The Pennsylvania State University

The Graduate School

Eberly College of Science

HIGH PRESSURE CHEMICAL DEPOSITION IN EXTREME ASPECT RATIO TEMPLATES FOR SEMICONDUCTOR OPTICAL FIBER APPLICATIONS

A Dissertation in

Chemistry

by

Justin R. Sparks

© 2013 Justin R. Sparks

Submitted in Partial Fulfillment
of the Requirements
for the Degree of

Doctor of Philosophy

May 2013

The dissertation of Justin R. Sparks was reviewed and approved* by the following:

John V. Badding
Professor of Chemistry
Dissertation Advisor
Chair of Committee

Ayusman Sen
Distinguished Professor of Chemistry

Harry R. Allcock
Evan Pugh Professor of Chemistry

Venkatraman Gopalan
Professor of Materials Science and Engineering
Associate Director of Center for Optical Technologies

Barbara J. Garrison
Shapiro Professor of Chemistry
Head of the Department of Chemistry

*Signatures are on file in the Graduate School

ABSTRACT

Amorphous silica microstructured optical fibers with micro/nanoscale arrays of pores designed in virtually any desired pattern are an exemplary platform for the manipulation of photons in cylindrical geometries, while, in contrast, crystalline semiconductors are ideal hosts for the control of electrons in planar geometries. The integration of semiconductors into the pores of microstructured optical fibers merges these two conflicting frameworks into one entity to result in a novel class of fiber geometry optoelectronic materials. The realization of such structures is a challenge in materials synthesis because conventional nanofabrication techniques cannot conformally coat such extreme aspect ratio pores with films of uniform thickness.

The focus of this dissertation was to develop an innovative, high pressure chemical deposition technique that removes the mass transport constraints in such intricate structures. The meter long, ultra-high aspect ratio pores of microstructured optical fibers are treated as high pressure chemical reactors for the deposition of Group IV and II-VI semiconductors from organometallic precursors. The behavior of molecules compressed to high pressures and confined to the small dimensions of the micro/nanoreactors is dramatically altered such that nearly every aspect of the pathway from molecular precursor to reaction product, including reactant flow, surface chemistry, chemical kinetics and thermodynamics, and nucleation and growth, differs from that under conventional conditions. Taking such factors into account, the necessary chemical principles have been developed to fabricate high quality Group IV and II-VI semiconductor core optical fibers by identifying and inventing high pressure chemical pathways that are suitable for the large aspect ratio, confined geometry capillary templates.

The high pressure reactions result in near atomically smooth micro/nanoscale diameter semiconductor wires and tubes that are much longer and more geometrically perfect than structures typically made by conventional nanofabrication methods. The extreme aspect ratios,

spatial organization, and geometric perfection of these fiber geometry materials make them of interest for a wide range of optical fiber applications. These multimaterial optical fibers exhibit very low loss and provide a platform with unprecedented capabilities for infrared laser light delivery and high power infrared lasers, amplifiers, and nonlinear optical devices that enable new function in the optical fiber geometry. Specifically, second order nonlinearity in optical fibers and the first Cr^{2+}:ZnSe optical fiber laser are demonstrated.

TABLE OF CONTENTS

LIST OF FIGURES

LIST OF TABLES

LIST OF ABBREVIATIONS

ALD	Atomic layer deposition
APCVD	Atmospheric pressure chemical vapor deposition
ARROW	Antiresonant reflecting optical waveguide
a-Si:H	Hydrogenated amorphous silicon
CVD	Chemical vapor deposition
CVT	Chemical vapor transport
CW	Continuous wave
DAP	Donor acceptor pair
DMS	Dilute magnetic semiconductor
EDFA	Erbium doped fiber amplifier
HPCVD	High pressure chemical vapor deposition
HR	High reflector
LMA	Large mode area
LO	Longitudinal optical
LPCVD	Low pressure chemical vapor deposition
LTD	Low temperature drawing
MCD	Molten core drawing
MOF	Microstructured optical fiber
NA	Numerical aperture
OC	Output coupler
OPG	Optical parametric generation
PAPF	Pressure assisted physical filling
PBG	Photonic bandgap
PCF	Photonic crystal fiber
PECVD	Plasma enhanced chemical vapor deposition
PIT	Powder in tube
poly-Si	Polycrystalline silicon
RMS	Root mean square
SEM	Scanning electron microscopy
SFG	Sum frequency generation
SHG	Second harmonic generation
TEM	Transmission electron microscopy
TO	Transverse optical
XRD	X-ray diffraction

ACKNOWLEDGEMENTS

The work presented in this dissertation would not have been possible without the support of my teachers, advisors, colleagues, friends, and family. First, I would like express my appreciation to my advisor, Dr. John Badding, for supporting me throughout my graduate career, giving me complete freedom to independently develop my project and design experiments, and ingraining his relentless approach to problem solving on me. Also, I am very grateful to Dr. Venkatraman Gopalan for his enthusiastic approach to my research and steadfast encouragement. I would also like to thank the members of my dissertation committee: Dr. Harry Allcock and Dr. Ayusman Sen.

My interdisciplinary research has led to some very enjoyable collaborations. At the University of Southampton, I thank my overseas advisors, Dr. Pier Sazio and Dr. Anna Peacock, who have been incredibly helpful throughout my graduate career, and my good friend, Dr. Noel Healy, who conducted many silicon and ZnSe optical fiber characterizations. At Penn State, I thank Dr. Mahesh Krishnamurthi for teaching me optical polishing techniques and light coupling, my good friend, Dr. Matthew Dirmyer, for his energizing attitude both in and out of the lab, Dr. Trevor Clark and Josh Maier of the Materials Characterization Laboratory for their assistance with various characterization techniques, Dr. Ali Borhan, and Dr. Eftihia Barnes. I am grateful to Dr. Patrick Berry and Dr. Ken Schepler at the Wright Patterson Air Force Base for their collaboration and financial support through the Air Force Research Lab, Sensors Directorate Contract FA8650-10-C-1902.

I would also like to thank the past and present members of the Badding group: Derek Keefer, Dr. Gregory Larsen, Dr. Jacob Calkins, Jesse Bischof, Dr. Michael Proia, Dr. Neil Baril,

Paramita Ray, Subhasis Chaudhuri, and Yunzhi Liu. I thank my officemates, Todd Day and Thomas Fitzgibbons, whose discussions/arguments made the office an entertaining and enjoyable environment. It was a pleasure to work with Dr. Rongrui He, whose purely objective, focused approach to experiments has significantly influenced who I am as a scientist today.

Finally, I am very grateful to my friends and family for their unwavering support and encouragement to pursue my passion for science. In particular, I thank my parents, Deborah and Ralph, for the sacrifices that they made for my education and the work ethic that they instilled in me, and my brother, Jared, for always being there to motivate me.

Chapter 1

An Introduction to the Optical Fiber Geometry: A Materials Limited Platform

1.1 The Fiber Geometry

From a materials science perspective, the optical fiber geometry is incredibly unique: micrometer to nanometer transverse dimensions with kilometer axial dimensions, making optical fibers the highest aspect ratio materials ever made.[1] Arranging materials in such geometries presents a fundamental challenge in materials fabrication, but also offers unique opportunities to exploit very weak effects in materials due to the extremely long interaction lengths of photons and electrons. Such high aspect ratio, 1-D structures are becoming advantageous, or even necessary, for next generation photovoltaic, electronic, spintronic, and photonic devices that require strict control over the structure, shape, and morphology of materials.[2,3] Waveguiding optical fibers are ubiquitous in transmitting light over long distances for the flexible delivery of optical power in technologies such as communication, surgery, and sensing due to their high purity, mechanical strength, and uniform, smooth structure.[4]

Optical fiber waveguides are well known for their significant technological applications in telecommunications, but are also important in many scientific fields by offering fundamental platforms for light manipulation, sensing, nonlinear optics, and imaging. Optical fibers originated as "single material" step index fibers made entirely of silica and guided light by total internal reflection via refractive index differences. It is said that whatever step-index fibers can do, they do it extremely well.[1] However, scientists and engineers want fibers that can do more: generate, modulate, and detect light, carry higher intensities, sense chemical species, have higher

nonlinearity properties, and in general, have more engineering parameters to tune. To have more tunability for photonic bandgap guidance, higher refractive index differences were needed, which led to the development of the air/silica microstructured optical fiber. To have more nonlinearity and optoelectronic function, the fiber fabrication process had to be reconsidered for non-glassy materials: either by adapting fiber drawing processes or by developing new fiber fabrication techniques to process functional materials such as semiconductors into the optical fiber geometry. This introduction will briefly highlight the materials science history of optical fibers and then focus on the materials challenges and progress that has been made in the fabrication of semiconductor optical fiber materials towards the realization of an entirely new platform of optical fiber technology.

1.1.1 Loss as a Function of Time

As early as the 19th century, the concept of guiding and confining light via total internal reflection was first discussed and applied to add color to water jets in decorative fountains. Later, these principles were applied to glass rods and fibers in the late 1920s for a variety of optical transmission applications such as medical endoscopy, periscopes, scramblers for defense, and even video transmission technology. For an excellent, thorough review of the history of fiber optics see reference [5]. Primarily, all the envisioned applications of such fibers called for short lengths; the idea that light could be transmitted over kilometers with low-loss optical fibers as the transmission media was considered preposterous.

In 1966, Charles Kao (Nobel Prize in Physics in 2009) proposed that the main sources of loss in a dielectric material were from absorption and scattering. He went on to predict that the intrinsic fundamental loss of optical fibers could be as low as a few dB/km. Even after this bold prediction, the concept of optical fibers as transmission media was not taken seriously. In the

1960s, state of the art glass fibers had a loss of 1 dB/m, or 1000 dB/km, which is an astronomically low transmission of 10^{-100}. To put this into perspective, a loss of 1000 dB implies that if one puts a number of photons into one end of the fiber equal to the total number of atoms in the known universe (~10^{80}), not a single one would make it through the fiber to the other end.[5] However, Kao's theoretical studies suggested that the loss in optical fibers could be reduced dramatically with proper glass processing, which put materials science and chemistry at the heart of the problem. For reference, the equation for loss in terms of dB is given below:

$$Loss(dB/L) = \frac{1}{L} 10 \log_{10} \frac{1}{T} \qquad \textbf{(Equation 1.1)}$$

where T is the transmittance over the length L.

A more detailed calculation of the fundamental loss limit in silica results in a value of 0.14 dB/km at wavelength of 1550 nm. This means that ~97% of the light can be transmitted through an optical fiber over one kilometer; which makes optical fibers a very practical media for transmitting high frequency light over long distances. Materials chemistry has been at the forefront of optimizing optical fiber drawing fabrication and reducing impurities in the glass that cause absorption and scattering and as a result decreasing the loss towards the fundamental limits. In fact, this loss value has been achieved experimentally, and silica fibers with this loss are now produced routinely. The decades of work to minimize the loss in silica are largely responsible for the revolution in communication that has significantly changed the world: the Internet.

1.1.2 Adding Structure

The fundamental transparency properties of silica had been fully exploited, but optical fiber materials research was certainly not finished. The second revolution in optical fibers started in the 1990s and centered on the structure of the silica fiber itself and the invention of fibers

referred to as microstructured optical fibers (MOFs) or photonic crystal fibers (PCFs).[6,7] These fibers are also made from silica, but have a microstructure of air holes in the transverse plane that continue in the axial direction down the fiber. MOFs are typically fabricated by the stack and draw method, shown in **Figure 1.1**, in which millimeter diameter silica tubes and solid rods are stacked into a centimeter scale preform of the desired pattern.[8,9] The preform is subsequently drawn in a tower furnace at high temperature (~2000 °C). The pattern that is created in the macroscale is drawn down to the microscale/nanoscale to physically reduce the dimensions while keeping the positions and relative sizes of the holes equivalent to the preform. This technique allows for virtually any pattern of holes of different shapes and sizes to be fabricated with precise locations in the transverse plane (**Figure 1.1**). Compared to other glasses, silica's low slope viscosity curve aids this process and allows for intricate structures to be drawn on nanometer scale dimensions.

In some geometries, MOFs can be thought of as 3-dimensional photonic crystals, where one dimension is considered to be infinite, and can have dispersion and nonlinear properties that are not possible with conventional silica fibers (although you can tailor these properties with tapering in conventional fibers). These fibers have found applications in a variety of scientific fields because they can have very unique optical properties such as photonic bandgap guidance, endlessly single mode operation, and supercontinuum generation. The supercontinuum fiber laser, for example, provides a white light source with the brightness of a laser, which is a valuable tool in a variety of laboratories. MOFs are also ideal containers for gasses and form very long gas waveguide cavities for sensing and gas laser applications.[10] MOFs have been a disruptive technology and have had and will continue to have an incredible impact in all areas of optical science.

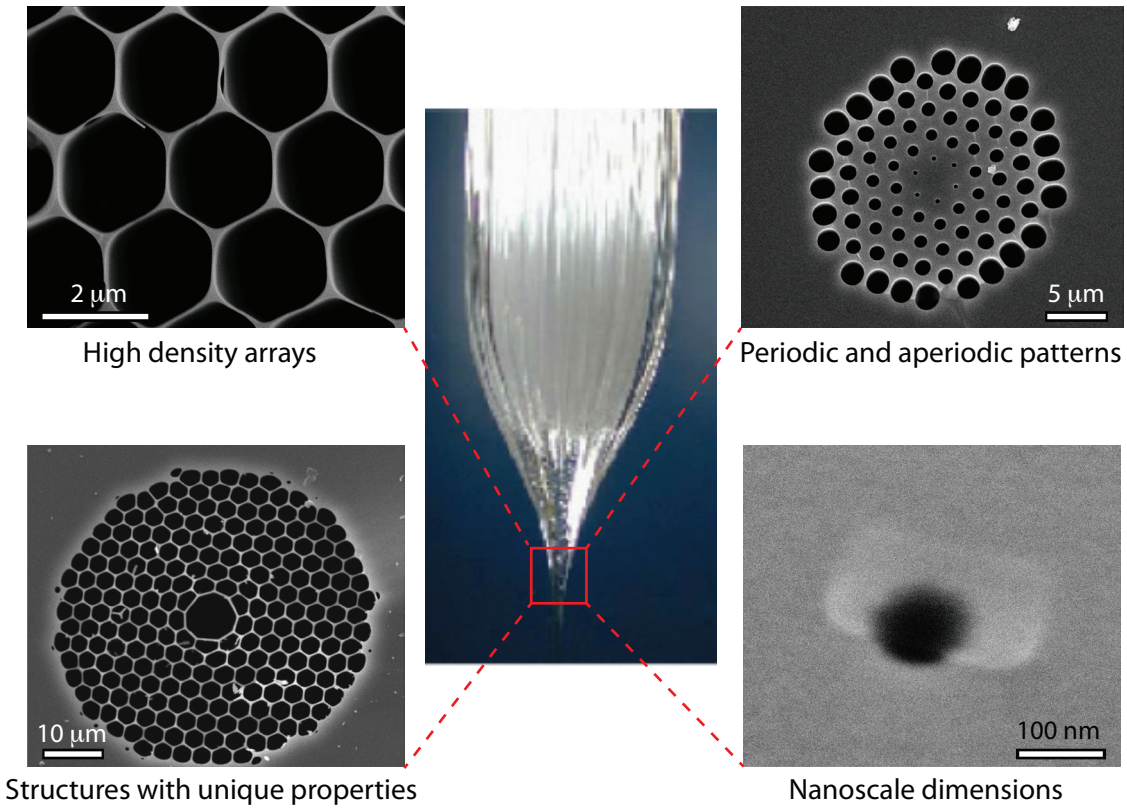

Figure 1.1: Microstructured optical fiber structures. The size, shape, and position of air holes in the transverse plane are controlled very accurately due to the precision of silica optical fiber drawing processes. Preform image (center) reproduced with permission from reference [8], © 2006 Wiley.

1.1.3 A Materials Limited Platform

Fiber drawing has unrivaled control over the position, shape, and size of glass cores in step index fibers or air holes in MOFs. However, the method places a stringent limit on the materials that can be incorporated within the silica MOF. Fabricating optical fibers out of crystalline or amorphous semiconductor materials poses a significant challenge in materials science due to thermal, chemical, and mechanical mismatches of the materials with the prevalent fiber material, silica. For example, many semiconductor materials are not compatible with standard drawing processes because of the necessity to have similar softening temperatures,

viscosities, and thermal expansion coefficients compared to silica. Thus, fabricating multimaterial optical fibers has posed as a significant challenge. For the "two material" air/silica MOFs, such challenges are not an issue because MOFs are still made from a single solid material, but multimaterial fiber fabrication methods need to address such issues. Also, the high temperatures necessary for fiber drawing can lead to undesired reactions and solid state diffusion that can destroy the pattern that was created in the preform. As such, the incorporation of unary and compound crystalline semiconductors within optical fibers is not possible with conventional drawing techniques. This materials limitation is highlighted in **Figure 1.2**, where drawing of a ZnSe optical fiber was attempted by the Ballato group in collaboration with Patrick A. Berry (Wright-Patterson Air Force Base) at Clemson University.[11] A cylinder of ZnSe was placed inside of a silica cladding tube to construct a preform which could then be drawn into an optical fiber. However, as the preform was heated up to the drawing temperature of silica (2000 °C), the ZnSe developed a significant vapor pressure in the preform via a dissociative sublimation. This vapor pressure caused the preform to explode before it could be drawn into a fiber. Thus, ZnSe, a material that will be discussed extensively in this dissertation, is considered "un-drawable".

1.1.4 Structural Perfection of Optical Fibers

Expanding the materials library of optical fibers not only has advantages for telecommunication and photonic technologies, but it also provides a platform for the hierarchical arrangement of materials in geometries not possible by planar fabrication methods. An ongoing challenge that is prevalent in nanoscience is the ability to control the organization of nanomaterials.[12] Many structures can be synthesized and fabricated, but a far greater challenge is to arrange them precisely with a scalable process necessary for real world applications. However, with the optical fiber fabrication processes and template approaches discussed in this dissertation,

wires, tubes, and heterostructures can be arranged in precise patterns for subwavelength imaging[13] and for the study of fundamental physical phenomena. The optical fiber geometry allows for materials to be processed into ultra-long nanowires[14] that allow for the study of physical properties without contact interference.[15] Nanowires that are meters to kilometers long that are in a larger template (the cladding) can literally be picked up and held in hand.

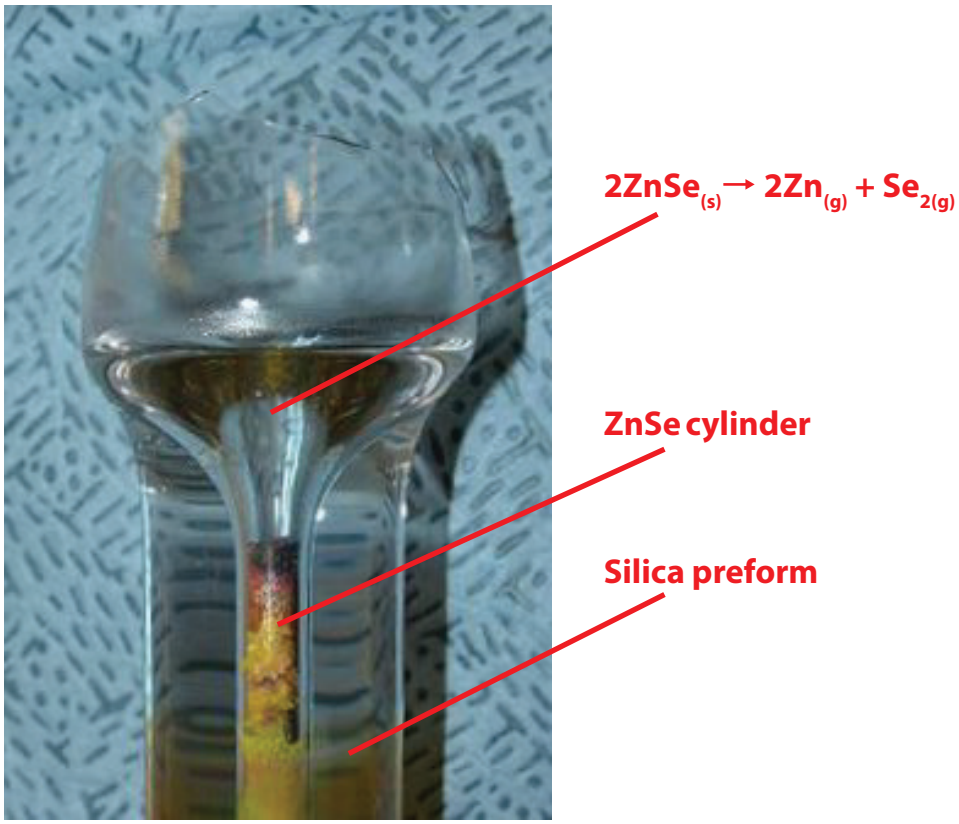

Figure 1.2: Failed ZnSe optical fiber drawing. When attempting to draw ZnSe with standard drawing processes, the preform explodes due to a buildup of pressure from the dissociative sublimation of ZnSe. Image reproduced with permission from Patrick A. Berry, WPAFB.[11]

Optical fiber fabrication processes can result in structures with unrivaled uniformity. For example, capillaries can have variations in diameter as small as tens of nanometers over centimeter length scales. For shorter length scales, surface capillary waves during fiber drawing determine the surface roughness and capillary uniformity. The silica surface is atomically smooth over short length scales, but some long range nanometer scale "roughness" arises from thermally

excited surface waves that form in the low viscosity, glassy state that get frozen in as the glass cools.[16-18] These are dictated by the equilibrium thermodynamics and cannot be removed with process improvement. However, the low hydroxyl content of optical fibers allows the amplitude of the waves to be dampened due to increased surface tension. Thus, the optical fiber geometry fabrication processes presented in this dissertation have the potential to fabricate the most structurally perfect wires of materials over unprecedented length scales.

1.2 Semiconductor Optical Materials

Table 1.1: A summary of the optical properties of semiconductors that have been fabricated into optical fibers to date compared to silica. Data sources: *:[19] #:[20] %:[21]

Material	n (@1.550 μm)	Melting Point (°C)	Linear Thermal Expansion (10^{-6} K^{-1}, 300°C)	Transparency Window (μm)
Silica	1.44#	1983%	0.51%	0.16 – 3.8%
Si	3.47#	1414*	2.5*	1.1 – 6.5%
Ge	4.28#	938*	6.1*	1.8 – 15%
Diamond	2.38#	3577*	1.2*	0.24 – 2.7%
ZnS	2.27#	1700*	6.4*	0.4 – 12.5%
ZnSe	2.45#	1525 (sublimes)*	7.2*	0.5 – 19%
ZnO	1.92,1.94%	1974*	2.9*	0.4 – 10#
CdS	2.29#	1750*	4.7*	0.5 – 15%
PbS	4.25#	1113*	15*	3 – 20#
InSb	4.08#	525*	4.7*	7 – 30#
InP	3.17#	1057*	4.6*	1 – 15#
As_2S_3	2.44#	310*	26.1%	0.62 – 11%
As_2Se_3	2.88 (@1.2μm)#	260*	24.6%	0.87 – 17.2%
TeO_2	2.27%	733*	15.0%	0.34 – 4.5%

Amorphous silica fibers and MOFs have been shown to be ideal hosts for the manipulation of photons in cylindrical geometries. Conversely, crystalline semiconductors are ideal hosts for the manipulation of electrons in (typically) planar geometries. Combining semiconductors and optical fibers into one entity opens up a new class of "fiber geometry" optoelectronic materials. Compared to silica, semiconductors can add an assortment of new

function to the optical fiber geometry. This section describes some of the basic properties and advantages of semiconductors, with a focus on laser and optical isolator applications in the mid-IR. **Table 1.1** provides a summary of the important optical/material properties of some materials that have been fabricated into the fiber geometry to date by a variety of methods.

1.2.1 Transparency Windows

The applications of silica-based fibers are typically limited to passive optical waveguides that function at wavelengths shorter than ~3 μm due to the transmission limits of silica. Transmitting infrared light with fiber optics is very desirable for chemical and thermal sensing but requires materials that have high transmission in the mid to far IR.[22,23] For example, the molecular fingerprint region is from 6 – 20 μm and is very important for monitoring chemical reactions or detecting chemical threats from a distance, while arrays of fibers can provide a means to remote thermal imaging. Another application is the delivery of high laser powers (for example, 10.6 μm CO_2 laser light) for various industrial laser cutting/welding processes and medical laser surgery technologies. Many semiconductors have transmission windows that extend much farther into the IR than silica (**Table 1.1**), making them very useful for such applications. Materials with lower phonon freqencies (e.g., ZnSe) have a longer cut-off edge of transparency and can push the transmission window of the fiber farther into the IR, well beyond 20 μm.

1.2.2 Intrinsic Loss Limits of Semiconductors

The loss limit of a material in a window in which it is considered transparent can be calculated by considering three intrinsic loss mechanisms. The short wavelength side is influenced by electronic absorption, while the long wavelength side is influenced by multiphonon

absorption. In between, Rayleigh/Brillouin scattering determine the fundamental loss. Optical loss versus wavelength plots, known as V-curves, (**Figure 1.3**) are a standard way to determine the loss of a material in the window in which it is transparent. The plots result in a curve with a minimum loss value at a certain wavelength that is at the intersection of the scattering curve and the multiphonon absorption curve. For silica, this is the value mentioned in **Section 1.1.1** of 0.14 dB/km at 1.55 μm wavelength, which is why all telecommunication optoelectronics are in this wavelength range.

The equations that are needed to construct a V-curve as a function of frequency (ω) or wavelength (λ) for a given semiconductor are:

1. Urbach electronic absorption tail (direct bandgap materials):[24]

$$\alpha(cm^{-1}) = Ae^{\sigma(\hbar\omega - \hbar\omega_{gap})/k_B T} \quad \textbf{(Equation 1.2)}$$

(where A and σ are constants specific to the material, k_B is Boltzmann's constant, and T is temperature)

2. Pinnow Rayleigh/Brillouin scattering:[25]

$$\alpha(m^{-1}) = \frac{8\pi^3}{3}\frac{1}{\lambda^4}(n^8 P_{12}^2)(k_B T \mathrm{B}_T) \quad \textbf{(Equation 1.3)}$$

(where P_{12} is the elasto-optic coefficient, B_T is the isothermal compressibility, and n is the refractive index at wavelength λ)

3. Multiphonon absorption:[26]

$$\alpha(cm^{-1}) = Ae^{-B\omega/\omega_{phonon}} \quad \textbf{(Equation 1.4)}$$

(where A and B are constants specific to the material)

With these equations, the fundamental loss limits of a material can readily be calculated.[22] As shown in **Figure 1.3**, the intrinsic loss of a semiconductor, like ZnSe, can be orders of magnitude lower than silica. For ZnSe, the lowest loss wavelength is ~6 μm with a loss

of 10^{-5} dB/km. Another example is aluminum oxide, with a loss of 10^{-3} dB/km at 1.78 μm.[22] For many IR transparent solids with a low phonon frequency (e.g., 250 cm^{-1} for ZnSe), the intersection of the scattering line with the multiphonon absorption line is pushed farther into the IR, where scattering can be significantly less because of the λ^{-4} and n^8 dependence.

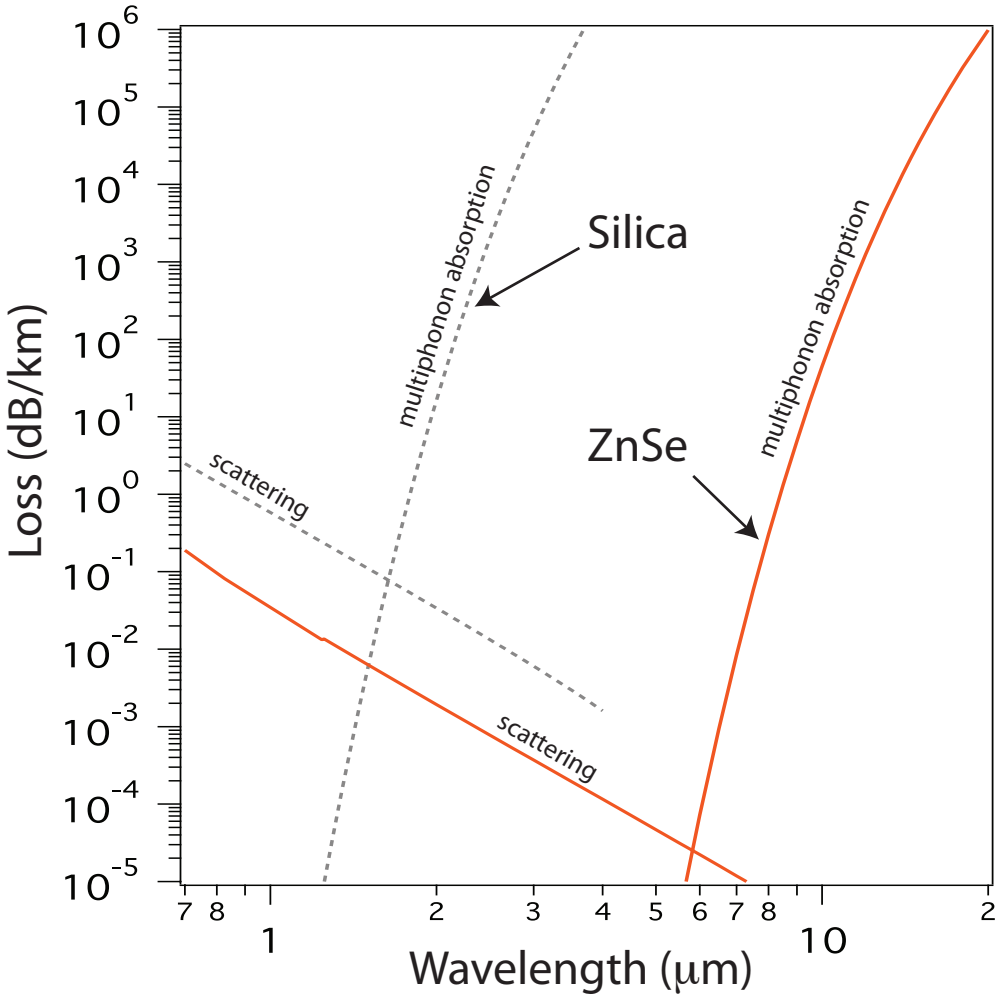

Figure 1.3: V-curves of silica and ZnSe. The fundamental limit of losses in semiconductors can be orders of magnitude lower than silica.

A semiconductor optical fiber with loss on the order of 10^{-4} dB/km would have a core that is a perfectly pure single crystal with zero Rayleigh scattering due to grain boundaries and defects. Brillouin scattering from density fluctuations due to temperature and phonons are unavoidable and set the lower limits for loss, while multi-phonon absorption sets the intersection

of the V-curve. Also, the optical fiber would have to be geometrically perfect with atomically smooth surfaces and the lack of any scattering sites such as micro-cracks or other extrinsic loss mechanisms.

If these ultra-low loss fibers could be fabricated, they would eliminate the need for repeaters/amplifiers in the telecommunications network as well as open up many new possibilities. To put these losses into perspective, a semiconductor optical fiber with a loss of 10^{-4} dB/km could wrap around the circumference of the earth (~40,000 km) and have an attenuation of only 4 dB, or 39% transmission. For comparison, a silica fiber would have a loss of 5600 dB. Although it seems unlikely that such limits will ever be reached for ZnSe, sapphire, etc., it is worth noting that it took decades of research to reach the fundamental loss limit of silica fibers, where there were initial doubts as well. However, many of the structures and devices that will be presented in this dissertation do not require such long lengths and ultra-low loss.

1.2.3 Photonic and Optoelectronic Properties of Semiconductors

By fabricating optically and electrically active semiconductors into the long, cylindrical fiber geometry, unique waveguides can be realized for nonlinear optics and laser applications. As an example, the optical fiber geometry is very resilient against detrimental thermal effects that typically limit the output power of lasers; as such, some of the world's most powerful commercially available lasers are fiber lasers.[27] Doping silica (for example, with Er^{3+} and Yb^{3+}) has successfully led to numerous breakthroughs in photonics from the erbium doped fiber amplifier (EDFA) to multi-kilowatt class ytterbium doped fiber lasers; nevertheless, the varying chemical environment in a glass limits dopants to shielded f-shell rare earth ions and typically excludes d-shell transitions of metal ions that require a crystalline host. Embedding non-silica solid state laser materials into the fiber geometry will be of great value in the power scaling of

many solid state lasers across the entire spectrum. The optical fiber geometry is the ideal geometry for high power lasers, so it is desirable to have access to a variety of laser transitions based on Cr^{2+} or Fe^{2+} doped II-VI semiconductors. For example, Cr^{2+}:ZnSe based lasers are plagued by thermal effects which could be eliminated by fabricating the material into the optical fiber geometry (this is discussed in more detail in **Chapter 6**), which is the central goal of this dissertation. ZnSe also has second order susceptibility (which silica does not) and enables function such as second harmonic generation in the optical fiber geometry (**Chapter 5**). It is noted that the EDFA was responsible for the incredible improvements in long haul communication as it allowed for a network with much more efficient amplifiers while keeping the light within the fiber. The development of detectors, modulators, nonlinear devices, and other amplifiers is expected to have similar impacts on communications as well as many other optoelectronic fields.

Incorporating optoelectronic materials into optical fibers allows for active devices to be fabricated within optical fibers. Semiconductor junctions with precise electronic dopants are necessary for such devices such as high speed detectors and modulators. Traditionally, these types of structures have been limited to millimeter to centimeter length scales on planar, rigid substrates. Fabricating devices directly into the optical fiber can have a variety of advantages such as uninterrupted, high speed processing of telecommunication signals without the need to couple the light to a wafer.[28] Such discrete, bulky optical-electrical-optical conversions are a bottleneck to the speed of the network and increase the power consumption of the Internet. Furthermore, there has been a motivation in materials science to move to longer length scales and to more flexible forms[29] for applications such as power generation, chemical sensing, and foldable displays. The optical fiber geometry is ideal for such applications as they can be indefinitely long and can be woven into fabrics and three-dimensional structures.

1.2.4 Magneto-Optical Properties of Semiconductors

Semiconductors doped with magnetic transition metals, such as $Zn_{(1-x)}Mn_xSe$, are termed as dilute magnetic semiconductors (DMS) because of their magnetic and semiconducting properties. Other chalcogenide materials also exhibit magneto optical properties.[30] These materials have applications in spintronics and magneto-optics.[31] For example, DMSs can be used as optical isolators, which are non-reciprocal devices that transmit light in only one direction. As the optical analog of an electrical diode, the main purpose of an optical isolator is to prevent reflected light from returning to the source, which can have detrimental effects on devices such as lasers, circulators, modulators, and splitters.[32,33] The underlying physical principal is the rotation of the linear polarization of the light within the structure.

The degree of rotation of the polarization of light that passes through a Faraday rotator, which rotates the polarization of light in the presence of a magnetic field, is given by:

$$\theta = VLB \qquad \textbf{(Equation 1.5)}$$

where θ is the angle of rotation, L is the length of the device, B is the magnetic field, and V is the Verdet constant ($°cm^{-1}T^{-1}$), which is a measure of the strength of the Faraday effect of the material. Therefore, with a higher Verdet constant, a much shorter pathlength is needed for a given rotation angle of the polarization (45° for an isolator). For comparison, the Verdet constant of silica glass is 2 $°cm^{-1}T^{-1}$,[34] while that of $Zn_{(1-x)}Mn_xSe$ is 300 $°cm^{-1}T^{-1}$ (at 650 nm).[35] Therefore, the incorporation of such a device in current silica fiber technology is not practical because of the long length needed (2.25 m for a 0.1 T field). However, fabricating $Zn_{(1-x)}Mn_xSe$ optical fibers would allow for fiber based high power optical isolators (**Figure 1.4**) that operate into the mid-IR because much shorter lengths are needed (1.5 cm for a 0.1 T field). This simplifies systems in which optical isolation is required because the device is within the optical fiber, eliminating the need for alignment in current free space devices and making the system

much more rugged, compact, and capable of handling much higher optical intensities. Systems like these would be essential for high power Cr^{2+}:ZnSe optical fiber lasers.

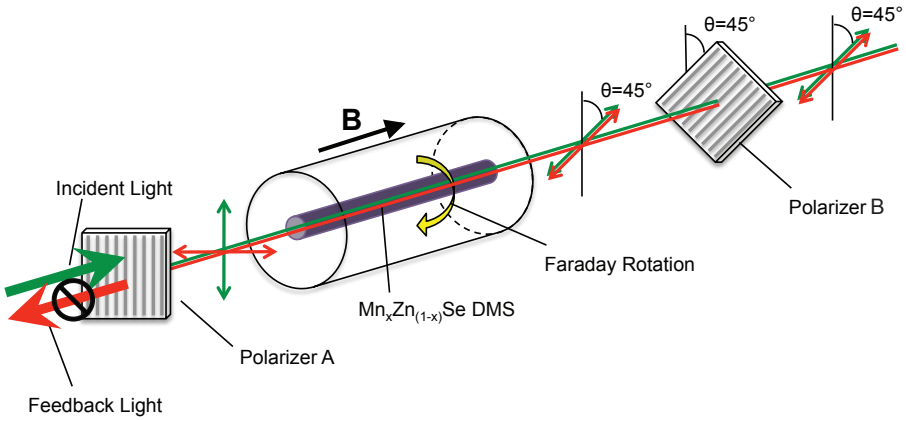

Figure 1.4: Schematic of a mid-IR optical fiber isolator. The active waveguide rotates the polarization of the incident light (green) 45° so that it can pass through polarizer B. Reflected or feedback light (red) that propagates in the reverse direction is rotated another 45° in the same direction, which then cannot pass through polarizer A. The polarizers are shown in free space for clarity; they could be deposited on the end facets of the fiber for a completely fiberized isolator.

1.3 Current Semiconductor Optical Fiber Fabrication Methods

Many approaches have been taken to fabricate optical fibers with semiconductor cores, each with its own advantages and disadvantages for certain materials and applications. The techniques can be divided into two principal categories: adapting current drawing techniques to be suitable for different materials, or utilizing post-drawn capillaries or MOFs as templates for the infiltration of materials. The Ballato group at Clemson and the Pickrell group at Virginia Tech have developed molten core and powder in tube variations of fiber drawing to realize semiconductor core fibers, while the Fink group at the Massachusetts Institute of Technology has transitioned to low melting, glassy semiconductors that can readily be drawn. Another drawing approach is to use nanoparticle/glass composites to add the desired properties to the core, which has been developed by a variety of groups. In terms of the template category, the Russell group

at the Max Planck Institute in Erlangen has developed physical melt-infiltration techniques, while the collaboration between Pennsylvania State University and the University of Southampton has developed a high pressure chemical deposition approach to deposit semiconductors inside the pores of post-drawn capillaries and MOFs. The high pressure template approach is the focus of this dissertation; however, it is worth briefly reviewing the advantages and disadvantages of the other techniques.

1.3.1 Molten Core Drawing

The Ballato group at Clemson University has developed a molten core crucible technique to draw optical fibers primarily with Group IV semiconductors,[36-38] and more recently extending the method to III-V semiconductors,[39] in a process called molten core drawing (MCD).[40] First, a rod of the semiconductor material is placed inside a cladding glass tube to construct a preform. When the preform is heated to the glass transition temperature of the cladding and above the melting point of the core material, the fiber is then drawn. Although the semiconductor is a molten liquid at the draw temperature, the glass is still rigid enough with a sufficiently low viscosity to be drawn while functioning as a container to contain and shape the semiconductor into the fiber geometry.

To date, MCD has been applied to make circular and square cross-section step index fibers,[41] and the group anticipates that the process could be adapted to microstructured fibers. This method is very useful for fabricating long lengths of optical fiber for applications such as laser light delivery because it uses standard equipment that is used in modern optical fiber drawing facilities. However, the high temperature process limits the materials selection to crystalline ones and can result in significant diffusion of impurities from the cladding, such as oxygen from silica, into the core of the fiber. This may ultimately place a lower limit on the core

size, as small cores of silicon could become completely oxidized to silica during the drawing.[40] However, by introducing sacrificial oxygen getter materials such as SiC into the core during the drawing of silicon, oxygen contamination can be reduced.[42] This reactive MCD method may also be adapted to synthesize materials from two or more reactants during the processing to expand the library of available materials. Thus, instead of being inhibited by the high temperatures needed, the process can take advantage of solid state reactions that can be favored under the draw conditions.

Thermal expansion mismatch is a common problem in many of the techniques presented in this introduction. Drawing at such high temperatures exacerbates expansion mismatch effects and can result in cracking because of the extraordinarily low thermal expansion coefficient of silica compared to many semiconductors (**Table 1.1**). To this end, the Clemson group is investigating more appropriate glass compositions for use as cladding materials that will be more compatible with the molten semiconductors in terms of thermal expansion and temperature-viscosity properties.[36] Germanium melts at a much lower temperature than the glass transition of silica, so a lower melting point glass can substantially reduce the drawing temperature from that of silica (1600 – 2000 °C) to a more modest temperature around 1000 °C. Since diffusion of impurities from the cladding is a thermally driven process, drawing germanium fibers in lower temperature glasses will allow for much improved optical fibers.

The first demonstration of a III-V compound semiconductor optical fiber was InSb by MCD.[39] A phosphate glass cladding was used because it is more thermally compatible with the low melting point semiconductor (527 °C). Oxygen and phosphorous contamination of the core by diffusion from the cladding at the draw temperature was observed, but the material was phase pure. Optical transmission measurements could not be made due to the free carrier absorption of the doped core. The fiber was drawn for a proof of concept that MCD was applicable to compound semiconductors and the group anticipates that the method can be extended to other

families of compound semiconductors. As was shown in **Figure 1.2**, the material must not develop a vapor pressure at the drawing temperature, making ZnSe optical fibers inaccessible by this technique.

1.3.2 Powder in Tube

At Virginia Tech, the Pickrell group has taken a similar approach to MCD by using a powder-in-tube (PIT) method to produce smaller core size silicon optical fibers of shorter lengths.[43] In this method, silicon powder is densely packed into millimeter diameter silica tubes, which can then be heated and stretched on a bench top scale fiber drawing apparatus to produce fibers with circular core sizes with diameters that range between 10 – 100 μm. These fibers are typically fabricated over centimeter length scales for testing purposes, but the process should be adaptable to large fiber drawing towers as well. The PIT method was the first to fabricate n-doped (phosphorus) silicon core optical fibers by using doped silicon powder as the starting material.[44] Similar to the MCD method, the high temperatures needed for the drawing cause micro-cracks to form in the core, which can also develop some shape non-uniformity.

1.3.3 Low Temperature Drawing

Instead of limiting the materials that can be drawn to those that are thermally compatible with silica cladding, an alternative approach is to use standard drawing techniques with an entirely new platform of materials.[45] To take the place of a silica cladding, a polymer can be used such as polyethersulfone as the glassy container for low temperature drawing (LTD) of materials.[46] Many materials such as chalcogenides and low melting point metals can be compatible with each other for drawing purposes. These materials, which are primarily

amorphous but can be crystalline,[47] serve well for some fiber devices but will be limited in their use for high power density applications like fiber lasers. The Fink group at MIT has pioneered this approach to result in a variety of very unique, long fiber structures[14] and devices with unique optical,[48] electrical,[49] thermal,[50] and acoustic functionality.[51] These fibers are very useful for delivering optical power at wavelengths where silica is opaque, with the Omniguide fiber as an excellent example of commercially successful non-silica optical fiber.[52]

In terms of the general challenge in materials science of producing and orienting nanostructures, LTD excels at producing unique spheres[53] and ultra-long nanowires[14] out of various materials as well as complex shaped particles.[53] This highlights that optical fiber fabrication not only has applications in fiber optics but is also transforming into a general nanomaterials synthesis technique with many advantages over traditional methods. For example, an ultra-long nanowire embedded within a cladding of micrometer dimensions is readily manipulated and positioned by hand. No other technique, except for the ones presented in this introduction, can produce a nanowire this long that can simply be handled in this way. Also, bottom up synthesis approaches result in particles of varying dimensions, while many top down approaches are not nearly as scalable as fiber drawing, where in principle 10^8 nanowires of meter length scales could be fabricated and aligned in a single fiber draw.[14] Furthermore, the precise control of shape, size, and arrangement of materials that fiber drawing offers is now being extended to the field of nanoparticles, with very precisely designed Janus and “beach ball” particles.

Although moving to lower temperature cladding materials (such as amorphous chalcogenides) allows for the incorporation of new materials into optical fibers, this technique does not allow for traditional, technologically relevant semiconductors (such as group II, II-VI, and III-V) to be drawn. As a result, the materials typically have a lower device performance compared to that of traditional semiconductors because the LTD materials have significantly

lower electron/hole mobilities. High speed electrical and optoelectronic devices cannot be fabricated from amorphous materials, as crystalline materials, in general, have higher carrier mobilities that enable better device performance. Another major drawback of chalcogenide glasses is that they have very limited power handling capabilities because of their low electronic bandgaps, low melting points, and susceptibility to photostructural effects which limits their use for high power fiber laser applications.[54] However, fibers fabricated by LTD can be crystallized via post drawing annealing processing.[47]

During the drawing, chemical synthesis can occur at interfaces when appropriately chosen materials are in physical contact with each other.[55] This is valuable for fabricating electrical junctions from more relevant semiconductors, such as ZnSe, which is formed at the interface between $Sn_{85}Zn_{15}$ and $Se_{97}S_3$. However, it is unlikely that such interfacial reactions, which take place in domains on the order of 100 nm, will be able to produce core sizes large enough for optical applications. If appropriate starting materials are chosen, then many other semiconductors could be incorporated into the optical fiber geometry using this drawing synthesis technique for a variety of electrical and optical functionality.

1.3.4 Particle Composites

Another way to synthesize materials that are not compatible with drawing into the optical fiber geometry is to disperse particles of the material into a glass that can readily be drawn. For example, diamond, one of the hardest materials to melt or draw, can be fabricated into optical fiber form by dispersing 40 – 50 nm particles of diamond into a tellurite glass, which can then be drawn into optical fibers to take advantage of the optical properties of diamond in the fiber geometry such as the nitrogen-vacancy color center.[56] This process has also been shown with silicon[57] and InP.[58] Another example is Cr^{2+}:ZnSe, which as discussed earlier is highly desirable

to fabricate into optical fibers for high power laser applications, but is very difficult to draw because of the high vapor pressure. However, fibers can be drawn with 30 nm Cr^{2+}:ZnSe crystals dispersed in a As_2S_3 glass, enabling mid-IR emission.[59]

This technique can allow for a variety of materials that are typically not compatible with drawing processes to be fabricated into the fiber geometry. However, the use of chalcogenide hosts for diamond or Cr^{2+}:ZnSe does not allow all of the excellent properties of the material to be fully exploited which makes a core that is made entirely out of the material much more desirable. For example, diamond has a very high damage threshold and thermal conductivity;[60] however, chalcogenide glasses typically have very low damage thresholds and thermal conductivities in comparison. Also, care must be taken to avoid any reactions that would result in diffusion of the cladding into the particle and thus dissolve it.

1.3.5 Pressure Assisted Physical Filling

Using post drawn capillaries and MOFs as templates for the physical infiltration of materials by pressure assisted physical filling (PAPF) allows for a variety of materials to be introduced into the fiber geometry that are completely incompatible with drawing. The Russell group at Erlangen used PAPF to fabricate structures of glasses that are typically considered to be incompatible at drawing temperatures, such as silica and chalcogenides.[61] This method can fill capillaries as small as 200 nm,[62,63] and has been used to fabricate both step index and MOF chalcogenide/silica hybrid fibers.[64,65] Chalcogenide glasses can have extraordinarily high nonlinear susceptibilities and can have transmission windows far into the IR depending on their composition. $Ga_4Ge_{21}Sb_{10}S_{65}$ glass has been infiltrated into a 1.6 μm diameter capillary to make a step index fiber for efficient supercontinuum generation, while a tellurite melt (75 mol.% TeO_2, 10 mol.% ZnO, 15 mol.% Na_2O) was infiltrated into a MOF to fabricate an all-solid bandgap

fiber.[63] The technique has been used to fabricate optical fibers with magneto-optical glasses for Faraday rotation applications as well.[30] Selective filling of pores in MOFs is possible,[66] to provide more freedom in optical fiber design. The group anticipates moving towards other materials such as As_2S_3 for a variety of amplification, modulation, filtering, and nonlinear applications.

Many materials such as liquids,[67] gases,[68] metals,[69] and colloids[70] have been infiltrated into MOFs by PAPF, but, to date, semiconductors have been limited to germanium.[71] The PAPF method requires that the material be a fluid or have a congruent melting point that is below that of the glass transition temperature of silica. ZnSe does not melt congruently, which makes it incompatible with this technique.

1.3.6 Deposition from Solution

By employing chemical bath deposition chemistries, the Harrington group at Rutgers and the Miyagi at Tohoku University, Japan have led the development of a wet chemistry processing method to deposit semiconductor and metallic layers within 1000 μm diameter silica capillaries. Films of various semiconductors such as ZnS, ZnSe, Ge, CdS, and PbS as well as metals can be deposited by precipitating out the materials from a solution of their salts with pH control.[22,72] This process has been primarily used to fabricate very large, hollow core optical fibers for infrared power delivery and sensing applications. The inner surfaces of the films have a surface roughness on the order of 10 nm. Complete filling of pores with this technique has not been reported, but the hollow core fibers have losses on the order of 1 dB/m. This technique will likely not be as viable for nanometer to micrometer sized capillaries in view of liquid mass transport and surface tension constraints.

1.4 Optical Fiber Fabrication from a Chemist's Perspective

Of all the materials and methods discussed in this introduction, the II-VI semiconductors, such as ZnSe, seem to be the most challenging materials to form into the optical fiber geometry due to their high vapor pressures and incongruent melting points. When a chemist looks at the MOF structures shown in **Figure 1.1**, an opportunity for the templated growth of materials becomes apparent. By chemically depositing II-VI semiconductors within the pores of MOFs, the first II-VI semiconductor optical fibers could be realized. The challenge that arises is the difficulty of infiltrating molecules into such high aspect ratio pores. The answer, and the focus of this dissertation, is pressure. Through the use of high pressures to overcome the mass transport constraints, gaseous chemical precursors can be introduced into the high aspect ratio pores. The meters-long, ultra-high aspect ratio pores of MOFs can then be treated as high pressure chemical reactors for the deposition of semiconductors, metals, and insulators from hydride and organometallic precursors[73] in a process termed high pressure chemical vapor deposition (HPCVD). The behavior of molecules compressed to high pressures and confined to the small dimensions of the micro/nanoreactors is dramatically altered such that nearly every aspect of the pathway from molecular precursor to reaction product, including reactant flow, surface chemistry, chemical kinetics/thermodynamics, and nucleation/growth, differs from that under conventional conditions. The focus of this dissertation will be to investigate these effects with the goal of fabricating the first II-VI semiconductor optical fibers for nonlinear optics and to demonstrate the first Cr^{2+}:ZnSe optical fiber laser.

1.5 References

[1] P. St. J. Russell, "Photonic Crystal Fibers: A Historical Account" *IEEE Lasers and Electro-Optics Soc.* **2007**, 21, 11.

[2] Y. Xia, P. Yang, Y. Sun, Y. Wu, and B. Mayers, "One-Dimensional Nanostructures: Synthesis, Characterization, and Applications" *Adv. Mater.* **2003**, 15, 353.

[3] B. Tian, X. Zheng, T. J. Kempa, Y. Fang, N. Yu, G. Yu, J. Huang, and C. M. Lieber, "Coaxial Silicon Nanowires as Solar Cells and Nanoelectronic Power Sources" *Nature* **2007**, 449, 885.

[4] W. A. Gambling, "The Rise and Rise of Optical Fibers" *IEEE J. Sel. Top. Quantum Electron.* **2000**, 6, 1084.

[5] J. Hecht, "*City of Light: The Story of Fiber Optics*" Oxford University Press, NY, **2004**.

[6] J. C. Knight, J. Broeng, T. A. Birks, and P. St. J. Russell, "Photonic Band Gap Guidance in Optical Fibers" *Science*, **1998**, 282, 1476.

[7] P. St. J. Russell, "Photonic Crystal Fibers" *Science* **2003**, 299, 358.

[8] J. Laegsgaard and A. Bjarklev, "Microstructured Optical Fibers: Fundamentals and Applications" *J. Amer. Ceram. Soc.* **2006**, 89, 2.

[9] T. M. Monro and H. Ebendorff-Heidepriem, "Progress in Microstructured Optical Fibers" *Annu. Rev. of Mater. Res.* **2006**, 36, 467.

[10] A. V. V. Nampoothiri, A. M. Jones, C. Fourcade-Dutin, C. Mao, N. Dadashzadeh, B. Baumgart, Y. Y. Wang, M. Alharbi, T. Bradley, N. Campbell, F. Benabid, B. R. Washburn, K. L. Corwin, and W. Rudolph, "Hollow-Core Optical Fiber Gas Lasers (HOFGLAS): A Review" *Opt. Mater. Express* **2012**, 2, 948.

[11] P. A. Berry, "Versatile Chromium-Doped Zinc Selenide Infrared Laser Sources" *Dissertation*, Air Force Institute of Technology, Dayton, Ohio, **2010**.

[12] C. M. Lieber, "The Incredible Shrinking Circuit" *Sci. Amer*. **2007**, 17, 64.

[13] M. Krishnamurthi, E. Barnes, J. R. Sparks, R. He, N. F. Baril, P. J. A. Sazio, J. V. Badding, and V. Gopalan, "A Magnifying Fiber Element with an Array of Sub-Wavelength Ge/ZnSe Pixel Waveguides for Infrared Imaging" *Appl. Phys. Lett.* **2012**, 101, 021108.

[14] M. Yaman, T. Khudiyev, E. Ozgur, M. Kanik, O. Aktas, E. O. Ozgur, H. Deniz, E. Korkut, and M. Bayindir, "Arrays of Indefinitely Long Uniform Nanowires and Nanotubes" *Nat. Mater*. **2011**, 10, 494.

[15] M. Singh, J. Wang, M. Tian, T. E. Mallouk, and M. H. W. Chan, "Antiproximity Effect in Aluminum Nanowires with No Applied Magnetic Field" *Phys. Rev. B.* **2011**, 220506R.

[16] P. J. Roberts, F. Couny, H. Sabert, B. J. Mangan, T. A. Birks, J. C. Knight, and P. St. J. Russell, "Loss in Solid-Core Photonic Crystal Fibers Due to Interface Roughness Scattering" *Opt. Express* **2005**, 13, 7779.

[17] P. J. Roberts, F. Couny, H. Sabert, B. J. Mangan, D. P. Williams, L. Farr, M. W. Mason, A. Tomlinson, T. A. Birks, J. C. Knight, and P. St. J. Russell, "Ultimate Low Loss of Hollow-Core Photonic Crystal Fibres" *Opt. Express* **2005**, 13, 236.

[18] J. Jackle and K. Kawasaki, "Intrinsic Roughness of Glass Surfaces" *J. Phys.: Condens. Matter* **1999**, 7, 4351.

[19] D. R. Lide, "*CRC Handbook of Chemistry and Physic*s" 84th Ed. CRC Press, FL, **2004**.

[20] E. D. Palik, "*Handbook of Optical Constants of Solids*" Elsevier, **1998**.

[21] M. Bass, "*Handbook Of Optics Volume III*" McGraw-Hill, **2001**.

[22] J. A. Harrington, "*Infrared Fibers and Their Applications*" SPIE, **2004**.

[23] A. Méndez and T. F. Morse, "*Specialty Optical Fibers Handbook*" Elsevier, **2006**.

[24] J. Baillou, J. Daunau, P. Bugnet, J. Daunay, C. Auzary, and R. Poindessault, "Optical-Absorption Edge in Doped and Undoped Znse Crystals" *J. Phys. Chem. Solids* **1980**, 41, 295.

[25] D. A. Pinnow, T. C. Rich, F. W. Ostermayer, and M. DiDomenico, "Fundamental Optical Attenuation Limits in the Liquid and Glassy State with Application to Fiber Optical Waveguide Materials" *Appl. Phys. Lett.* **1973**. 22, 527.

[26] B. Bendow, "Fundamental Optical Phenomena in Infrared Window Materials" *Annu. Rev. Mater. Sci.* **1977**, 7, 23.

[27] D. J. Richardson, J. Nilsson, and W. A. Clarkson, "High Power Fiber Lasers: Current Status and Future Perspectives" *J. Opt. Soc. Am. B* **2010**, 27, B63.

[28] R. He, P. J. A. Sazio, A. C. Peacock, N. Healy, J. R. Sparks, M. Krishnamurthi, V. Gopalan, and J. V. Badding, "Integration of Gigahertz-Bandwidth Semiconductor Devices Inside Microstructured Optical Fibres" *Nature Photon*. **2012**, 6, 174.

[29] S. Ju, A. Facchetti, Y. Xuan, J. Liu, F. Ishikawa, P. Ye, C. Zhou, T. J. Marks, D. B. Janes, "Fabrication of Fully Transparent Nanowire Transistors for Transparent and Flexible Electronics" *Nature Nano*. **2007**, 2, 378.

[30] M. A. Schmidt, L. Wondraczek, H. W. Lee, N. Granzow, N. Da, and P. St. J. Russell, "Complex Faraday Rotation in Microstructured Magneto-Optical Fiber Waveguides" *Adv. Mater.* **2011**, 23, 2681.

[31] T. Dietl, "Dilute Magnetic Semiconductors: Functional Ferromagnets" *Nat. Mater.* **2003**, 2, 646..

[32] H. Dtsch, N. Bahlmann, O. Zhuromskyy, M. Hammer, L. Wilkens, R. Gerhardt, P. Hertel, and A. F. Popkov, "Applications of Magneto-Optical Waveguides in Integrated Optics: Review" *J. Opt. Soc. Am. B* **2005**, 22, 240.

[33] B. E. A. Saleh and M. C. Teich, "*Fundamentals of Photonics*" Wiley-Interscience, **2007**.

[34] C. Z. Tan and J. Arndt, "Wavelength Dependence of the Faraday Effect in Glassy SiO_2" *J. Phys. Chem. Solids.* **1999**, 60, 1689.

[35] D. U. Bartholomew, J. K. Furdyna, and A. K. Ramdas, "Interband Faraday Rotation in Diluted Magnetic Semiconductors: $Zn_{1-x}Mn_xTe$ and $Cd_{1-x}Mn_xTe$" *Phys. Rev. B* **1986**, 34, 6943.

[36] S. Morris, T. Hawkins, P. Foy, J. Ballato, S. W. Martin, and R. Rice, "Cladding Glass Development for Semiconductor Core Optical Fibers" *Int. J. Appl. Glass. Sci.* **2012**, 3, 144.

[37] J. Ballato, T. Hawkins, P. Foy, R. Stolen, B. Kokuoz, M. Ellison, C. McMillen, J. Reppert, A. M. Rao, M. Daw, S. Sharma, R. Shori, O. Stafsudd, R. R. Rice, and D. R. Powers, "Silicon Optical Fiber" *Opt. Express* **2008**, 16, 18675.

[38] J. Ballato, T. Hawkins, P. Foy, B. Yazgan-Kokuoz, R. Stolen, C. McMillen, N. K. Hon, B. Jalali, and R. Rice, "Glass-Clad Single-Crystal Germanium Optical Fiber," *Opt. Express* **2009**, 17, 8029.

[39] J. Ballato, T. Hawkins, P. Foy, C. McMillen, L. Burka, J. Reppert, R. Podila, A. M. Rao, and R. R. Rice, "Binary III-V Semiconductor Core Optical Fiber" *Opt. Express* **2010**, 18, 4972.

[40] J. Ballato, T. Hawkins, P. Foy, B. Yazgan-Kokuoz, C. McMillen, L. Burka, S. Morris, R. Stolen, and R. Rice, "Advancements in Semiconductor Core Optical Fiber" *Opt. Fiber Technol.* **2010**, 16, 399.

[41] S. Morris, C. McMillen, T. Hawkins, P. Foy, R. Stolen, J. Ballato, and R. Rice, "The Influence of Core Geometry on the Crystallography of Silicon Optical Fiber" *J. Cryst. Growth* **2011**, 352, 53.

[42] S. Morris, T. Hawkins, P. Foy, C. McMillen, J. Fan, L. Zhu, R. Stolen, R. Rice, and J. Ballato, "Reactive Molten Core Fabrication of Silicon Optical Fiber" *Opt. Mater. Express* **2011**, 1, 1141.

[43] B. Scott, K. Wang, V. Caluori, and G. Pickrell, "Fabrication of Silicon Optical Fiber" *Opt. Eng.* **2009**, 48, 100501.

[44] B. L. Scott, K. Wang, and G. Pickrell, "Fabrication of n-Type Silicon Optical Fibers," *IEEE Photon. Technol. Lett.* **2009**, 21, 1798.

[45] G. Tao, A. F. Abouraddy, and A. M. Stolyarov, "Multimaterial Fibers" *Int. J. Appl. Glass Sci*. **2012**, 4, 349.

[46] M. Bayindir, F. Sorin, A. F. Abouraddy, J. Viens, S. D. Hart, J. D. Joannopoulos, and Y. Fink, "Metal-Insulator-Semiconductor Optoelectronic Fibres" *Nature* **2004**, 431, 826.

[47] S. Danto, F. Sorin, N. D. Orf, Z. Wang, S. A. Speakman, J. D. Joannopoulos, and Y. Fink, "Fiber Field-Effect Device Via in situ Channel Crystallization" *Adv. Mater.* **2010**, 22, 4162.

[48] A. M. Stolyarov, L. Wei, O. Shapira, F. Sorin, S. L. Chua, J. D. Joannopoulos, and Y. Fink, "Microfluidic Directional Emission Control of an Azimuthally Polarized Radial Fibre Laser" *Nature Photon.* **2012**, 6, 229.

[49] A. F. Abouraddy, M. Bayindir, G. Benoit, S. D. Hart, K. Kuriki, N. Orf, O. Shapira, F. Sorin, B. Temelkuran, and Y. Fink, "Towards Multimaterial Multifunctional Fibres that See, Hear, Sense and Communicate" *Nat. Mater.* **2007**, 6, 336.

[50] M. Bayindir, A. F. Abouraddy, J. Arnold, J. D. Joannopoulos, and Y. Fink, "Thermal-Sensing Fiber Devices by Multimaterial Codrawing" *Adv. Mater.* **2006**, 18, 845.

[51] S. Egusa, Z. Wang, N. Chocat, Z. M. Ruff, A. M. Stolyarov, D. Shemuly, F. Sorin, P. T. Rakich, J. D. Joannopoulos, and Y. Fink, "Multimaterial Piezoelectric Fibres" *Nat. Mater*. **2010**, 9, 643.

[52] B. Temelkuran, S. D. Hart, G. Benoit, J. D. Joannopoulos, and Y. Fink, "Wavelength-Scalable Hollow Optical Fibres with Large Photonic Bandgaps for CO_2 Laser Transmission" *Nature* **2002**, 420, 650.

[53] J. J. Kaufman, G. Tao, S. Shabahang, E. H. Banaei, D. S. Deng, X. Liang, S. G. Johnson, Y. Fink, and A. F. Abouraddy, "Structured Spheres Generated by an In-Fibre Fluid Instability" *Nature* **2012**, 487, 463.

[54] B. J. Eggleton, B. Luther-Davies, and K. Richardson, "Chalcogenide Photonics" *Nature Photon*. **2011**, 5, 141.

[55] N. D. Orf, O. Shapira, F. Sorin, S. Danto, M. A. Baldo, J. D. Joannopoulos, and Y. Fink, "Fiber Draw Synthesis" *Proc. Natl. Acad. Sci.* **2011**, 12, 4743.

[56] M. R. Henderson, B. C. Gibson, H. Ebendorff-Heidepriem, K. Kuan, S. Afshar V., J. O. Orwa, I. Aharonovich, S. Tomljenovic-Hanic, A. D. Greentree, S. Prawer, and T. M. Monro, "Diamond in Tellurite Glass: A New Medium for Quantum Information" *Adv. Mater*. **2011**, 23, 2806.

[57] P. R. Watekar, S. Ju, and W.T. Han, "Visible-to-Infrared Down-Conversion in the Silicon Nanoparticles-Doped Optical Fiber" *Curr. Appl. Phys.* **2009**, 9, S182.

[58] F. Pang, X. Zeng, Z. Chen, and T. Wang, "Fabrication and Characteristics of Silica Optical Fiber Doped with InP Nano-Semiconductor Material" *Opt. Quant. Electron.* **2008**, 39, 975.

[59] R. A. Mironov, E. V. Karaksina, A. O. Zabezhailov, R. M. Shapashnikov, M. F. Churbanov, and E. M. Dianov, "Mid-IR Luminescence of Cr^{2+}:II-VI Crystals in Chalcogenide Glass Fibres" *Quantum. Electron.* **2010**, 40, 828.

[60] I. Aharonovich, A. D. Greentree, and S. Prawer, "Diamond Photonics" *Nature Photon.* **2011**, 5, 397.

[61] N. Da, A. A. Enany, N. Granzow, M. A. Schmidt, P. St. J. Russell, and L. Wondraczek, "Interfacial Reactions Between Tellurite Melts and Silica During the Production of Microstructured Optical Devices" *J. of Non-Cryst. Solids* **2011**, 357, 1558.

[62] N. Da, L. Wondraczek, M. A. Schmidt, N. Granzow, and P. St. J. Russell, "High Index-Contrast All-Solid Photonic Crystal Fibers by Pressure-assisted Melt Infiltration of Silica Matrices" *J. Non-Cryst. Solids* **2010**, 356, 1829.

[63] M. A. Schmidt, N. Granzow, N. Da, M. Peng, L. Wondraczek, and P. At. J. Russell, "All-Solid Bandgap Guiding in Tellurite-Filled Silica Photonic Crystal Fibers" *Opt. Lett.* **2009**, 34, 1946.

[64] N. Granzow, S. P. Stark, M. A. Schmidt, A. S. Tverjanovich, L. Wondraczek, and P. St. J. Russell, "Supercontinuum Generation in Chalcogenide-Silica Step-Index Fibers" *Opt. Express* **2011**, 19, 21003.

[65] N. Granzow, P. Uebel, M. A. Schmidt, A. S. Tverjanovich, L. Wondraczek, and P. St. J. Russell "Bandgap Guidance in Hybrid Chalcogenide–Silica Photonic Crystal Fibers" *Opt. Lett.* **2011**, 36, 2432.

[66] B. T. Kuhlmey, B. J. Eggleton, and D. K. C. Wu, "Fluid-Filled Solid-Core Photonic Bandgap Fibers" *J. Lightw. Technol.* **2009**, 27, 1617.

[67] T. T. Larsen, A. Bjarklev, D. S. Hermann, and J. Broeng, "Optical Devices Based on Liquid Crystal Photonic Bandgap Fibres" *Opt. Express* **2003**, 11, 2589.

[68] F. Benabid, J. C. Knight, G. Antonopoulos, and P. St. J. Russell, "Stimulated Raman Scattering in Hydrogen-Filled Hollow-Core Photonic Crystal Fiber" *Science* **2002**, 298, 399.

[69] H. W. Lee, M. A. Schmidt, R. F. Russell, N. Y. Joly, H. K. Tyagi, P. Uebel, and P. St. J. Russell, "Pressure-Assisted Melt-Filling and Optical Characterization of Au Nano-Wires in Microstructured Fibers" *Opt. Express* **2011**, 19, 12180.

[70] S. H. Kim, H. Hwang, and S. M. Yang, "Fabrication of Robust Optical Fibers by Controlling Film Drainage of Colloids in Capillaries" *Angew. Chem. Int. Ed.* **2012**, 51, 3601.

[71] H. K. Tyagi, M. A. Schmidt, L. P. Sempere, and P. S. J. Russell, "Optical Properties of Photonic Crystal Fiber with Integral Micron-Sized Ge Wire" *Opt. Express* **2008**, 16, 17227.

[72] J. A. Harrington, "A Review of IR Transmitting, Hollow Waveguides" *Fiber Integrated Opt.* **2000**, 19, 211.

[73] P. J. A. Sazio, A. Amezcua-Correa, C. E. Finlayson, J. R. Hayes, T. J. Scheidemantel, N. F. Baril, B. R. Jackson, D. J. Won, F. Zhang, E. R. Margine, V. Gopalan, V. H. Crespi, and J. V. Badding, "Microstructured Optical Fibers as High-Pressure Microfluidic Reactors" *Science* **2006**, 311, 1583.

Chapter 2

Fundamental Aspects of High Pressure Chemical Vapor Deposition

Before moving into the complex chemistry for the deposition of II-VI semiconductors at high pressure, it is important to understand the fundamental aspects of reactions that occur at high pressures within confined capillary geometries. Throughout this chapter, SiH_4 pyrolysis will be treated as the model system as its reaction dynamics are very well known at atmospheric conditions. Also, it was one of the first systems studied in HPCVD, making it the most well understood reaction. The principles that are developed with the SiH_4 chemistry can then be applied to II-VI semiconductor chemistries.

2.1 Limitations of Conventional CVD/ALD

Conventional chemical vapor deposition (CVD) techniques, such as low pressure chemical vapor deposition (LPCVD), atmospheric pressure chemical vapor deposition (APCVD), and plasma enhanced chemical vapor deposition (PECVD), are among the most powerful and widely used materials fabrication techniques and are well suited for the fabrication of planar thin films. The reactors for these CVD techniques have typically been designed with a view towards deposition on large area substrates and much effort is spent in conventional CVD reactors to configure them to deposit uniform thickness layers on substrates. The balance between surface reaction rate and precursor transport is carefully controlled to achieve this goal. However, these techniques are limited in their ability to uniformly and conformally coat and/or fill extreme aspect ratio voids and trenches with well-developed, uniform thickness films. The ability to conformally coat these features is of particular value in the synthesis of geometrically complex, three-

dimensional materials that are hierarchically organized across a range of length scales. Specifically, conformally coating the pores of MOFs is of particular interest in this dissertation. Additional examples where the coating of complex templates is valuable include pillar array photovoltaics,[1] intricate microfluidic channels and in-channel microfluidic devices,[2] nanoscale biological templates,[3] three-dimensional optical metamaterials,[4] and three-dimensional electronics.

Atomic layer deposition (ALD) has been the most viable technique for conformally coating high aspect ratio micro/nanostructures with semiconductors because the self-limiting nature of the deposited film allows for uniform film thickness despite variations in the precursor flux to the surface.[5-7] However, the requirement for self-limited chemical reaction and thermal stability at the desired growth temperature places limits on the range of precursor molecules that can be employed and thus the accessible materials. Moreover, the layer-by-layer nature of the process greatly limits the overall rate of deposition.[8,9] CVD allows for higher rates of deposition of semiconductor materials than ALD and does not require self-limiting chemical reactions; thus it is desirable to develop CVD chemistry that has the highly conformal nature of ALD. In this chapter, it will be shown that HPCVD combines the advantages of both ALD and CVD.

2.2 Pressure Enabled Mass Transport

The poor ability of conventional CVD to conformally coat deep nanoscale voids or pores with semiconductors arises because the mean free path for molecules at the atmospheric or sub-atmospheric pressures typically employed is hundreds of nanometers or more. The mean free path of a gas molecule can be calculated using the kinetic theory of gases and is inversely proportional to pressure:[10]

$$l = \frac{k_B T}{\sqrt{2}\pi d^2 P}$$

(**Equation 2.1**)

where k_B is Boltzmann's constant, T is temperature, P is pressure, and d is the kinetic diameter of the molecule.

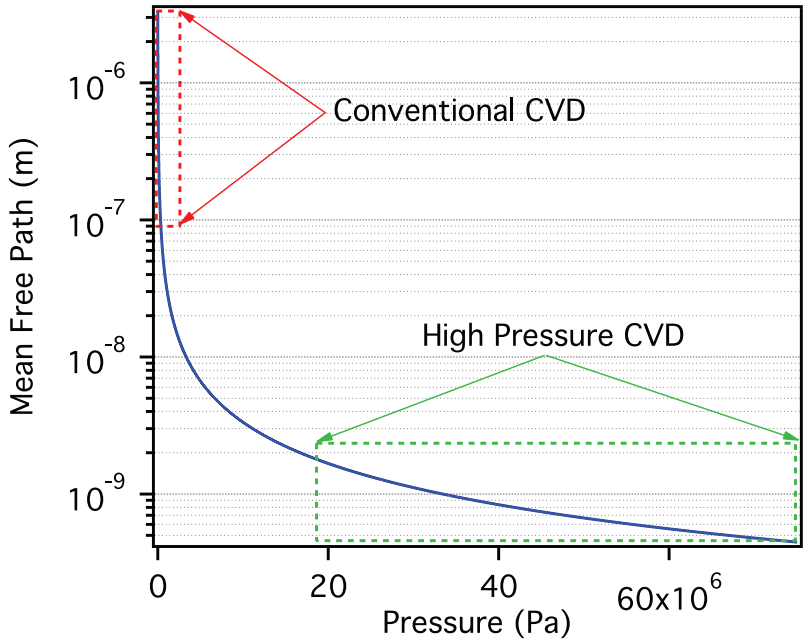

Figure 2.1: Mean free path of H_2 as a function of pressure at 400 °C.

The mean free path of a H_2 molecule at 400 °C is approximately 300 nm at the atmospheric pressures employed in conventional CVD compared to about 1 nm at the 35 MPa pressures used in HPCVD (**Figure 2.1**). In conventional CVD, effusion of molecules into nanoscale openings is the primary transport mechanism (**Figure 2.2**).[10] Thus the transport into these openings is relatively slow. However, at high pressures, on the order of tens of MPa, the molecular mean free path that is on the order of 1 nm allows for pressure driven transport by hydrodynamic flow into micro/nanoscale voids. The rate of mass transport to micro/nanoscale voids and features then becomes nearly equal to the rate of transport to macroscale features. Thus, HPCVD can conformally coat surfaces with semiconductor films yet still allow for a higher rate

of deposition than ALD and access to the wide range of precursor chemistries possible with CVD. Additionally, if the high pressure mixture is allowed to flow through a reactor, as is possible with a capillary of a MOF, there is a significant increase in mass transport into high aspect ratio structures without relying on slower diffusion processes.

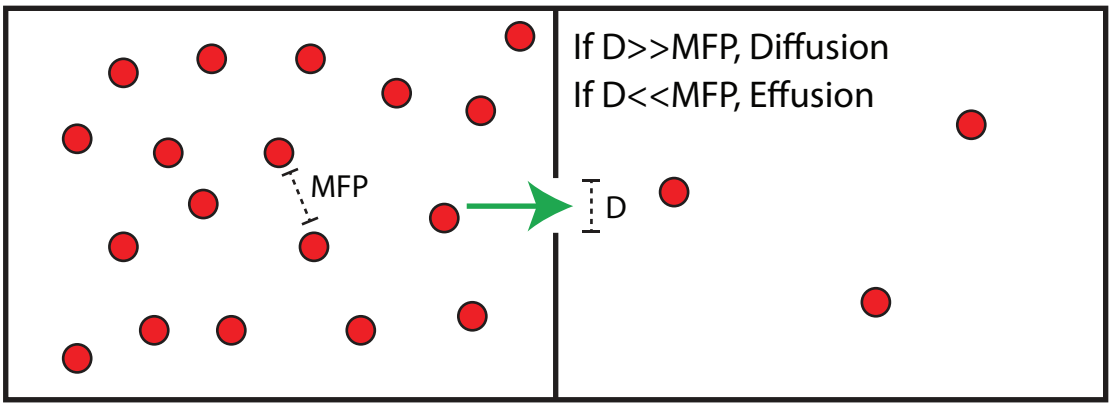

Figure 2.2: Effusion versus diffusion. When infiltrating a very small pore with gas molecules, a small mean free path results in a diffusion driven process, rather than effusion, leading to hydrodynamic flow.

The hydrodynamic flow through a CVD reactor plays a major role in the resulting properties of the deposited material. The high pressure flow through capillaries has been characterized by experimental studies of helium gas flow. These capillaries are the reactors in which films of semiconductors will be deposited (described in the next section). The volumetric flow rate through the capillaries was measured as a function of pressure at constant capillary diameter and as a function of diameter at a constant pressure. As shown in **Figure 2.3**, the flow scales with the square of pressure, and with the fourth power of the diameter. Note that at larger capillary diameters, the data does not fit the curve, implying that the flow is no longer laminar and transitions to turbulent. Turbulent flow will have a significant impact on the growth of films, as the mass transport of precursor molecules to the silica walls from the center of the capillary will not be uniform along the length. However, the majority of the reactions presented in this dissertation will take place in the laminar flow regime.

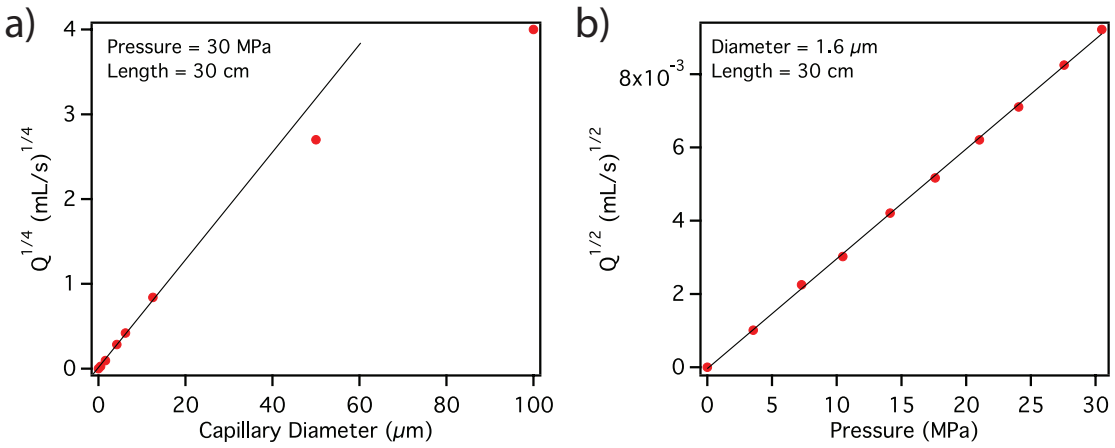

Figure 2.3: Compressible laminar flow in micro-capillaries. The mass flow rate is proportional to D^4 (a) and P^2 (b).

Thus the flow is approximated as compressible laminar[11] and can be expressed as:

$$Q \propto \frac{\pi \Delta P^2 D^4}{8 \eta L}$$

(**Equation 2.2**)

where ΔP is the pressure difference, D is the diameter, η is the viscosity, and L is the length of the capillary. The rate of mass transport into a given capillary diameter can thus be controlled with pressure and length, which can significantly influence the grain growth in a polycrystalline film. It is worth noting that the large pressure differences and confined geometries alter reactant diffusion as well as the flow,[12] especially in the all-important boundary layer in the immediate vicinity of the surface chemical reaction.[13]

2.3 Overview of the HPCVD Process

An important practical difference in HPCVD is that reaction precursors must often be transported together for delivery into a heated reaction zone whereas conventional CVD reactors typically allow for the introduction of precursors separately to avoid prereaction before they reach

a planar deposition target (**Figure 2.4a**).[14] Thus the precursors selected for HPCVD must be chosen so that they do not prereact as they are transported to a desired deposition location at low temperature, yet do react once they reach the desired target and are thermally activated.

In a typical HPCVD reaction, a high pressure precursor mixture is configured to flow into a capillary. The mixture consists of the precursor molecules (kPa to MPa pressures) that are pressurized with a carrier gas such as helium or H_2 to a total pressure of 35 – 70 MPa. This precursor mixture is introduced into a high pressure reservoir. This reservoir can be made from parts such as high pressure tubing, fittings, and valves from Superpressure and High Pressure Equipment companies. The precursors can be introduced into the reservoir either by cryogenic condensation, if their condensation temperatures are high enough, or by means of a suitable high pressure pump. Pumps such as stainless steel diaphragm pumps are well suited for this purpose. They do not introduce oil or other types of impurities as the gas being pumped only comes into contact with clean, dry, corrosion resistant metal surfaces and suitably chosen, chemically inert o-rings. Once the precursor and carrier mixture is loaded into the reservoir, the capillary is attached to it and evacuated. Next, the valve on the reservoir is opened and the high pressure precursor flows down the fiber pores. The other end of the capillary is open to atmospheric pressure. This pressure difference is thus an additional driving force for the introduction of precursors into the MOF pores. Upon heating the capillary with a furnace, reaction occurs to deposit layers and wires within its pores (**Figure 2.4b**). Unreacted precursors, carrier gas, and reaction byproducts are carried out of the fiber downstream. Multiple layers may be deposited by successively introducing different precursors. Patterning of the deposition along the length of the fiber by laser-induced photochemical or thermal decomposition is also possible.[15]

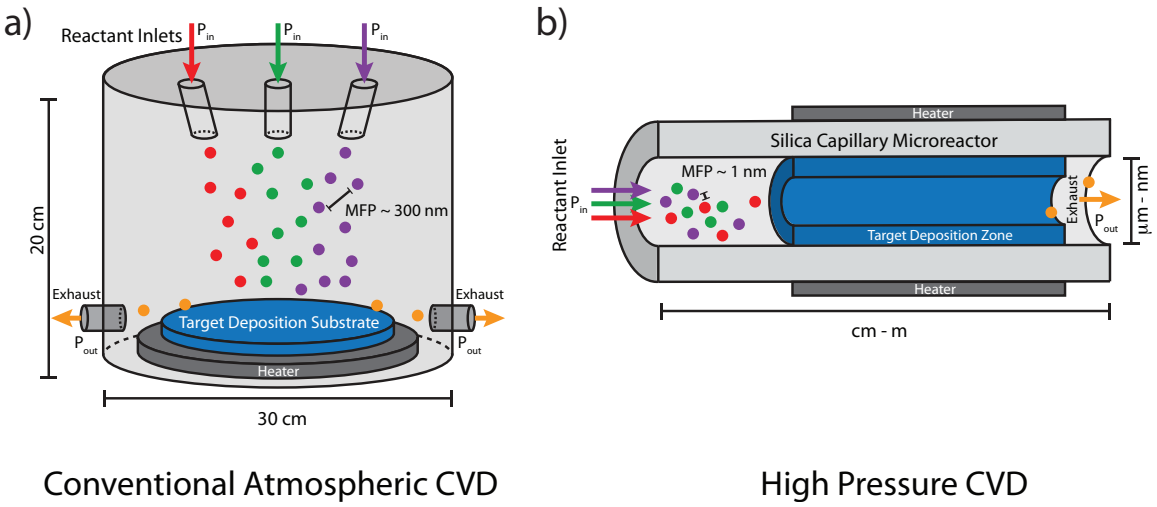

Figure 2.4: Comparison of CVD to HPCVD.[16] (a) Schematic of atmospheric CVD process, where source molecules can be introduced to a heated substrate separately such that prereaction can, in general, be avoided. Flow towards the substrate is achieved via a small pressure difference with the exhaust ports. (b) Schematic of HPCVD in a capillary microreactor, where a high pressure precursor mixture of source molecules is configured to flow into a capillary (left) with the opposite end open to atmosphere (right). In the unheated region of the capillary, precursor molecules are so intimately mixed that any tendency to prereact at low temperatures must be avoided. When the capillary is heated, well-developed annular films are deposited, while unreacted precursors, carrier gas, and reaction byproducts are exhausted downstream.

2.3.1 Comparison to Drawing Techniques

HPCVD allows for fabrication of semiconductor wires and layers from electronic grade chemical precursors, making it possible obtain high purity materials if the standard semiconductor fabrication protocols are followed for insuring contaminants are not incorporated into the precursors during handling. Oxidation of the core from the silica cladding, which is a major challenge in drawing techniques presented in **Chapter 1**, is straightforward to avoid owing to the relatively low temperatures of CVD reactions. Optical fiber cores with dimensions of a few micrometers or less, which are preferred for single mode guidance, have higher surface area to volume ratios than the large core unary semiconductor fibers that have been fabricated by

drawing techniques. Impurities enter into the fiber cores from the surface; thus the ability to make high chemical purity nanoscale diameter semiconductor fiber cores is a strength of HPCVD.[15,16]

The film growth is a layer by layer process such that films and layers with very sharp interfaces can readily be deposited with low temperature processing. Precisely configured interfaces that allow for optoelectronic junctions with built-in electric potential can thus be formed.[17] Such junctions are central to modern optoelectronics, as the junction potential can quickly sweep out carriers and be used to control the flow of electrons. The low viscosity and high chemical reactivity of melted crystalline unary and compound semiconductors make it difficult to draw precise, sharply defined layers of these materials. It is also not yet clear if patterned arrays of closely spaced crystalline semiconductor wires can be drawn as well, as the fraction of low viscosity melt in this array would be high. Furthermore, HPCVD can deposit films at very low temperatures compared to drawing and allow for materials to be deposited in amorphous,[18] polycrystalline,[19] or even single crystalline[20] form. Another advantage of low temperature processing of high temperature materials is that it removes many of the thermal constraints associated with the drawing methods while still maintaining the properties of a robust silica based optical fiber.

The use of templates fabricated via the mature silica fiber drawing process also has several advantages. The inner air/silica surfaces of silica capillaries and MOFs are nearly atomically smooth,[21] such that the materials that are deposited on this surface template it nearly perfectly and result in atomically smooth outer surfaces.[22] This minimizes roughness at the silica/deposited material interface while maintaining a uniform cross-section along the length, which is paramount to minimizing optical loss due to geometry imperfections. Furthermore, the HPCVD fibers can be spliced into existing silica fiber infrastructure.[17] Since the silica MOFs can have micro/nanopores arranged in nearly any shape or pattern, they can be used as complex 2D

templates to arrange semiconductor materials precisely. This allows for the microstructure of the resulting optical fiber to be readily controlled in the transverse plane.

2.4 Pressure Effects on Reactions

Not only does pressure allow for the infiltration of precursor molecules into the pores of MOFs to chemically deposit materials, it also significantly alters the chemistry of the deposition reaction. HPCVD is remarkably different from conventional CVD because the high pressures employed affect many deposition characteristics such as reaction kinetics, thermodynamics, and surface chemistry.

2.4.1 Reaction Kinetics of Silane Pyrolysis

The chemical kinetics of the system are vastly altered because of the increased number of molecular collisions of both precursor and carrier molecules. This is a direct result of the nanoscale mean free path experienced by the molecules at high pressure. These effects can be calculated for the first step of SiH_4 pyrolysis.

The reaction pathway from SiH_4 reactant to crystalline or amorphous silicon products in conventional CVD is thought to involve many gas phase and/or surface steps.[23,24] High pressure will alter the mechanism for this reaction, as evidenced by the change in reaction order for homogeneous gas phase reaction of SiH_4 in large volume reactors.[25-27] Despite the complexity of the SiH_4 reaction mechanism,[23] some generalizations can be made. First, the rates of gas phase reactions can be expected to increase at high pressure because collisional activation increases the rate constant up to a limit and also because reactant concentrations are high.[18] The SiH_4 molecule is thermodynamically unstable, but kinetically stable at temperatures below ~550 °C

because of a large activation barrier to decomposition.[23] In the gas phase, the following reaction to form SiH_2 (silylene) is thought to be the first step in the pyrolysis of SiH_4:[23]

$$SiH_{4(g)} \rightarrow SiH_{2(g)} + H_{2(g)} \qquad \textbf{(Reaction 2.1)}$$

The rate expression for this reaction is usually written in its unimolecular form, although bimolecular collision with carrier molecules and other SiH_4 molecules is critical to the activation step. The reaction rate, with the Arrhenius expression for the rate constant is given by:

$$-\frac{d[SiH_4]}{dt} = Ae^{-\frac{E_a}{k_B T}}[SiH_4] \qquad \textbf{(Equation 2.3)}$$

where E_a is the activation energy, k_B is Boltzmann's constant, T is temperature, and A is the pre-exponential factor. When the rate expression is written this way, it is dependent on the temperature, the total pressure, and the identity of the colliding bath gas molecules (which affect the pre-exponential factor, A). The SiH_4 molecule has no low frequency vibrations and thus its unimolecular decomposition is not at the high pressure limit under conventional CVD conditions.[28] Quantum Rice-Ramsperger-Kassel theory modeling can be used to calculate the unimolecular decomposition rate constant as a function of the total pressure of both carrier gas (helium carrier in the case of HPCVD of silicon) and SiH_4 (**Figure 2.5**).[18] The increase in molecular collision rate per unit time with increasing pressure increases the reaction rate until the high pressure limit. Thus, the reaction rate constant at 420 °C can be increased considerably from 1.6×10^{-7} s^{-1} at 13 Pa (typical LPCVD pressure) to 4.6×10^{-4} s^{-1} at the high pressure limit of ~10 MPa. Relative to LPCVD reaction conditions, the $\sim 10^5$ fold increase in reaction concentration under typical HPCVD conditions (13 Pa versus 1.7 MPa partial pressure SiH_4) together with the $\sim 10^3$ fold increase in rate constant can be expected to considerably increase the rate of decomposition of SiH_4 to SiH_2.

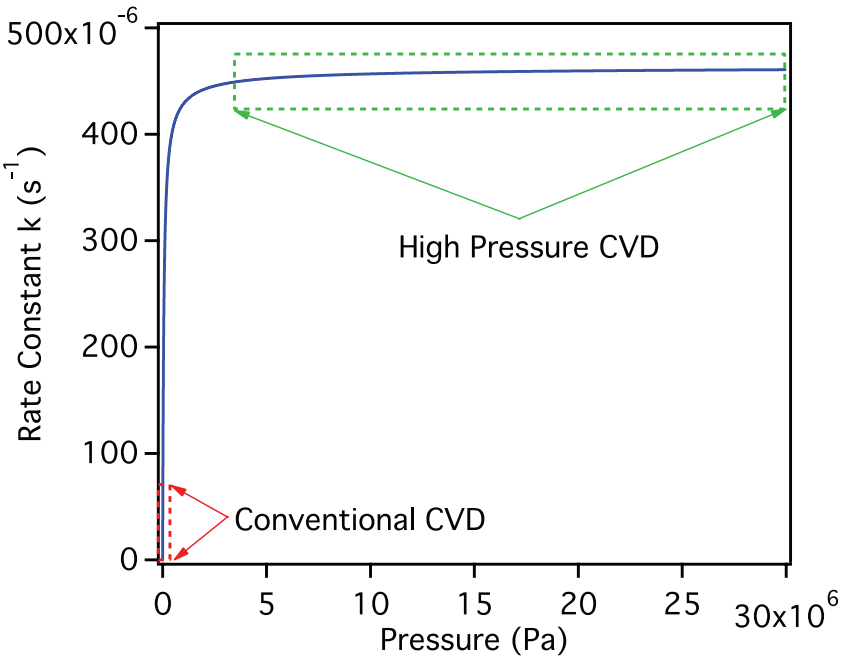

Figure 2.5: Rate constant of the first step of silane pyrolysis as a function of pressure at 420 °C in helium predicted by Rice-Ramsperger-Kassel calculations.

The SiH_2 intermediate can be expected to then react with SiH_4 and other species in a complex series of reactions that lead to solid silicon.[24] Each of these reaction steps may be accelerated in a manner similar to that of the SiH_2 formation reaction as a result of both increased rate constant due to collisional activation and higher intermediate concentration. Experimentally it is found that the increase in deposition rate is ~30 fold at 450 °C, from 0.01 $Å s^{-1}$ reported for LPCVD at a pressure of 13 Pa[29] to ~0.3 $Å s^{-1}$ for HPCVD SiH_4 at a partial pressure of 1.7 MPa. Thus it is clear that some acceleration occurs, but it is not as large as that expected for the increase in the concentration of intermediates such as SiH_2.[18] A detailed modeling study would be required to quantitatively account for the effect of high pressure on film deposition rates. It may be that surface reactions lead to a rate-limiting step in view of the high concentration of reactive intermediates in the gas phase.

Dopants may be added to the precursor mixture to control the electron or hole concentration in the deposited materials in HPCVD.[17] It has been found that the addition of dopant precursors can catalyze the HPCVD SiH_4 reaction. For example, the reaction rate at 400 °C and 1.7 MPa partial pressure can be accelerated dramatically from <1 $Å s^{-1}$ to ~50 $Å s^{-1}$ when ~1 at% B_2H_6 is added; a similar trend is observed for conventional CVD.[17] Adding ~1 at% PH_3 also slightly increases the reaction rate, albeit only by 2 – 3 $Å s^{-1}$ at 500 °C and the same partial pressure. This increase is in contrast to the trend observed for conventional CVD, where there is a decrease in reaction rate with phosphorus addition that is thought to be associated with blockage of surface adsorption by phosphorus species. It may be that the high concentration of reactive intermediates at high pressure competes effectively with the phosphorus for the adsorption sites. The reaction intermediates could be altered by the presence of phosphorus to form species such as SiH_3PH_2 that may play a role in the increased rate of deposition.[17] Again a complete understanding will require a full investigation by means of a combination of modeling and experiment.

2.4.2 Thermodynamics

Increasing the pressure of a system alters collisionally based reaction dynamics as well as the chemical potential of the reactant species. In chemical reactions, one typically activates a reaction by increasing the temperature to change the chemical potential of a molecule and make it reactive. However, the same activation can be achieved by changing the pressure of the system without heating. This is because chemical thermodynamics are altered by the volume-pressure term ($V\Delta P$) in the expression for the Gibbs free energy. From the equation of state of a system, the effects of pressure on thermodynamic quantities can be calculated. For H_2, increasing the pressure of the system results in an increased chemical potential of the molecule (**Figure 2.6**).[30]

This is embodied in the hydrogen embrittlement of steel, where high pressure H_2 gas can react with the carbon in the steel and weaken it.[31,32] When coupled with the kinetic effects, the thermodynamic effects result in higher reaction rates of CVD reactions and allows for reactions to occur at temperatures much lower than that needed in conventional CVD. This is highlighted in **Chapter 3** for the deposition of hydrogenated amorphous silicon and **Chapter 4** for ZnO.

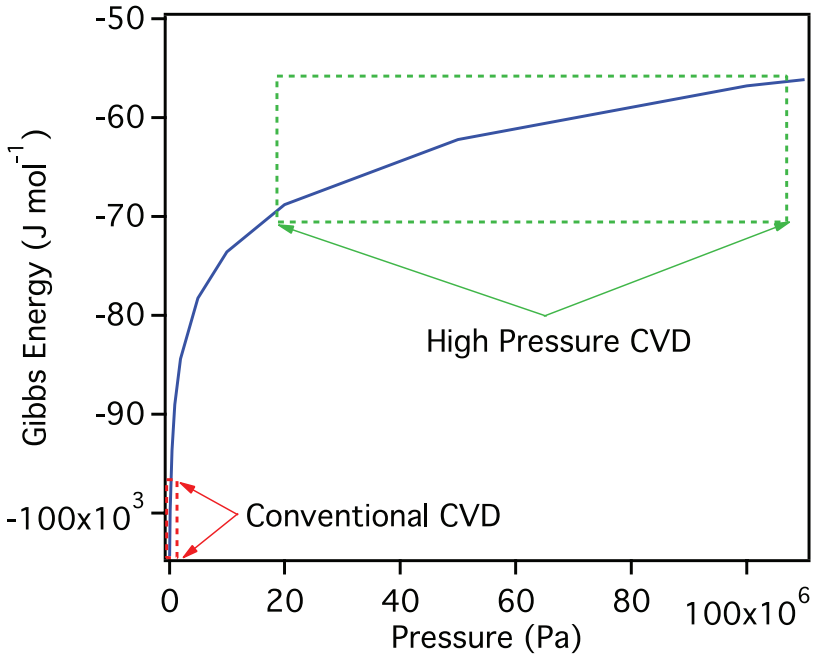

Figure 2.6: The chemical potential of H_2 as a function of pressure. Data from: [30].

2.4.3 Surface Area to Volume Effects

The concentrations of precursor employed for HPCVD may be orders of magnitude higher than those employed for conventional CVD processes. When using higher precursor pressures, there are many more molecular/cluster collisions, which can lead to the formation of undesirable particles that grow homogeneously in the gas phase, instead of the desired heterogeneous growth of a film. It is known that larger reactors with dimensions on the order of centimeters predominantly produce particles when too high of a precursor pressure is used.[27]

However, the confinement aspects of HPCVD in micrometer diameter capillaries have a significant influence on the competition between surface and gas phase reactions. A typical result of using a large, bulk reactor is shown in **Figure 2.7a**, where silicon particles are produced in a predominantly homogenous reaction. When a large 2.5 mm internal diameter capillary is used for deposition in HPCVD (**Figure 2.7b**), undesired silicon particles are still formed along with a film. This is at the threshold of particle/film growth, so both are observed. Well-developed films are only formed when the capillary diameter, or reactor, is confined to <300 μm. In the confined geometry, any particles that form homogenously have little time to grow into larger particles before reaching the pore walls and become embedded in the growing film. The time required for a nucleated particle to reach the pore wall scales as x^2/D, where x is the pore diameter and D is the gas phase diffusivity of the particle. x^2/D is orders of magnitude smaller in 6 μm pores than in pores ≥300 μm, which results in the growth of a film (**Figure 2.7c**). The resulting morphology of silicon deposition in different sized capillaries, or reactors, is shown in **Figure 2.7**.

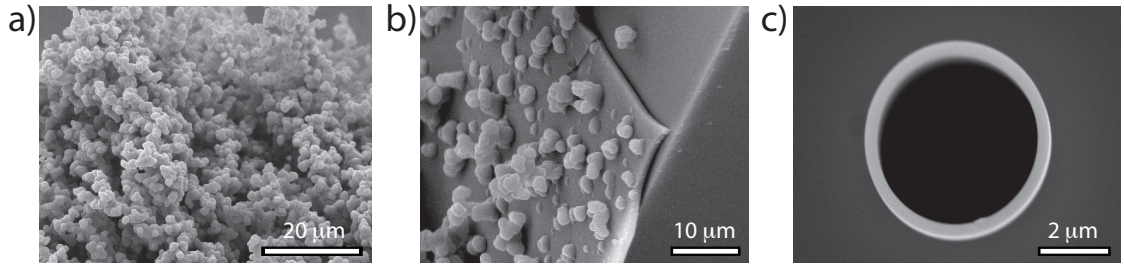

Figure 2.7: Growth of silicon as a function of surface area to volume ratio. Silicon particles are produced by deposition in a bulk reactor (a). A transition from particles to a film is observed in a 2.5 mm tube (b),[18] while completely heterogeneous deposition is observed when the capillary diameter is <300 μm (c). Image credit (a,b): Todd D. Day.

2.5 Pyrolysis of Silane: Understanding the HPCVD Complete Filling Processes

Pressure influences many aspects of a CVD reaction, which leads to some surprising results. One striking result of the HPCVD process in microscale capillaries is that it can result in

a void-free, completely filled semiconductor wire of centimeter length scales. At first glance, completely filling the capillaries of MOFs over lengths of centimeters or more appears to be challenging in view of their extreme aspect ratios. Precursors need to be transported into the channel and decompose into semiconductor to further fill the channel while reaction byproducts must be transported out of the channel. It might be expected that as soon as a location along the length of the growing annular film becomes clogged and transport of the reaction byproduct (H_2) is inhibited, the deposition reaction:

$$SiH_{4(g)} \rightarrow Si_{(s)} + H_{2(g)} \qquad \textbf{(Reaction 2.2)}$$

will shift back to the left and the forward reaction will become inhibited according to Le Chatelier's principle. However, the deposition rate can actually increase as the pore clogs, allowing the remainder of the void to be completely filled. Through both experiment and modeling (in collaboration with the Borhan group, Chemical Engineering, PSU), an understanding of this process, which is referred to as "backfilling", has been developed.[12]

For the following experiments and modeling, a 15 cm furnace was used to deposit silicon from SiH_4 at 500 °C. The high pressure mixture consists of 2 MPa of SiH_4 and 33 MPa of helium. Since the reservoir from which the precursor mixture is introduced into the capillary cannot be at the deposition temperature, it is inevitable that there will be a temperature gradient at some point along the length of the capillary; in these experiments there is a temperature maximum at about 7.8 cm from the furnace entrance (**Figure 2.8a**). The overall capillary length is 30 cm with an internal diameter of 6.2 μm; there are 5 cm of capillary between the high pressure source and the start of the furnace. Deposition was arrested after 3, 9, and 15 hours and scanning electron microscopy (SEM) cross-sections were collected along the length of the pore by Neil F. Baril. Deposition profiles from these cross-sections allow for visualization of the axial profile of the film thickness (**Figure 2.8b**). The process of complete filling can be broken down into three phases.[12]

In phase I, which occurs for the first few minutes of deposition, the film is thin enough to have minimal impact on the deposition. Under these conditions, the axial pressure profile can be computed using Fanno flow analysis.[33] The total pressure decreases from 30 MPa at the furnace entrance to 20 MPa at the furnace exit 15 cm downstream (**Figure 2.8a**). The effect of temperature on film growth rate is exponential while that of SiH_4 partial pressure is linear. Thus, in phase I, the effect of the increasing temperature on film growth rate dominates over the slightly hindering effect of decreasing SiH_4 partial pressure along the length of the pore leading to a maximum in the growth rate at the maximum wall temperature (**Figure 2.8c**).

After a few minutes of deposition, the reaction enters phase II. In phase II, the growing film impacts the deposition process by forming a convergent-divergent nozzle around the axial node of maximum growth rate (**Figure 2.8b**). The nozzle causes the flow to change from subsonic to supersonic as it passes through the region of maximum constriction. This supersonic flow gives rise to an unstable feedback loop that accelerates growth at the nozzle relative to locations downstream from it. After ~9 hours, as seen in profile B (**Figure 2.8b**) the flow rate is dramatically reduced by closure of the pore to less than 1 μm in diameter. The deposition rate in phase II remains highest at the first node (7.8 cm downstream of the furnace entrance), but begins to increase upstream as the throat closes down and the deposition gradually enters phase III.

In phase III, which is entered after approximately 9 hours, the growth at the nozzle has closed such that flow is nearly or completely extinguished. Deposition does not halt in phase III, which is termed the “no flow” regime, because the silica walls of the capillary are permeable to the H_2 reaction byproduct and the helium carrier gas, especially at the high temperatures used for deposition. For reference, the kinetic diameters of He and H_2 are 2.0 Å and 2.5 Å, respectively, while the silica has interstitial spacing of ~ 3 Å. Thus, SiH_4 can continue to enter the capillary void despite the extinguished flow. Moreover, any unreacted SiH_4 can no longer exit the capillary because this molecule is too large (3.6 Å) to travel through the silica capillary walls. The helium

continues to flow, however, drawing more SiH_4 molecules with it, forming a "kinetic pump" that can increase the SiH_4 concentration in the capillary to above that in the reservoir. This increased SiH_4 concentration can then accelerate the reaction rate several centimeters upstream from the initial plug (**Figure 2.8b**). The continued deposition allows for void free filling upstream of the nozzle closure.

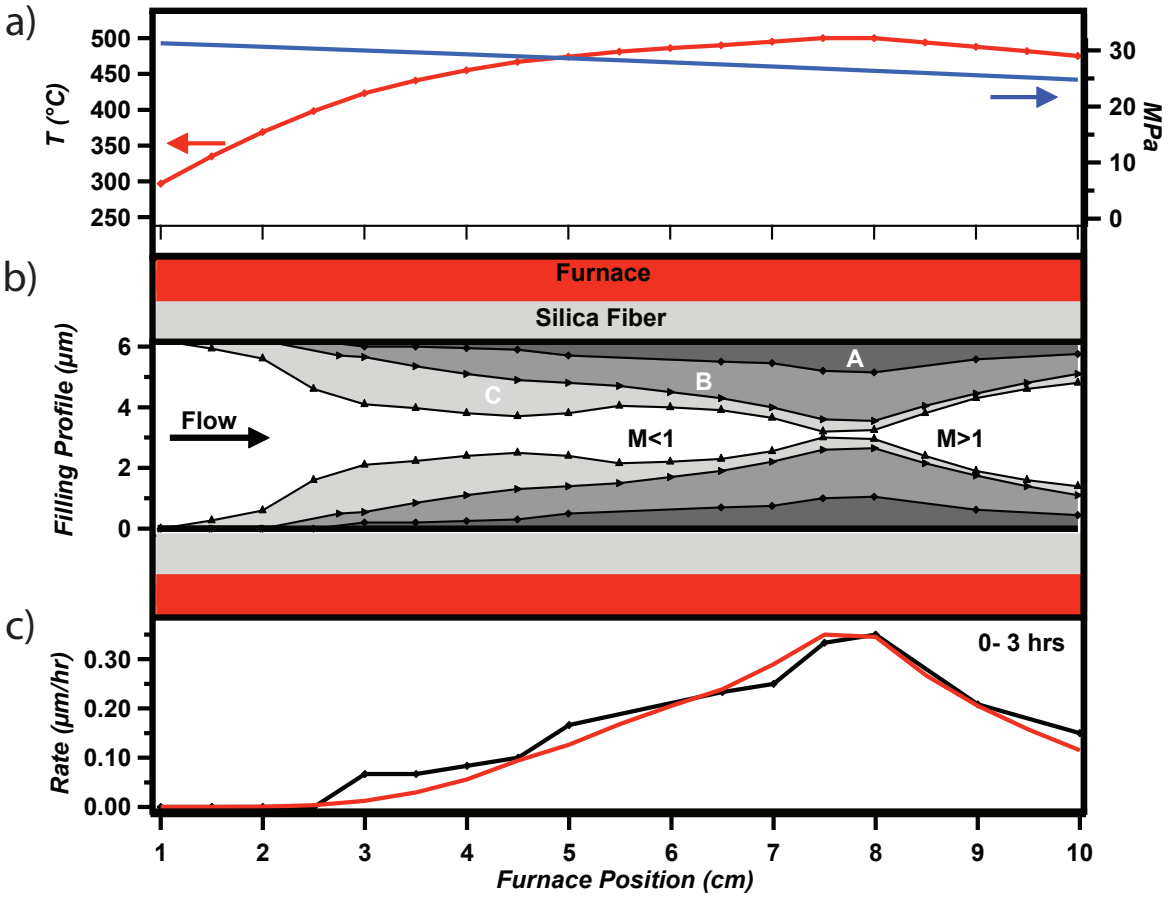

Figure 2.8: The three phases of complete filling.[12] a) The axial furnace temperature profile (red) and the axial pore pressure profile (blue) in phase I before the growing film impacts flow. b) Profiles determined from SEM cross-sections for a 3 (A), 9 (B), and 15 (C) hour depositions. Credit: Neil F. Baril. c) Calculated initial reaction rate (red) based on the temperature, pressure, and the Mach number of the gas mixture flowing through the pore (Borhan group) compared with the experimentally determined deposition rate (black) from 0 – 3 hours from profile A.

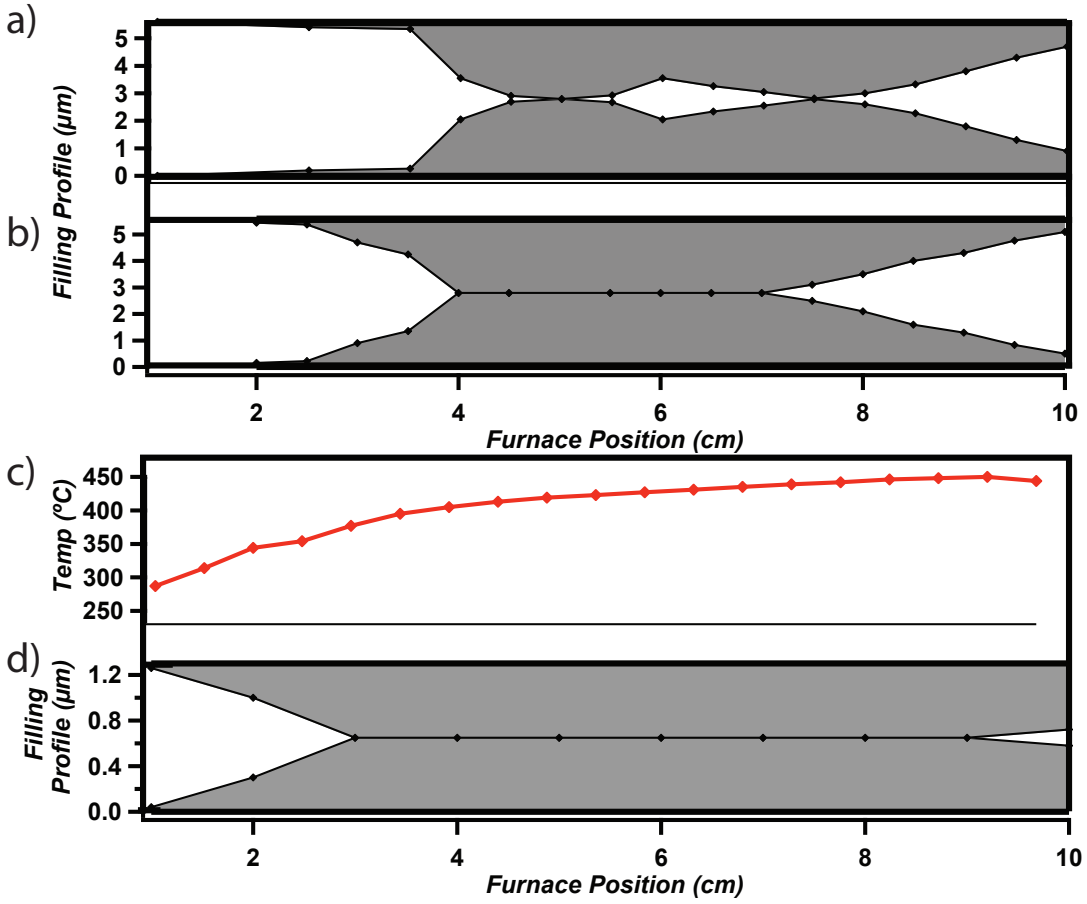

Figure 2.9: Control over plug formation and backfilling.[12] (a) A gap forms upstream of the first node as a result of the increased reaction rate. (b) Profile of a deposition with a 48 hour temperature ramp from 400 to 500 °C. (c) Furnace temperature profile for filling a 1.3 μm diameter pore. d) Profile of deposition within this 1.3 μm pore with a 48 hour temperature ramp from 380 to 450 °C.

With the understanding of the mechanism of in-pore HPCVD developed, it becomes possible to design deposition conditions that allow for complete filling of the micrometer diameter pores over distances of several centimeters via this backfilling process. Once closure at the first node has occurred, if growth occurs too rapidly at the second node closer to the furnace entrance, the pore will plug at this node and an undesirable gap in the filling between it and the first node is formed (**Figure 2.9a**). By slowly ramping up the temperature of the furnace over a period of 48 hours to 500 °C while precursor is flowing, it is possible to avoid this gap (**Figure**

2.9b). This temperature ramp allows for a greater fraction of the deposition to occur at lower temperatures than those used in the above experiments for which a fixed temperature was employed. At these lower temperatures the rate of helium diffusion through the pore walls is slower, which decreases the magnitude of the concentration gradient that arises due to this diffusion and allows for even filling over 3 cm (**Figure 2.9b**). In contrast, if the temperature is ramped over 24 hours, the rate of deposition at the second node is too high and the gap develops.

Modification of the furnace temperature profile (**Figure 2.9c**) allows for void free deposition of silicon in a 1.3 μm diameter pore over distances of 6 cm (**Figure 2.9d**). The maximum in the temperature of the furnace in this profile is at 9.5 cm instead of at 7.8 cm, which allows for backfilling after pore closure over a longer distance to produce a longer wire. For even longer lengths, the furnace, or fiber, could be translated in a controlled manner to slowly move the backfilling plug along much longer distances. A transmitted optical micrograph of this backfilling interface of an annealed silicon wire is shown in **Figure 2.10**. In the backfilling process, a nanoscale hole is slowly being filled back towards the high pressure source, which highlights the ability of HPCVD to infiltrate very high aspect ratio voids with precursor molecules.

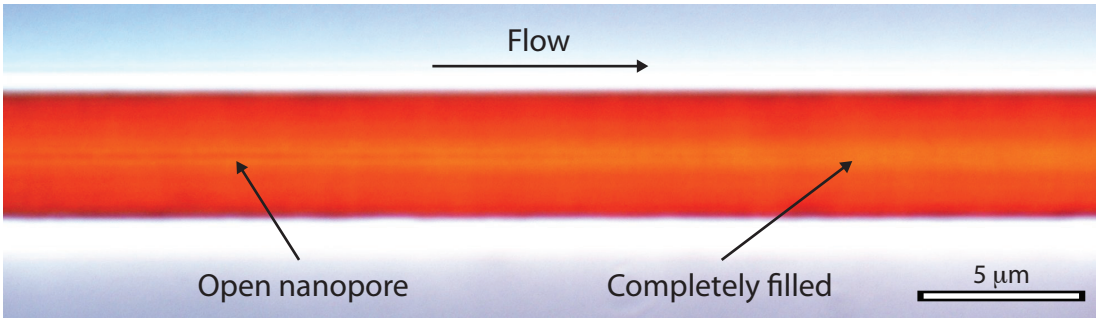

Figure 2.10: Optical micrograph of the backfilling interface.[12] When viewing an annealed polycrystalline silicon wire in transmitted light, the silicon is transparent and the central pore in which backfilling occurs can be seen. Image credit: Neil F. Baril.

2.6 Moving to More Complex Structures / Chemistries

With a thorough understand of the reaction kinetics, thermodynamics, and flow dynamics effects on the filling of high aspect ratio pores, optical fibers based on completely filled capillaries can be realized. Complex MOF templates can be filled to fabricate very unique semiconductor waveguides that are presented in **Chapter 3**. Furthermore, significantly more complex reactions can be investigated to deposit compound II-VI semiconductors such as ZnSe, which will be discussed in **Chapter 4**.

2.7 References

[1] E. C. Garnett, M. L. Brongersma, Y. Cui, and M. D. McGeHee, "Nanowire Solar Cells" *Annu. Rev. Mater. Res.* **2011**, 41, 269.

[2] G. M. Whitesides, "The Origins and the Future of Microfluidics" *Nature* **2011**, 442, 368.

[3] M. R. Jorgensen and M. H. Bartl, "Biotemplating Routes to Three-Dimensional Photonic Crystals" *J. Mater. Chem.* **2011**, 21, 10583.

[4] C. M. Soukoulis and M. Wegener, "Past Achievements and Future Challenges in the Development of Three-Dimensional Photonic Metamaterials" *Nature Photon*. **2011**, 5, 523.

[5] J. J. Wang, X. Deng, R. Varghese, A. Nikolov, P. Sciortino, F. Liu, L. Chen, and X. Liu, "Filling High Aspect-Ratio Nano-Structures by Atomic Layer Deposition and its Applications in Nano-Optic Devices and Integrations" *J. Vac. Sci. Technol*. **2005**, 23, 3209.

[6] S. M. George, "Atomic Layer Deposition: An Overview" *Chem. Rev.* **2010**, 110, 111.

[7] X. Meng, Y. Zhang, S. Sun, R. Li, and X. Sun, "Three Growth Modes and Mechanisms for Highly Structure-Tunable SnO_2 Nanotube Arrays of Template-Directed Atomic Layer Deposition" *J. Mater. Chem.* **2011**, 21, 12321.

[8] R. K. Puurunen, "Surface Chemistry of Atomic Layer Deposition: A Case Study for the Trimethylaluminum/water Process" *J. Appl. Phys*. **2005**, 97, 121301.

[9] L. Reijnen, B. Meester, F. deLange, J. Schoonman, and A. Goossens, "Comparison of Cu_xS Films Grown by Atomic Layer Deposition and Chemical Vapor Deposition" *Chem. Mater.* **2005**, 17, 2724.

[10] F. Reif, "*Fundamentals of Statistical and Thermal Physics*" McGraw-Hill, **1965**.

[11] H. R. Vandenberg, C. A. Tenseldam, and P. S. Vandergulik, "Compressible Laminar Flow in a Capillary" *J. Fluid. Mech*. **1993**, 246, 1.

[12] N. F. Baril, B. Keshavarzi, J. R. Sparks, M. Krishnamurthi, I. Temnykh, P. J. A. Sazio, A. C. Peacock, A. Borhan, V. Gopalan, and J. V. Badding, "High-Pressure Chemical Deposition for Void-Free Filling of Extreme Aspect Ratio Templates" *Adv. Mater*. **2010**, 22, 4605.

[13] A. C Jones and M. L. Hitchman, "*Chemical Vapour Deposition: Precursors, Processes and Applications"* RSC Publishing, **2008**.

[14] G. B. Stringfellow, "*Organometallic Vapor-phase Epitaxy: Theory and Practice*" Academic Press, **1999**.

[15] P. J. A. Sazio, A. Amezcua-Correa, C. E. Finlayson, J. R. Hayes, T. J. Scheidemantel, N. F. Baril, B. R. Jackson, D. J. Won, F. Zhang, E. R. Margine, V. Gopalan, V. H. Crespi, and J. V. Badding, "Microstructured Optical Fibers as High-Pressure Microfluidic Reactors" *Science* **2006**, 311, 1583.

[16] J. R. Sparks, R. He, N. Healy, S. Chaudhuri, T. C. Fitzgibbons, A. C. Peacock, P. J. A. Sazio, and J. V. Badding, "Conformal Coating by High Pressure Chemical Deposition for Patterned Microwires of II-VI Semiconductors" *Adv. Funct. Mater.* **2012**, DOI: 10.1002/adfm.201202224.

[17] R. He, P. J. A. Sazio, A. C. Peacock, N. Healy, J. R. Sparks, M. Krishnamurthi, V. Gopalan, and J. V. Badding, "Integration of Gigahertz-Bandwidth Semiconductor Devices Inside Microstructured Optical Fibres" *Nature Photon*. **2012**, 6, 174.

[18] N. F. Baril, R. He, T. D. Day, J. R. Sparks, B. Keshavarzi, M. Krishnamurthi, A. Borhan, V. Gopalan, A. C. Peacock, N. Healy, P. J. A. Sazio, and J. V. Badding, "Confined High-Pressure Chemical Deposition of Hydrogenated Amorphous Silicon" *J. Am. Chem. Soc.* **2012**, 134, 19.

[19] L. Lagonigro, N. Healy, J. R. Sparks, N. F. Baril, P. J. A. Sazio, J. V. Badding, and A. C. Peacock, "Low Loss Silicon Fibers for Photonics Applications" *Appl. Phys. Lett.* **2010**, 96, 041105.

[20] B. R. Jackson, P. J. A. Sazio, and J. V. Badding, "Single-Crystal Semiconductor Wires Integrated into Microstructured Optical Fibers" *Adv. Mater.* **2008**, 20, 1135.

[21] P. J. Roberts, F. Couny, H. Sabert, B. J. Mangan, D. P. Williams, L. Farr, M. W. Mason, A. Tomlinson, T. A. Birks, J. C. Knight, and P. St. J. Russell, "Ultimate Low Loss of Hollow-Core Photonic Crystal Fibres" *Opt. Express* **2005**, 13, 236.

[22] N. Healy, L. Lagonigro, J. R. Sparks, S. Boden, P. J. A. Sazio, J. V. Badding, and A. C. Peacock, "Polycrystalline Silicon Optical Fibers with Atomically Smooth Surfaces" *Opt. Lett.* **2011**, 36, 2480.

[23] J. M. Jasinski and S. M. Gates, "Silicon Chemical Vapor Deposition One Atep at a Time: Fundamental Studies of Silicon Hydride Chemistry" *Acc. Chem. Res.* **1991**, 24, 9.

[24] C. J. Giunta, R. J. McCurdy, J. D. ChappleSokol, and R. G. Gordon, "Gas-Phase Kinetics in the Atmospheric Pressure Chemical Vapor Deposition of Silicon from Silane and Disilane" *J. Appl. Phys.* **1990**, 67, 1062.

[25] J. O. Odden, P. K. Egeberg, and A. Kjekshus, "From Monosilane to Crystalline Silicon, Part I: Decomposition of Monosilane at 690-830 K and Initial Pressures 0.1-6.6 MPa in a Free-Space Reactor" *Sol. Energ. Mater. Sol. C.* **2005**, 86, 165.

[26] J. O. Odden, P. K. Egeberg, and A. Kjekshus, "From Monosilane to Crystalline Silicon, Part II: Kinetic Considerations on Thermal Decomposition of Pressurized Monosilane" *Int. J. Chem. Kinet.* **2006**, 38, 309.

[27] J. Odden, P. Egeberg, and A. Kjekshus, "From Monosilane to Crystalline Silicon. Part III. Characterization of Amorphous, Hydrogen-Containing Silicon Products" *J. Non-Cryst. Solids.* **2005**, 251, 1317.

[28] A. Dollet, S. dePersis, and F. Teyssandier, "Rate Constants of Reactions Involving SiH_4 as an Association Product from Quantum Rice-Ramsperger-Kassel Calculations" *Phys. Chem. Chem. Phys.* **2004**, 6, 1203.

[29] C. Manfredotti, "Amorphous Silicon Prepared by Low Pressure Chemical Vapour Deposition" *Thin Solid Films* **1986**, 141, 171.

[30] H. Hemmes, A. Driessen, and R. Griessen, "Thermodynamic Properties of Hydrogen at Pressures up to 1 Mbar and Temperatures Between 100 and 1000 K" *J. Phys. C: Solid State Phys.* **2000**, 19, 3571.

[31] J. R. Thygeson and M. C. Molstad, "High Pressure Hydrogen Attack of Steel" *J. Chem. Eng. Data* **1964**, 9, 309.

[32] J. Song and W. A. Curtin, "Atomic Mechanism and Prediction of Hydrogen Embrittlement in Iron" *Nat. Mater.* **2012**, DOI: 10.1038/nmat3479.

[33] P. H. Oosthuizen and W. E. Carscallen, "*Compressible Fluid Flow*" McGraw-Hill, **1997**.

Chapter 3

HPCVD in Microstructured Templates: Silicon Optical Fibers

With the fundamental aspects of HPCVD in a single capillary understood, it is possible to fabricate unique optical fibers by carrying out the reactions in the microstructured templates shown in **Figure 1.1**. In this chapter, the materials chemistry aspects of step index silicon optical fibers in single capillaries are first discussed with the goal of realizing low optical loss in the IR. Then, the deposition is extended to MOFs, where the ability to selectively fill the pores of MOFs is demonstrated to enable tailoring of the properties of the resulting structures. These techniques are employed to fabricate two unique semiconductor optical fibers: a polycrystalline silicon (poly-Si) MOF and an hydrogenated amorphous silicon (a-Si:H) PCF.

3.1 Materials Quality of Silicon Optical Fibers

In HPCVD, silicon is typically deposited in the amorphous state in a furnace set to 500 °C with a temperature gradient along the axial direction. This amorphous material (without hydrogen passivation) has very high absorption in the infrared due to the presence of defect states in the bandgap that allow for absorption of light. By annealing the material after deposition, the amorphous network crystallizes, which in turn forms a defined bandgap with minimal defect states. Thus, the materials properties and optical loss of the silicon can be improved such that the completely filled capillaries function as low loss poly-Si optical fibers (**Section 3.1.1**). Another way to reduce the loss of the material is to incorporate hydrogen into the amorphous material to form a-Si:H to passivate the dangling bonds that create defect states, which is discussed in **Section 3.1.2**.

3.1.1 Polycrystalline Silicon

A systematic study was performed to investigate the effects of annealing on the optical loss of simple step index poly-Si optical fibers in collaboration with the University of Southampton.[1] In this case, the material was intentionally deposited with a low hydrogen content (in other words, at a high temperature). The fibers used in this investigation were fabricated by completely filling 6 μm inner diameter capillaries with silicon. Owing to the large index difference between the silicon core (n~3.5) and silica cladding (n~1.4), the guided light is well confined to the micrometer-sized core. The fibers were then polished on both facets using standard polishing techniques. A polished fiber facet is shown in **Figure 3.1**. Five silicon fibers were fabricated under different conditions: (A) amorphous silicon deposited at ~ 400 °C, (B) amorphous silicon deposited at ~ 500 °C, (C) poly-Si deposited at ~ 500 °C and annealed at 1125 °C, (D) poly-Si deposited at ~ 500 °C and annealed at 1200 °C, and (E) poly-Si deposited at ~ 500 °C and annealed at 1325 °C.

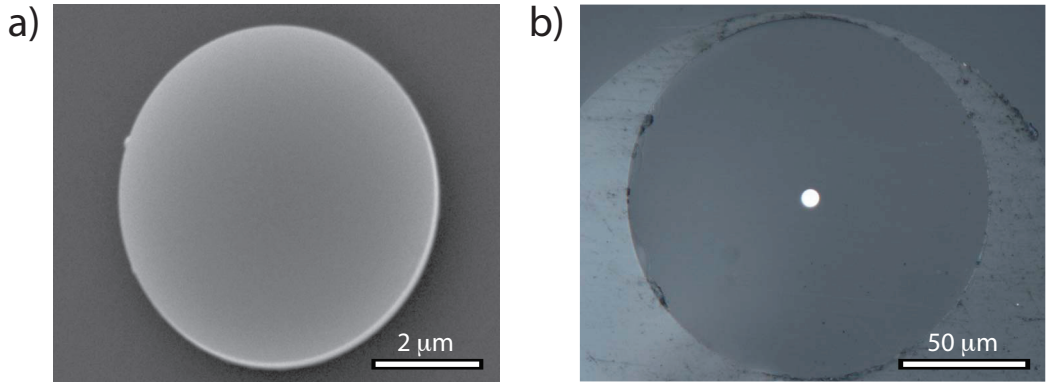

Figure 3.1: Silicon optical fibers.[1] (a) SEM image of a 6 μm diameter poly-Si optical fiber core. (b) Optical micrograph of the entire facet after polishing.

To determine the quality of the deposited material of the various fibers, micro-Raman spectroscopic measurements were performed on the silicon cores. In all cases a 633 nm HeNe laser was focused onto the silicon through the side of the transparent silica cladding, with a spot

size of ~ 2 μm and 3 mW of power at the outer surface. **Figure 3.2a** shows the Raman spectra of the two amorphous silicon fibers (samples A and B). Both fibers exhibit a strong broad peak around 480 cm^{-1} corresponding to the transverse optical mode, with some weaker subsidiary peaks associated with the other known vibrational modes of amorphous silicon.[2] In the higher frequency regime, as shown in the inset, sample A (solid line) also has a peak at ~ 2000 cm^{-1} which is the Si-H stretching mode.[3] This peak is absent in sample B (dashed line) indicating that hydrogen is incorporated into the amorphous material at low deposition temperatures.[4] The effects of hydrogen incorporation via HPCVD will be discussed in **Section 3.1.2**. However, based on this observation, only poly-Si fibers that are annealed from amorphous samples deposited at ~ 500 °C were investigated to avoid H_2 out diffusion. This is because the hydrogen reduces the density of the silicon; therefore, a high hydrogen content structure decreases in volume and peels off the silica walls when it is annealed and H_2 is evolved.

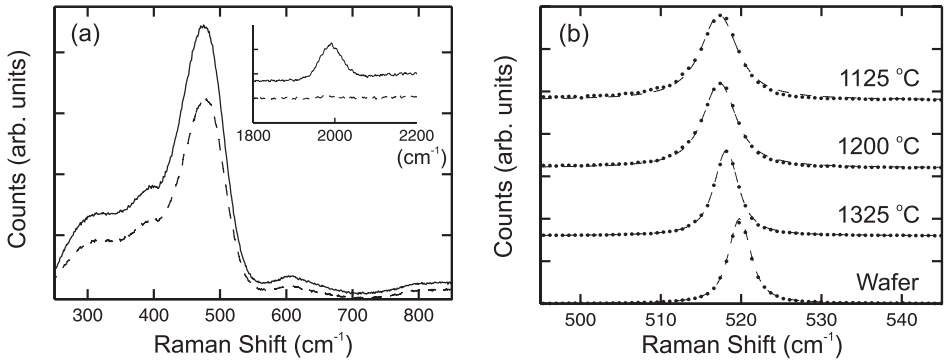

Figure 3.2: Raman spectra of silicon optical fibers in the (a) amorphous state and (b) annealed at different temperatures.[1]

The Raman spectra for the poly-Si samples are shown in **Figure 3.2b**, together with a reference spectrum taken of a single crystal silicon wafer (bottom curve). To estimate the Raman peak widths, the spectra are fitted with Voigt profiles (dashed curves) to account for the 1.5 cm^{-1} Gaussian instrument contribution. The silicon wafer has a Lorentzian full width at half maximum of 2.7 cm^{-1}, centered at 520 cm^{-1}, with the poly-Si widths measured to be 5.1 cm^{-1}, 4.5 cm^{-1}, and

3.0 cm^{-1} for samples C (1125 °C anneal), D (1200 °C anneal) and E (1325 °C anneal), respectively. The larger widths and the asymmetries seen in the poly-Si peaks, particularly for the lower temperature annealed samples, are due to contributions from defects and amorphous fractions, that surround the single crystal grains, which are associated with vibrations at frequencies in the range 500 − 517 cm^{-1}.[5] The smaller width of the Raman peak of sample E can be attributed to a reduction in the defect concentration and amorphous content and an improvement in the overall crystallinity.[6] The slight red shift of the poly-Si peaks (517 cm^{-1} for samples C and D, and 518 cm^{-1} for sample E) is, in part, due to the material surrounding the crystalline grains, as well as a small contribution from the residual stress induced across the silicon-silica boundaries which are introduced during annealing, and are a result of the differences in the thermal expansion of the strongly adhered materials.[7]

Optical transmission losses of the fibers as a function of the guided wavelength were determined using the cutback method (Laura Lagonigro and Noel Healy, University of Southampton), where the typical starting length was ~ 8 mm with 1 mm polished off the samples between each measurement. A supercontinuum source was filtered using a tunable acousto-optic device to yield an average power of ~ 0.5 mW over the wavelength range 1.2 − 1.7 μm, and launched into the silicon cores via free space coupling using a 25× microscope objective lens. A second 40× objective was used to capture the transmitted light and focus it onto a Newport 2832C power meter. The results of the loss measurements are plotted in **Figure 3.3** for all but the amorphous sample B. As discussed earlier, without hydrogen to saturate the dangling bonds, amorphous silicon has a very high loss in the infrared wavelength range (50 dB/cm at 1550 nm).

From the curves measured for the remaining samples, it is clear that in all cases the losses decrease for increasing wavelength, which suggests that scattering mechanisms (for example, from grain boundaries) contribute significantly to the loss. Further evidence is provided by the good agreement with the fitted curves which display the λ^{-4} dependence associated with Rayleigh

scattering. Comparison of the poly-Si loss curves shows that there is a clear reduction in the losses as the annealing temperature is increased, which agrees with the Raman observations that the higher temperature anneal leads to an improvement in the polycrystalline quality. From sample E, the loss at 1550 nm was determined to be ~ 8 dB/cm. Although the amorphous sample A shows a similar wavelength dependence, the slope of this data set is much steeper than the two higher temperature annealed samples, which are expected to be predominantly crystalline in nature. Thus the sharp increase in the losses at short wavelengths in the low temperature annealed sample C can be attributed to a contribution from the amorphous silicon material that surrounds the single crystal grains. Significantly, sample A yields the lowest loss of ~ 5 dB/cm at 1550 nm, which suggests that the incorporation of hydrogen, which was evident from the Raman spectrum, has resulted in an appreciable saturation of dangling bonds in the material (see **Section 3.1.2**).

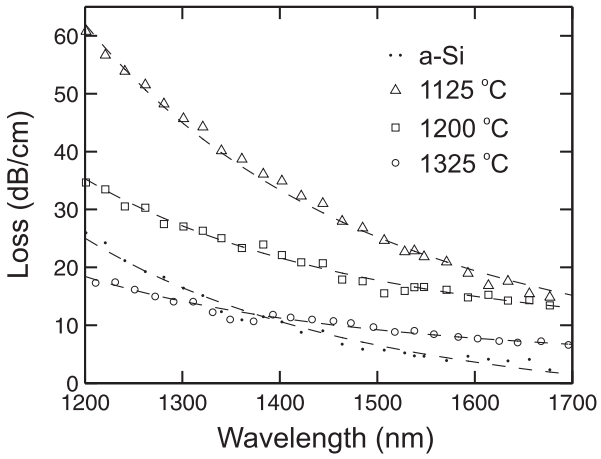

Figure 3.3: Optical loss as a function of wavelength of silicon optical fibers in the amorphous state and annealed at different temperatures.[1] Dashed lines are λ^{-4} fits.

The results of the transmission measurements indicate that by further optimizing the deposition and annealing processes to obtain high quality, low loss, and large grain poly-Si core materials, it should be possible to fabricate silicon fibers with losses that approach those of the lowest recorded values in on-chip waveguides of around a few dB/cm.[8,9] Since the main source of loss is from scattering from grain boundaries, minimizing the number of grain boundaries by

maximizing the size of the grains should minimize the loss of poly-Si optical fibers.

The resulting grain size can be controlled when annealing an initially amorphous silicon material via the anneal temperature.[10] At temperatures above about 500 °C, crystallites begin to nucleate in the amorphous phase. The number of initial crystallites is controlled by the temperature, with less nucleation sites forming at lower temperatures. As the adjacent amorphous material crystallizes around the seed, the grain grows until all the amorphous material is consumed and two crystalline grains touch each other at a newly formed grain boundary. Following the initial grain growth, a higher temperature anneal (~1000°C) can anneal out any defects within these large grains. Even higher temperatures (>1000 °C) can cause grains to combine into even larger ones. With the HPCVD process, the silica fiber can only withstand high temperatures (~1300 °C) for less than 15 minutes due to crystallization/cracking effects of the silica glass. Therefore, the high temperature annealing should start with the largest grains possible.

Accordingly, the optical fibers should be annealed at as low of a temperature as possible in order to maximize the initial grain size (i.e., form only a small amount of initial crystallites to form large grains). To determine the minimal practical temperature for crystallization of amorphous silicon, a 800 nm wire was annealed in a temperature gradient with a maximum temperature of 665 °C for 5 days. Raman spectra at 633 nm excitation were then collected along the length (as a function of temperature) to determine the minimum anneal temperature (**Figure 3.4**) necessary to grow crystallites. From this data, the threshold anneal temperature needed to form poly-Si is ~520°C; note that the material also becomes transparent to visible (red) light upon this transition.

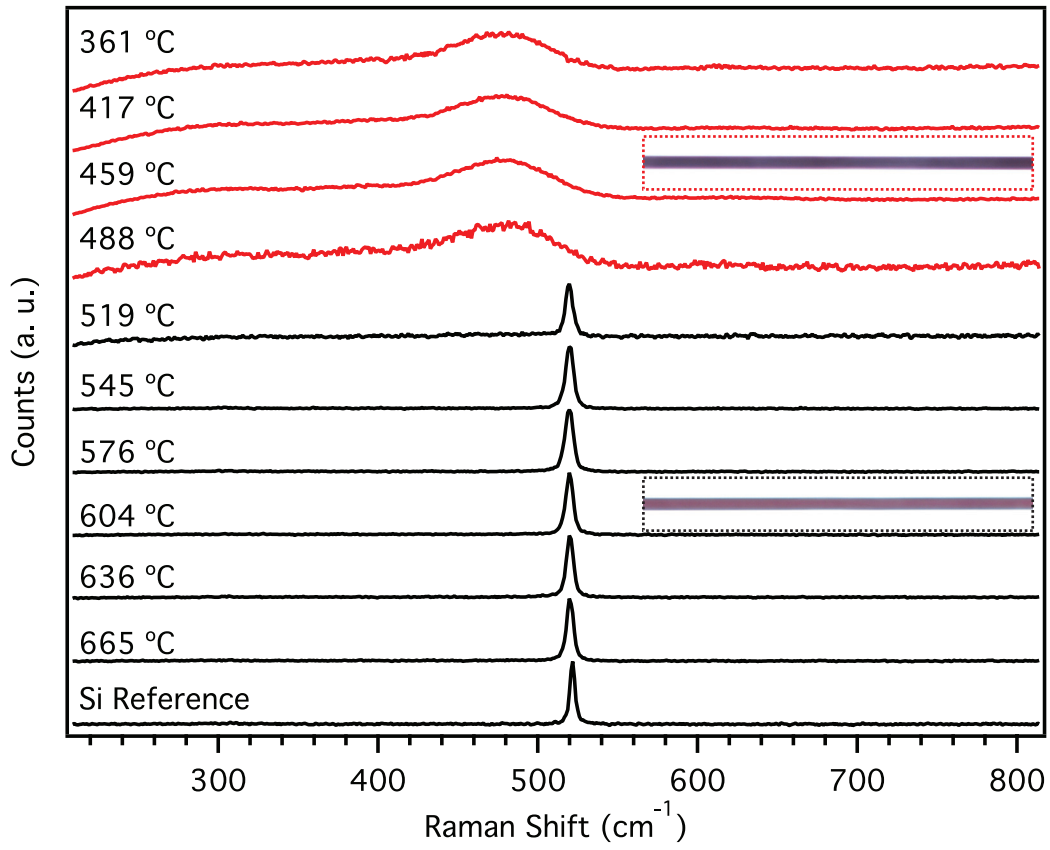

Figure 3.4: Determination of the minimum annealing temperature needed to form poly-Si from amorphous silicon. The inset images show that the material becomes transparent to red light once it is polycrystalline.

It follows that a sample which is annealed at a low temperature first before a high temperature should have a lower optical loss. In order to test the hypothesis, two samples were fabricated from an amorphous silicon wire deposited at 500 °C: (F) low temperature anneal at 530 °C for 7 days followed by a high temperature anneal at 1300 °C for 15 min, and (G) low temperature anneal at 560 °C for 7 days followed by a high temperature anneal at 1300 °C for 15 min. The losses of the samples were determined using the single pass technique at 1550 nm at different stages of the annealing. Initially, sample F had a loss of 30 dB/cm, while sample G had a loss of 16 dB/cm. After the high temperature anneal, sample F had a lower loss (9 dB/cm) than sample G (13 dB/cm). After the first anneal, sample F should have larger grains than sample G

owing to the lower temperature, but sample F will also have a higher loss than sample G due to the larger grains having more defects. However, after annealing at 1300 °C, the defects of the larger grains in F are annealed out and the primary source of loss in the waveguides is now from grain boundary scattering (**Figure 3.5**). Indeed, the losses then intersect after the high temperature anneal, and sample F results in the lower loss of the two samples.

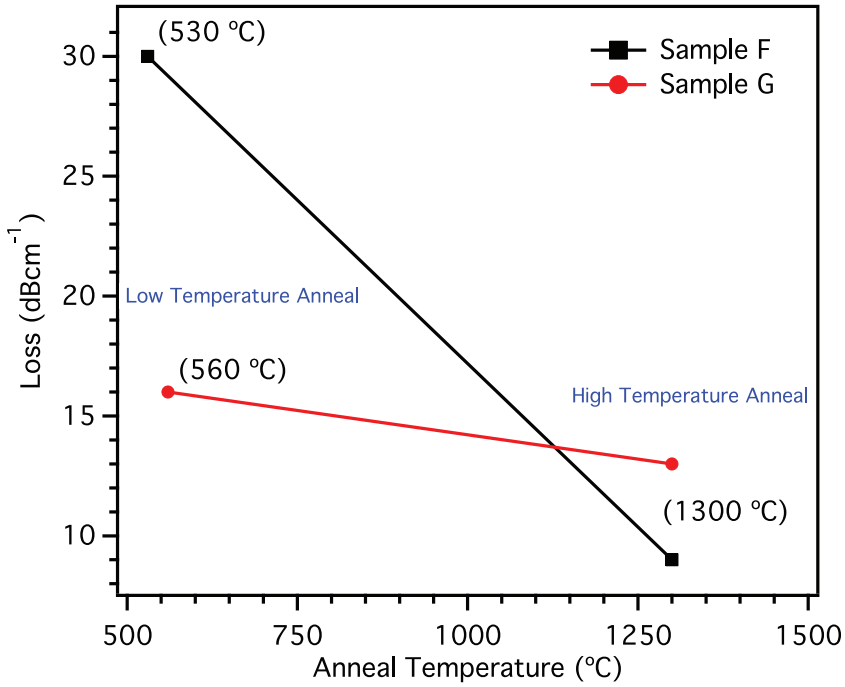

Figure 3.5: Loss of poly-Si optical fibers as a function of annealing strategy.

Further improvement of annealing strategies via thermal methods could result in a much lower loss or even single crystals if a seed point, such as a taper, is used to propagate a single crystal through the amorphous material. Some initial experiments with laser annealing are also proving to be promising in reducing grain boundary scattering in poly-Si optical fibers. Also, metal-induced crystallization is another potential route to propagating a single grain through the amorphous wire.

3.1.2 Hydrogenated Amorphous Silicon

Although amorphous silicon has very high loss (50 dB/cm at 1550 nm), the materials properties, and thus the loss, can be significantly different when hydrogen is incorporated into the material (as was seen with sample A in **Section 3.1.1**). This is because hydrogen can saturate the dangling bonds to form a-Si:H and eliminate any defect states in the bandgap that would otherwise absorb the waveguided light. As was discussed in **Chapter 2**, the high pressure chemistry in HPCVD can result in high rates of deposition at lower temperatures than are possible in conventional CVD; resulting in a significant incorporation of hydrogen by simple thermal decomposition of SiH_4. Typically, an expensive PECVD reactor is needed to achieve deposition at a low enough temperature for hydrogen incorporation in the deposited material.

In order to determine the threshold deposition temperatures for incorporation of hydrogen, a study was performed to investigate the hydrogen content as a function of deposition temperature. This was important for two reasons: (1) a low hydrogen content material is desirable for poly-Si annealing to avoid large volume changes (**Section 3.1.1**) and (2) maximizing the hydrogen content can help to minimize the loss in a-Si:H optical fibers. Raman spectra at 633 nm excitation were collected along the length of a 6 μm silicon wire that was deposited in a temperature gradient with a maximum temperature of 500 °C. The Si-H stretching mode (~2000 cm^{-1}) intensity decreases as the temperature increases (**Figure 3.6**). The cutoff for hydrogen incorporation appears to be ~465 °C (within the detection limits of this experiment). At very low temperatures (320 °C), a significant amount of hydrogen is incorporated into the material as evidenced by the appearance of the $Si\text{-}H_2$ stretching mode at 2075 cm^{-1}. Incorporation of hydrogen bound as $Si\text{-}H_2$ may not be ideal for waveguide applications as it can form small voids that can scatter light. Further optimization of the hydrogen content by Todd D. Day of the Badding group has resulted in a significant reduction in losses as well as the ability to control the

hydrogen content with the carrier gas to produce single mode a-Si:H optical fibers.[11,12] In fact, a-Si:H optical fibers are the lowest loss silicon waveguides that have been fabricated by HPCVD, with a loss of 0.8 dB/cm at 1550 nm.

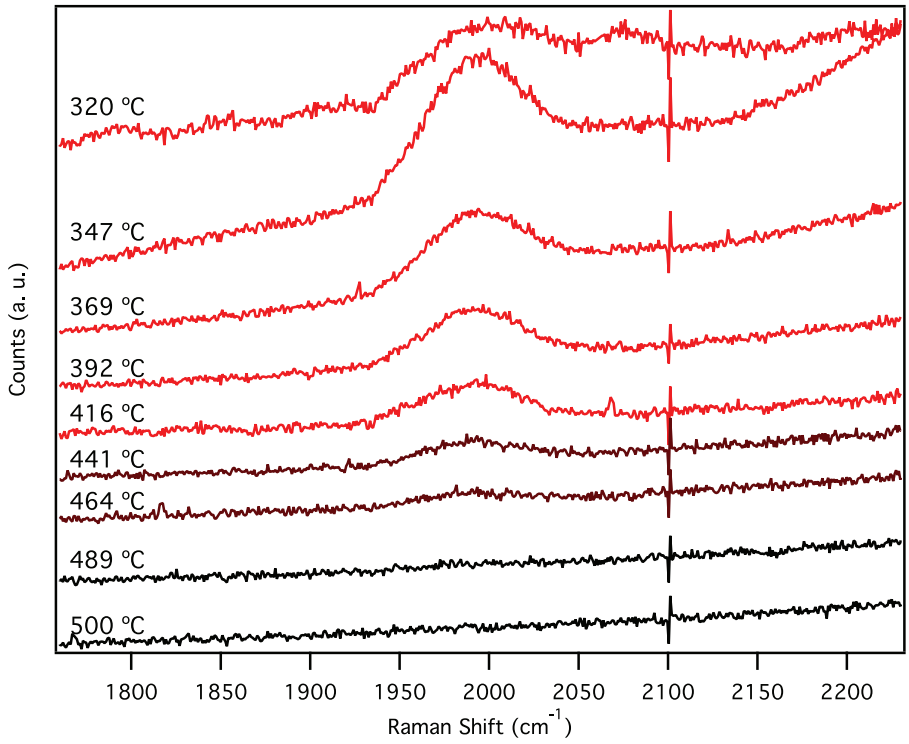

Figure 3.6: Intensity of the Si-H stretching mode in Raman spectroscopy of a-Si:H as a function of deposition temperature.

3.2 Selective Filling of MOFs with Semiconductors

Control of the transverse patterning in MOFs allows for precise tailoring of the transmission properties of the guided modes. By simply tuning the hole size and spacing of the capillaries that run along the length of a MOF, it is possible to tune the dispersion, nonlinearity, as well as induce birefringence and endlessly single mode operation.[13] As is the theme of this dissertation, MOFs also make exceptional templates for the infiltration of drawing-incompatible materials into the capillaries to fabricate complex, precisely organized micro to nanoscale

structures with additional functionality. To date, MOFs have been filled with a variety of materials including liquids,[14] gases,[15] metals,[16] monolayers,[17] and semiconductors,[18] leading to the development of active devices such as optical switches,[14] tunable filters,[19] and modulators.[20] An extension to this filling approach that allows for even more geometrical design flexibility is to control the filling or coating of selected holes in the MOF template. By engineering the guided mode interaction with the infiltrated material, selectively filled MOFs can exhibit unique transmission properties and have been demonstrated for use as optical thermometers,[21] polarizers,[22] and sensors.[23]

The selective filling of MOFs has been demonstrated previously via a number of methods, including the collapsing of selected air holes,[21,24] injection-cleave techniques that exploit the dependence of the capillary forces on the hole size,[25] carving holes in the side of the MOFs,[23,26] dispensing epoxy into the MOF holes using a micro-tipped silica fiber,[27] and end-face photolithography.[28] Of these techniques, the latter two allow for arbitrary patterns to be made independent of relative hole size and spacing. However, these methods require either rigorous mechanical control of a dispensing tip or a time consuming photolithographic process that decreases the damage threshold of the MOF end face.

In this section, a new selective filling technique that allows for complex two-dimensional patterning, independent of the MOF pore size and spacing is described, which is compatible with the HPCVD procedure. The technique is based on the selective waveguide curing of an epoxy with a refractive index greater than silica that has been infiltrated into the MOF holes. By waveguiding UV light in the epoxy filled holes it is possible to cure complex patterns in a quick and convenient manner. To demonstrate the flexibility of this technique, a variety of MOF templates have been selectively filled and coated with different semiconductor materials. Importantly, the selective filling of MOF templates with solid materials such as semiconductors via deposition offers several advantages over the liquid filling approaches as it is possible to

deposit a range of coating thicknesses from thin films to solid inclusions, different holes can be filled with different materials, and it is also possible to deposit different materials into the same hole. The ability to pattern semiconductor filled MOFs is an important step towards developing arrays of both passive and active fiber-integrated optoelectronic devices.

3.2.1 Selective Filling via Epoxy Waveguide Curing

To achieve selective filling, a UV curable epoxy, which is easily infiltrated into the holes of the MOF templates via capillary forces, is employed. A common optical grade epoxy, Norland optical adhesive 61, is ideal for this approach as it adheres strongly to silica and can withstand the pressures employed in HPCVD once it is cured. As a liquid, the epoxy has a refractive index of 1.53 and has a maximum absorption for curing at 364 nm. The cured solid has an even higher refractive index of 1.56 and transmits 364 nm light so that the solidifying material can continue to guide light down the length of the capillary to cure the epoxy at the solid/liquid interface. Thus it is possible to treat each hole as an individual step-index waveguide in which long lengths of epoxy can be cured. The ultimate resolution of this method is only limited to the spot size of the focused 364 nm light, which is shorter than the wavelengths used for two photon polymerization techniques,[28] and the focused spot is easier to control than the micro-tipped silica fiber used to manually dispense the epoxy into the holes.[27]

To ensure efficient coupling to each individually selected epoxy filled hole, the numerical aperture (NA) of the input objective must be less than that of the epoxy waveguide (NA=0.48). If the NA is higher than that of the waveguide, the light launched into the cladding can cure adjacent holes in the array. In addition, launching light into liquid cores is known to be problematic as the liquid can move away from the surface of the cleaved facet. As a result, if the epoxy is not in the plane of the cleaved fiber, this can also lead to the neighboring holes being

cured. To ensure that the relatively low viscosity (300 – 450 cps) epoxy stays flush with the MOF end face, the opposite end is sealed with a fusion splicer so that equilibrium can be reached between the pressure build up and the capillary force. With both of these factors considered, coupling of the 364 nm line of an Argon ion laser to the epoxy waveguides is straightforward and nearly any pattern can be made in short periods of time. The selective filling process is outlined in **Figure 3.7**, where the first step is to fill all the MOF holes with a short length of epoxy. The epoxy is then cured in the holes that will eventually be filled by HPCVD. The remaining holes are then filled further before they are also cured. Finally the end of the fiber is cleaved to remove the short length of patterned epoxy to reveal the desired template for filling.

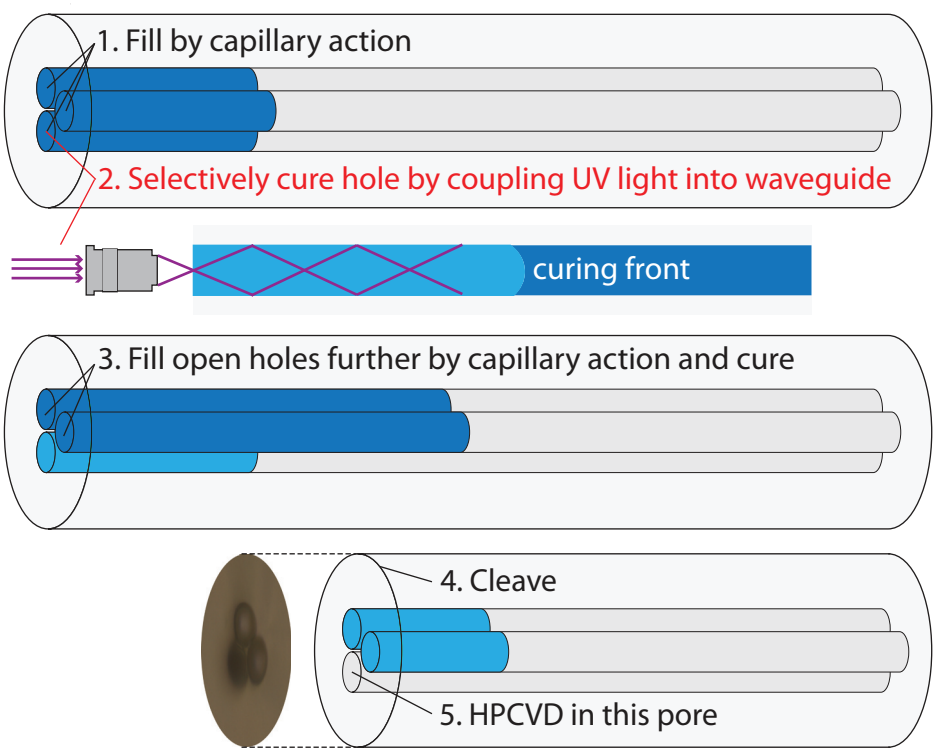

Figure 3.7: Selective filling technique.[29] Selective blockage of holes in MOFs is achieved by first filling each hole with a UV-curable epoxy (1), followed by curing a pattern of holes by treating each capillary as an individual step index waveguide (2). With the desired pattern cured, the negative is taken by filling the open holes further and curing the entire array (3). Cleaving beyond the original waveguide curing distance (4) results in a fiber facet (inset) that has the desired pattern of holes open for the HPCVD process (5).

To verify that the epoxy waveguides transmit UV light over appreciable distances, the length of cured epoxy was measured with different curing times and power densities, as shown in **Figure 3.8**. From these results, it can be seen that the cured distance tends to saturate with increasing time due to the optical loss of the epoxy waveguide, though lengths of up to 5 mm can be cured at a power density of 20 W/cm^2 in approximately 30 s. However, such long transmission lengths turn out to be detrimental to the patterning process as light can scatter into the adjacent holes as it travels down the lossy waveguides. A curing time of 5 s at a low power density of 0.14 W/cm^2 is the optimal configuration to reduce both the defects due to the scattered light and the time needed to cure complex patterns, yet is sufficient to cure lengths of ~1 mm.

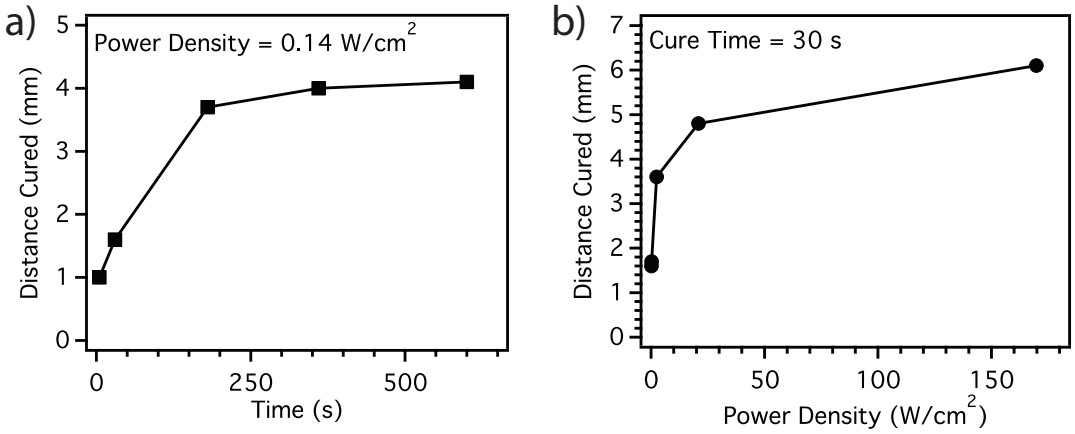

Figure 3.8: Waveguide epoxy curing.[29] The length of epoxy that is cured at different times (a, 0.14 W/cm^2 power density) as well as different power densities (b, 30 s cure times) tends to saturate due to the optical loss of the epoxy waveguides at the curing wavelengths.

3.2.2 Selectively Filled Semiconductor MOFs

To demonstrate the flexibility of this technique, semiconductor filling patterns were fabricated in a variety of MOF templates, as illustrated in **Figure 3.9**. In this figure, all of the fibers have been filled with silicon from SiH_4 pyrolysis using the HPCVD technique. By modifying the deposition parameters such as the precursor concentration, pressure and

temperature it is possible to fill a range of hole sizes, ~5 μm in **Figure 3.9a**, ~1 μm in **Figure 3.9b** and ~8 μm in **Figure 3.9c**, either to completely fill as is **Figure 3.9b**, or partially fill so that the holes are coated in thin layers such as in **Figure 3.9d**. By controlling the thickness of the deposited layers, it is possible to tune the resonance conditions of the MOFs to offer a further degree of control over the guidance properties.[30] It is also clear from **Figure 3.9a**, where the hole separation is only a few tens of nanometers, that this waveguide curing technique is suitable for any practical hole spacing; further evidence for which is provided by **Figure 3.9b** where six ~1 μm holes, separated by less than 1 μm, have been cured around a single hole. The examples of complex patterning in the form of concentric rings, **Figure 3.9c**, and the initials "PSU", **Figure 3.9d**, highlight the versatility of this technique.

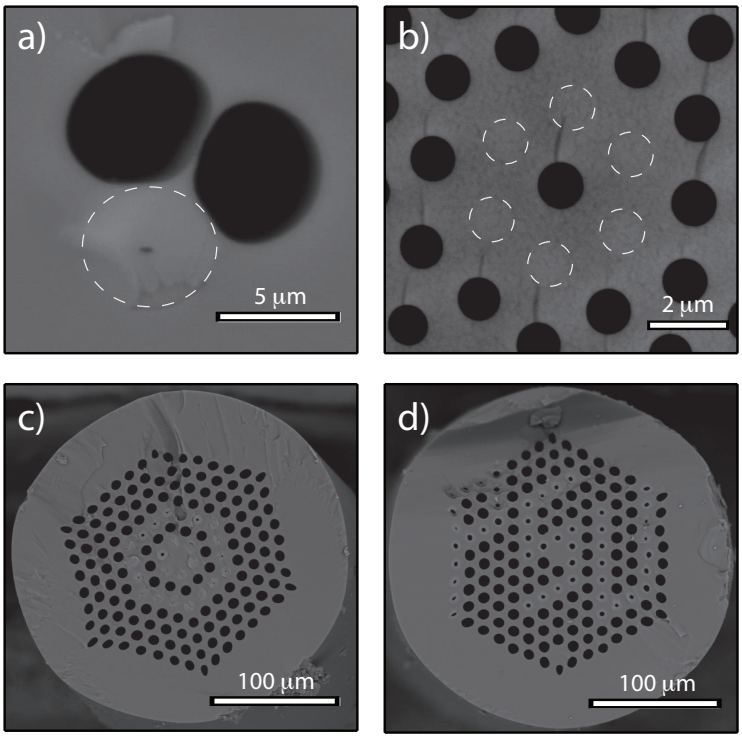

Figure 3.9: Selectively filled microstructured optical fibers.[29] Following epoxy waveguide curing, HPCVD can be carried out in specific capillaries of a variety of MOFs. Holes with separation < 100 nm (a) and small, closely spaced holes (b) can be cured without cross-talk and subsequently have silicon deposited in the holes that are left open. The technique allows for any pattern to be fabricated, such as concentric rings (c) and the letters "PSU" (d).

As previously discussed, an advantage of selectively filling with solid materials such as semiconductors is that it is possible to deposit multiple materials within the same template. To deposit two materials, each within different holes of the MOF, first the template is patterned then the open holes are completely filled with silicon. The patterned facet is then cleaved to open the originally blocked holes for HPCVD of another material, where in this case germanium is deposited from GeH_4.[31] **Figure 3.10a** shows a Raman spectroscopy map of a polished facet of the multi-material filled MOF. Confirmation of the different crystalline materials is provided by the Raman spectra in **Figure 3.10c** showing the silicon peak at 520 cm^{-1} and the germanium peak at 300 cm^{-1}. In addition, it is also possible to deposit different materials in the same hole to fabricate heterostructures, as shown in **Figure 3.10b**. Here, germanium has been deposited on a layer of silicon, though it is also possible to deposit several layers of doped materials for the fabrication of junction devices.[32,33] Thus using this method it should be possible to deposit semiconductor junctions into selected holes of the MOF templates to fabricate arrays of active devices. Selectively filling the pores of MOFs allows for their light guiding properties to be tuned, which will be demonstrated in **Section 3.4**.

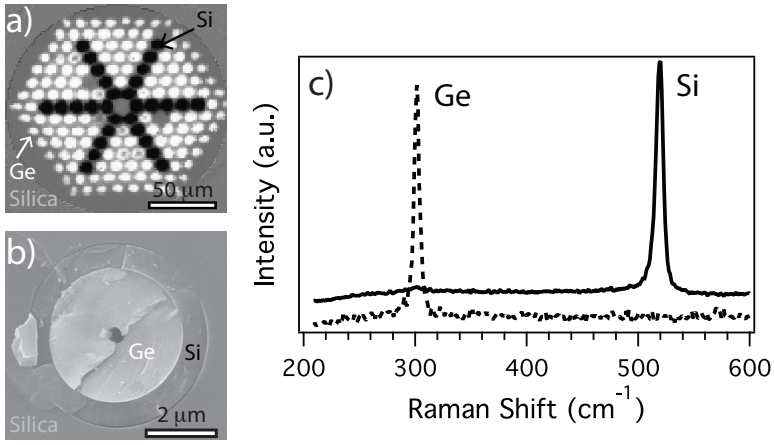

Figure 3.10: Multimaterial microstructured optical fibers.[29] Multiple crystalline semiconductors can be patterned in the transverse plane and layered by sequential deposition. (a) Raman mapping of the fiber facet shows a pattern of silicon (black) and germanium (white) rods in a MOF. (b) A SEM image of a germanium layer deposited on top of a silicon layer. Raman spectra of crystalline silicon and germanium are shown in (c).

3.3 Large Mode Area Silicon Optical Fibers

This work was performed in collaboration with Noel Healy at the University of Southampton, UK.[34] Modified figures and sections from reference [34] are reproduced with permission.

3.3.1 Motivation and Design

The burgeoning field of silicon photonics owes much of its success to the ability to leverage a vast, highly developed and capitalized microelectronics industry that allows for deep submicrometer lithographic processes at a wafer scale.[35] Typical on-chip silicon photonic devices are constructed by defining waveguiding structures on silicon-on-insulator wafers that were originally developed to minimize the parasitic capacitance of high speed electronic devices such as heterojunction bipolar transistors. Recently, there has been increased interest in tailoring the waveguide design to optimize these devices for photonics applications.[36] Since the high core/cladding index contrast results in strong optical confinement, so that waveguides of microscale dimensions are highly multimoded, attentions have primarily focused on scaling down the core to nanometer dimensions.[37] Such scaling not only reduces the number of guided modes supported by the core, thus reducing mode competition, but also increases the field intensities. However, this approach limits the optical power that can be launched into these structures before damage thresholds are reached, as well as significantly reducing the coupling efficiency between devices, particularly if light is launched by an optical fiber owing to the mismatch in mode cross-sections (a single mode fiber has a core diameter of 8 μm). Furthermore, small core structures force more light into the cladding, which increases losses due to surface roughness at the core-cladding interface and inhibits the use of these waveguides at wavelengths greater than 2 μm,

where the optical losses in the silica cladding are large. Therefore, there exists a need to fabricate large core, low NA silicon waveguides that can couple effectively to standard silica optical fibers. The design freedom of MOF templates allows for this challenge to be met in a way that would be very difficult to realize with planar fabrication methods.

3.3.2 Fabrication

A large mode area (LMA) silicon optical fiber was fabricated by filling in the holes of a 3-cell defect PCF with silicon by HPCVD (**Figure 3.11**).[34] The resulting silicon MOF has a comparatively large core of several micrometers in diameter, but a very small core-cladding effective index difference so that it supports significantly fewer guided modes than an equivalently sized conventional silicon-silica structure. Therefore, LMA silicon fibers offer improved coupling with standard micrometer-sized single mode silica fibers compared to on-chip waveguide devices, which has previously been seen as one of the major bottlenecks to silicon photonic device technology. The ability to realize LMA structures that are not highly multimode has a number of additional advantages for practical device applications. For example, LMA fibers exhibit low nonlinearities, low confinement losses, can have guidance properties that are largely wavelength independent, and can tolerate very high power levels.

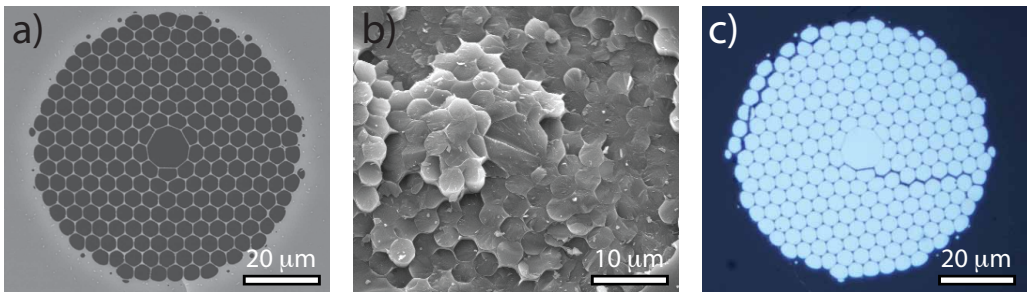

Figure 3.11: Large mode area silicon optical fiber.[34] (a) SEM of the silica MOF template (b) SEM of the silicon filled MOF (c) Optical micrograph of the polished optical fiber.

3.3.3 Characterization

Characterization of the optical transmission properties of a 6 mm length of poly-Si LMA fiber, annealed at 1125 °C, was conducted using a supercontinuum source over the extended telecommunication wavelength range of 1.3 − 1.7 μm in the same way as **Section 3.1.1** (Noel Healy, University of Southampton). **Figure 3.12** shows the near field mode images for light at (a) 1.3 μm, (b) 1.55 μm and (c) 1.7 μm, where at each wavelength the two allowed modes can clearly be distinguished. Importantly, coupling is preferentially obtained into the fundamental mode, with the second order mode only being isolated when the input beam is launched off-axis to the core. The asymmetries seen in the mode profiles at the shorter wavelengths are most likely due to mixing between the allowed modes, though this may also be due in part to the asymmetry in the microstructured template. At 1.7 μm, the second order mode is more difficult to excite resulting in a higher purity fundamental mode. Note that the isolated node on the left hand side in **Figure 3.12(c - right)** is a silicon cladding rod mode, coupling into which is hard to avoid owing to the off-axis launch.

The middle column of **Figure 3.12** plots the normalized cross-section of the fundamental modes (dotted curves) showing good agreement with their Gaussian fits (dashed lines). From the full width at half maximum values at the $1/e^2$ power level, the effective mode areas are calculated to be 21 μm^2, 26 μm^2, and 26 μm^2, top to bottom, which match well with the ~ 27 μm^2 predicted from finite element modeling for all the fundamental modes over this wavelength range. This mode area is thus comparable with the effective area of the fundamental mode of a single mode fiber (~70 μm^2), which is in contrast to those of on-chip devices, typically of nanometer dimensions, that are at least an order of magnitude smaller.[37] Optical transmission losses as a function of the guided wavelength were then determined using a cut-back method, where 1 mm lengths were polished off the sample between each measurement. As was shown in **Section 3.1.1**,

the optical loss of this fiber decreases with increasing wavelength with a λ^{-4} dependence; primarily due to Rayleigh scattering in the polycrystalline material.

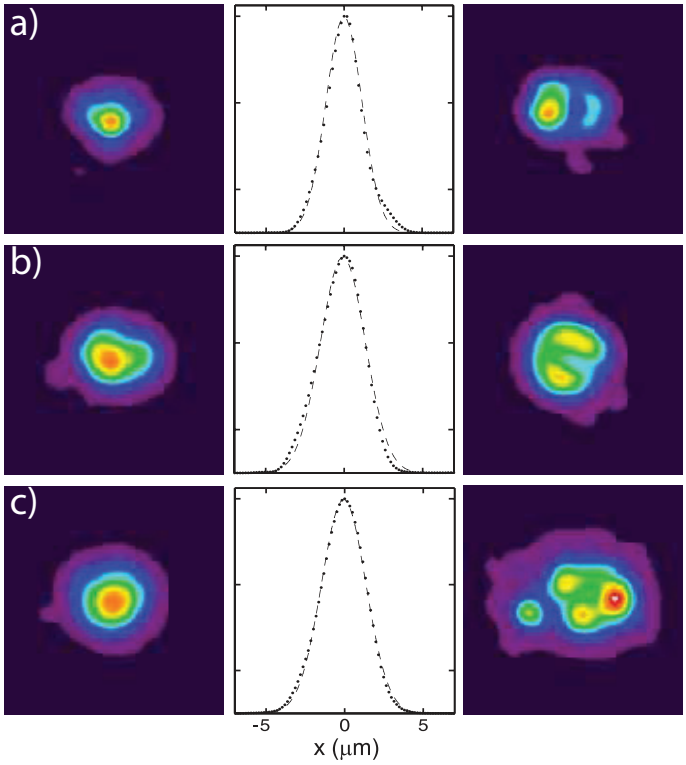

Figure 3.12: Dual mode guidance in a silicon large mode area optical fiber.[34] Intensity profiles of the fundamental (left column) and second order (right column) modes excited at the input wavelengths: (a) 1.3 μm, (b) 1.55 μm and (c) 1.7 μm. The middle column plots the normalized cross-sections (dotted lines) together with their Gaussian fits (dashed lines) of the fundamental mode.

This structure was determined to be dual mode over a very wide wavelength range from the near to mid-infrared with losses that depend only on the material quality. The properties of this novel silicon filled MOF render it suitable for high energy and/or multiwavelength devices with applications including mid infrared Raman amplification,[38] imaging,[39] and broadband supercontinuum generation.[40] The efficiency with which these silicon microstructured fibers can be launched into and integrated with existing fiber infrastructures will open up new possibilities for the next generation of silicon photonics devices.

3.4 Anti-Resonant Reflecting Silicon Optical Fibers

This work was performed in collaboration with Noel Healy at the University of Southampton, UK.[41] Modified figures and sections from reference [41] are reproduced with permission.

3.4.1 Motivation

Since the first demonstration of the PCF in 1996,[42] there have been hundreds of experimental and theoretical iterations that exploit its unique properties for applications ranging from non-linear optics,[43] fiber lasers,[44] and sensing.[45] The versatility of the PCF is predominantly due to its 2D transverse microstructure, which includes a cladding that consists of a background material and a lattice of periodic inclusions. The PCF can be classed into two distinct groups, those that guide through the mechanism of total internal reflection and those that guide through resonant effects associated with the microstructured cladding. The former guidance mechanism is analogous to the conventional step index fiber, in which the core has a higher refractive index than the cladding, so that either the cladding inclusions or the background material must have a lower refractive index than the core.[42] In general, the second class of fiber has cladding inclusions that are of equal or higher refractive index than that of the core. If the inclusions have a refractive index that is equal to that of the core or they are strongly coupled (i.e. the inclusion-background refractive index contrast is low), then the fiber is well described by the photonic bandgap (PBG) model. This model considers the guidance mechanism as a series of Bragg reflections induced by the periodic refractive index of the cladding.[46] When the Bragg condition is satisfied, light is forbidden to propagate through the cladding and is confined to the core. Due to the resonant nature of the Bragg condition, the transmission spectrum of a PBG

guiding optical fiber consists of core guided bands that are approximately periodic with wavelength. A well satisfied Bragg condition is required for this fiber type and the transmission properties are very sensitive to variations in the microstructure's periodicity.

When the cladding inclusions have a relatively high refractive index, compared to that of the background material, the inclusions are effectively isolated and the antiresonant reflecting optical waveguide (ARROW) model is more appropriate to describe the PCF.[47] This model considers that a single dielectric cladding inclusion can support its own guided modes. These modes, or resonances, then determine the width and position of the PCF's transmission bands. If light impinging on the inclusion is on resonance with one of its modes then it can propagate through the cladding and escape from the waveguide. Conversely, if the light is off resonance, it is reflected back into the core where it is confined and guided. Litchinister *et al*. demonstrated that for modes of a cylindrical inclusion, a suitable approximation of the resonant and antiresonant wavelengths is given by:[48]

$$\lambda_m \approx \frac{2d\sqrt{(n_{inc}^2 - n_{bg}^2)}}{m + \sigma} \qquad \textbf{(Equation 3.1)}$$

where λ_m is the wavelength, d is the inclusion diameter, m is a positive integer, n_{inc} and n_{bg} are the refractive indices of the inclusion and the background material, respectively. When $\sigma = 1/2$, λ is resonant and no core mode is supported and when $\sigma = 0$, λ is antiresonant and light is guided by the core. Thus the position and width of the transmission bands for an ARROW fiber are strongly dependent on the refractive index of the cylindrical inclusions. ARROW fibers are exciting candidates for many applications and, indeed, a number of devices have been demonstrated by using various high index cladding inclusions, for example fiber lasers, tunable transmission filters,[14] and optical modulators.[20]

3.4.2 Fabrication

The Si-ARROW fiber was fabricated by depositing a-Si:H into the capillary holes of a MOF template consisting of an array of 1 μm holes using the HPCVD technique.[41] The benefit of depositing the material in a-Si:H form is two-fold. Firstly, hydrogenation can saturate the dangling bonds of the amorphous material, thus reducing absorption losses, as was shown in **Section 3.1.2**. Secondly, depositing the material in an amorphous state allows the interfacial film of silicon to assume the smooth surface of the silica walls (root mean square (RMS) roughness of less than 0.1 nm) to reduce scattering losses incurred via reflections off the inclusions. **Figure 3.13a** shows an optical micrograph of the resulting fiber's endface after being polished using standard polishing techniques, which confirms that all holes have been completely filled.

In order to test the role of optical confinement on loss, a hybrid Si-ARROW fiber was fabricated by selectively filling the MOF template with the semiconductor material. Prior to deposition, the inner holes were plugged with UV curing epoxy to prevent infiltration of the semiconductor with the method described in **Section 3.2**. a-Si:H was then deposited into the unplugged holes. A SEM image of the hybrid Si-ARROW fiber is shown in **Figure 3.14c**, which confirms both the exclusion of any material in the inner ring of holes and the complete filling of the outer holes with the semiconductor.

3.4.3 Characterization

In order to test the optical transmission properties of the Si-ARROW fiber, characterization was conducted using a supercontinuum source over the extended telecommunication wavelength range of 1.3 – 1.7 μm in the same way as **Section 3.1.1** (Noel Healy, University of Southampton). The core guided light was filtered from the cladding light

using a pin hole, which is particularly important when measuring ARROW fibers as the cylindrical inclusions can act as isolated waveguides. The input and core guided powers were recorded for each wavelength to define the transmission spectrum shown as the solid black curve in **Figure 3.13b**. This spectrum exhibits two distinct transmission bands centered at 1365 nm and 1570 nm that match well with the finite element modeling, indicated by the dashed red curve. The central band spanning from 1430 – 1530 nm did not support a core mode, in accordance with the resonance predicted by Equation 1 at 1450 nm, and this is confirmed by the throughput images inset in **Figure 3.13**. Compared to the simulations, there is a slight reduction in the widths of the measured transmission bands, which is likely to be due to variations in the indices of the inclusions. The ability to withstand such variations is an important consequence of the ARROW mechanism as PBG fibers can suffer a total loss of guidance when their periodicity is disrupted. The extreme refractive index contrast between a-Si:H and silica means that the inclusions are well isolated, with the result being that the widths of the transmission bands are determined by the summation of the resonances of each individual inclusion. Therefore, variations in these resonances manifest themselves as a narrowing of the transmission bands rather that a complete breakdown of the fiber's guidance mechanism,[49] thus increasing the tolerance of these fibers to fabrication imperfections. The near field image of the guided mode for an operating wavelength of 1570 nm is shown in **Figure 3.13c**. The profile of the mode is approximately Gaussian with a mode field diameter of 2.8 μm, which compares well with the 3.1 μm predicted by the simulations. To determine the transmission losses at the maxima of the Si-ARROW transmission bands, cut-back measurements were undertaken and the losses for the 1365 nm and the 1570 nm bands were calculated to be 35 dB/cm and 31 dB/cm, respectively. Comparing these values with the confinement losses estimated from the simulations, where the lowest predicted value was ~ 25 dB/cm, it is likely that this is the dominant loss mechanism of the Si-ARROW fiber. However, it is clear from the discrepancy in these results that there is a further contribution to the losses,

which can be attributed to the material loss of the silicon inclusions. Evidence for this is provided by the mode profile in **Figure 3.13c** where it can be seen that, due to the small core size, there is some interaction of the light with the internal ring of silicon rods.

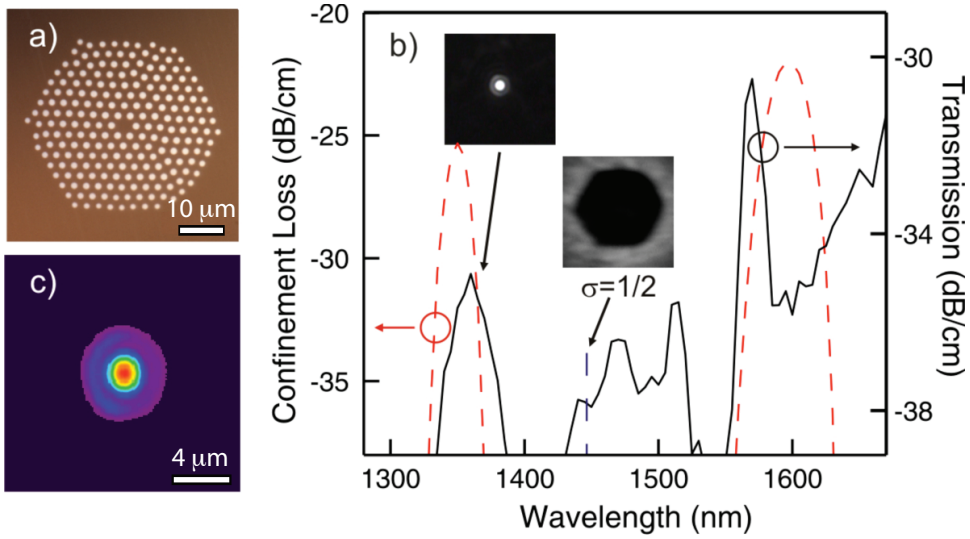

Figure 3.13: Characterization of a silicon ARROW optical fiber.[41] (a) The polished endface of the Si-ARROW fiber. (b) Measured transmission spectrum (solid black) compared to the simulations (dashed red). Insets are the output images at an antiresonant condition (core guided) and at a resonant condition. (c) Near field image of the fundamental mode at 1570 nm.

The hybrid Si-ARROW fiber was characterized in a similar manner to the Si-ARROW fiber but a longer 20 mm sample was used owing to the lower predicted confinement losses. The measured transmission spectrum of the fiber is plotted as the solid black curve in **Figure 3.14a**, showing good qualitative agreement with the simulations. The measured near field mode image, shown at 1310 nm in **Figure 3.14b**, also has a slightly reduced mode field diameter of 2.7 μm. Cut-back measurements were used to determine the transmission losses with the lowest value being 4 dB/cm at 1310 nm, which is almost three orders of magnitude lower than that measured in the Si-ARROW fiber at 1365 nm. Interestingly, this loss value is also more than an order of magnitude lower than that measured in a step index fiber with a a-Si:H core at the same wavelength (**Figure 3.3**), which is confirmation of the advantage of decoupling the

semiconductor functionality from the core. As in the Si-ARROW fiber, the non-negligible measured losses can be attributed to scattering associated with the a-Si:H material and this is supported by the wavelength dependence of the loss which was higher for the shorter wavelength transmission bands (10 dB/cm at 1040 nm). Finally, preliminary experiments have also shown that this fiber can support modes at wavelengths that have a photon energy greater than the a-Si:H valence-conduction bandgap (1.7 eV). This is illustrated in **Figure 3.14e**, which shows guidance at 620 nm (photon energy of 2 eV), and opens up the potential for silicon fiber devices to find use over an even broader wavelength range.

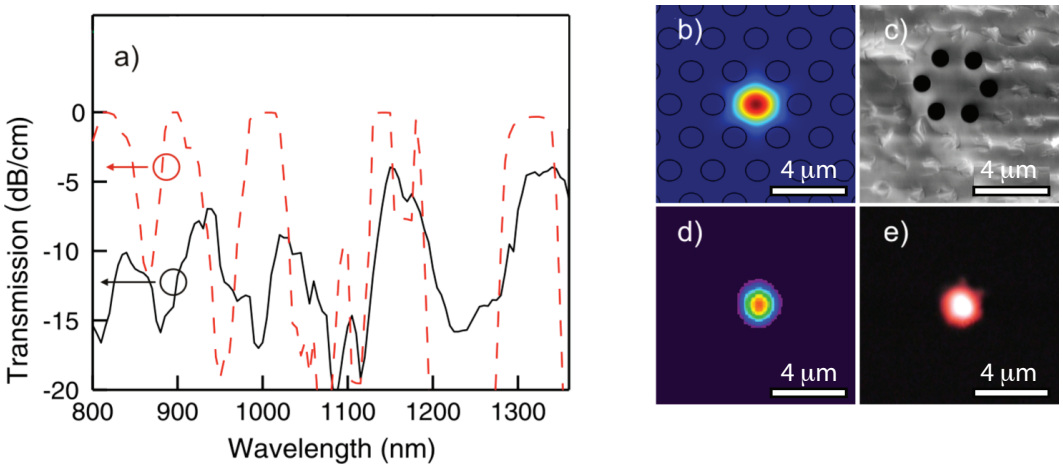

Figure 3.14: Characterization of a silicon hybrid ARROW optical fiber.[41] (a) Measured (solid black) and simulated (dashed red) transmission spectra of the hybrid Si-ARROW fiber. (b) The Poynting vector of the mode at 1310 nm. (c) SEM image of the fabricated fiber. (d) The near field mode image at 1310 nm. (e) Micrograph showing a guided mode at 620 nm where the photon energy is greater than the bandgap energy of a-Si:H.

3.5 Adding More Materials, Complexity, and Function

As was shown in this chapter, the ability to deposit semiconductors within the pores of MOFs adds new function to the optical fiber geometry. Increasing complexity with regulated impurity doping in unary semiconductors and metals allows for junction formation to enable transistor, light-emitting diode, laser, and high speed photodetector functionality. Fibers that have

such devices built into them can exhibit high performance electronic function and represent a significant step towards all-fiber optoelectronics. For high speed photodetection, poly-Si/Pt Schottky photodiodes with -3 dB bandwidths of up to 3 GHz at telecommunications wavelengths have been realized in fiber pores by means of HPCVD.[32] Homostructures such as poly-Si *p-i-n* junctions typically have higher quantum efficiency than Schottky junctions, which is desirable for photovoltaic and photodetector applications. A 1 cm long section of such a *p-i-n* fiber electrically contacted on both ends showed substantial photoresponse and an overall conversion efficiency of 0.5% under Air Mass 1.5 solar illumination.[33] Improvement of the junction geometries should allow for higher efficiencies and higher speeds. However, in order to add even more functionality, HPCVD reactions for compound semiconductors need to be developed, which is the focus of the following three chapters.

3.6 References

[1] L. Lagonigro, N. Healy, J. R. Sparks, N. F. Baril, P. J. A. Sazio, J. V. Badding, and A. C. Peacock, "Low Loss Silicon Fibers for Photonics Applications" *Appl. Phys. Lett.* **2010**, 96, 041105.

[2] D. J. Won, M. O. Ramirez, H. Kang, V. Gopalan, N. F. Baril, J. Calkins, J. V. Badding, and P. J. A. Sazio, "All-Optical Modulation of Laser Light in Amorphous Silicon-Filled Microstructured Optical Fibers" *Appl. Phys. Lett.* **2007**, 91, 161112.

[3] M. H. Brodsky, M. Cardona, and J. J. Cuomo, "Infrared and Raman Spectra of the Silicon-Hydrogen Bonds in Amorphous Silicon Prepared by Glow Discharge and Sputtering" *Phys. Rev. B.* **1977**, 16, 3556.

[4] R. Sun, K. McComber, J. Cheng, D. K. Sparacin, M. Beals, J. Michel, and L. C. Kimerling, "Transparent Amorphous Silicon Channel Waveguides with Silicon Nitride Intercladding Layer" *Appl. Phys. Lett.* **2009**, 94, 141108.

[5] A. A. Parr, D. J. Gardiner, R. T. Carline, D. O. King, and G. M. Williams, "Structural Variations in Polysilicon, Associated with Deposition Temperature and Degree of Anneal" *J. Mater. Sci.* **2001**, 36, 207

[6] L. Liao, D. R. Lim, A. M. Agarwal, X. Duan, K. K. Lee, and L. C. Kimerling, "Optical Transmission Losses in Polycrystalline Silicon Strip Waveguides: Effects of Waveguide Dimensions, Thermal Treatment, Hydrogen Passivation, and Wavelength" *J. Electron. Mater.* **2000**, 29, 1380.

[7] C. E. Finlayson, A. Amezcua-Correa, P. J. A. Sazio, N. F. Baril, and J. V. Badding, "Electrical and Raman Characterization of Silicon and Germanium-Filled Microstructured Optical Fibers" *Appl. Phys. Lett.* **2007**, 90, 132110.

[8] G. Cocorullo, F. G. D. Corte, R. De Rosa, I. Rendina, A. Rubino, E. Terzini, "Amorphous Silicon-Based Guided-Wave Passive and Active Devices for Silicon Integrated Optoelectronics" *J. Sel. Top. Quant. Electron.* **1998**, 4, 997.

[9] Q. Fang, J. F. Song, S. H. Tao, M. B. Yu, G. Q. Lo, and D. L. Kwong, "Low Loss (~6.45dB/cm) Sub-Micron Polycrystalline Silicon Waveguide Integrated with Efficient SiON Waveguide Coupler" *Opt. Express* **2008**, 16, 6425.

[10] T. Kamins, "*Polycrystalline silicon for integrated circuits and displays*" Kluwer Academic Publishers, **1998**.

[11] P. Mehta, N. Healy, T. D. Day, J. R. Sparks, P. J. A. Sazio, J. V. Badding, and A. C. Peacock, "All-Optical Modulation Using Two-Photon Absorption in Silicon Core Optical Fibers" *Opt. Express* **2011**, 19, 19078.

[12] P. Mehta, N. Healy, N. F. Baril, P. J. A. Sazio, J. V. Badding, and A. C. Peacock, "Nonlinear Transmission Properties of Hydrogenated Amorphous Silicon Core Optical Fibers" *Opt. Express* **2010**, 18, 16826.

[13] P. St. J. Russell, "Photonic Crystal Fibers" *Science* **2003**, 299, 358.

[14] T. T. Larsen, A. Bjarklev, D. S. Hermann, and J. Broeng, "Optical Devices Based on Liquid Crystal Photonic Bandgap Fibres" *Opt. Express* **2003**, 11, 2589.

[15] F. Benabid, J. C. Knight, G. Antonopoulos, and P. St. J. Russell, "Stimulated Raman Scattering in Hydrogen-Filled Hollow-Core Photonic Crystal Fiber" *Science*, **2002**, 298, 399.

[16] M. A. Schmidt, L. N. P. Sempere, H. K. Tyagi, C. G. Poulton, and P. St. J. Russell, "Waveguiding and Plasmon Resonances in Two-Dimensional Photonic Lattices of Gold and Silver Nanowires" *Phys. Rev. B* **2008**, 77, 033417.

[17] M. F. Danisman, J. A. Calkins, P. J. A. Sazio, D. L. Allara, and J. V. Badding, "Organosilane Self-Assembled Monolayer Growth from Supercritical Carbon Dioxide in Microstructured Optical Fiber Capillary Arrays" *Langmuir* **2008**, 24, 3636.

[18] P. J. A. Sazio, A. Amezcua-Correa, C. E. Finlayson, J. R. Hayes, T. J. Scheidemantel, N. F. Baril, B. R. Jackson, D. J. Won, F. Zhang, E. R. Margine, V. Gopalan, V. H. Crespi, and J. V. Badding, "Microstructured Optical Fibers as High-Pressure Microfluidic Reactors" *Science* **2006**, 311, 1583.

[19] P. Steinvurzel, E. D. Moore, E. C. Magi, and B. J. Eggleton, "Tuning Properties of Long Period Gratings in Photonic Bandgap Fibers" *Opt. Lett.* **2006**, 31, 2103.

[20] T. T. Alkeskjold, J. Laegsgaard, A. Bjarklev, D. S. Hermann, Anawati, J. Broeng, J. Li, and S. Wu, "All-Optical Modulation in Dye-Doped Nematic Liquid Crystal Photonic Bandgap Fibers" *Opt. Express* **2004**, 12, 5857.

[21] H. K. Tyagi, M. A. Schmidt, L. P. Sempere, and P. S. J. Russell, "Optical Properties of Photonic Crystal Fiber with Integral Micron-Sized Ge Wire" *Opt. Express* **2008**, 16, 17227.

[22] X. Zhang, R. Wang, F. M. Cox, B. T. Kuhlmey, and M. C. J. Large, "Selective Coating of Holes in Microstructured Optical Fiber and its Application to In-Fiber Absorptive Polarizers" *Opt. Express* **2007**, 15, 16270.

[23] C. M. B. Cordeiro, E. M. dosSantos, C. H. B. Cruz, C. J. S. deMatos, and D. S. Ferreira, "Lateral Access to the Holes of Photonic Crystal Fibers - Selective Filling and Sensing Applications" *Opt. Express* **2006**, 14, 8403.

[24] L. Xiao, W. Jin, M. Demokan, H. L. Ho, Y. L. Hoo, and C. Zhao, "Fabrication of Selective Injection Microstructured Optical Fibers with a Conventional Fusion Splicer" *Opt. Express* **2005**, 13, 9014.

[25] Y. Huang, Y. Xu, and A. Yariv, "Fabrication of Functional Microstructured Optical Fibers through a Selective-Filling Technique" *Appl. Phys. Lett.* **2004**, 85, 5182.

[26] Y. Wang, S. Liu, X. Tan, and W. Jin, "Selective-Fluid-Filling Technique of Microstructured Optical Fibers" *J. Lightw. Technol.* **2010**, 28, 3193.

[27] B. T. Kuhlmey, B. J. Eggleton, and D. K. C. Wu, "Fluid-Filled Solid-Core Photonic Bandgap Fibers" *J. Lightw. Technol.* **2009**, 27, 1617.

[28] M. Vieweg, T. Gissibl, S. Pricking, B. T. Kuhlmey, D. C. Wu, B. J. Eggleton, and H. Giessen, "Ultrafast Nonlinear Optofluidics in Selectively Liquid-Filled Photonic Crystal Fibers" *Opt. Express* **2010**, 18, 25232.

[29] J. R. Sparks, J. L. Esbenshade, R. He, N. Healy, T. D. Day, D. W. Keefer, P. J. A. Sazio, A. C. Peacock, and J. V. Badding, "Selective Semiconductor Filling of Microstructured Optical Fibers" *J. Lightw. Technol.* **2011**, 29, 2005.

[30] B. T. Kuhlmey, K. Pathmanandavel, and R. C. McPhedran, "Multipole Analysis of Photonic Crystal Fibers with Coated Inclusions" *Opt. Express* **2006**, 14, 10851.

[31] P. Mehta, M. Krishnamurthi, N. Healy, N. F. Baril, J. R. Sparks, P. J. A. Sazio, V. Gopalan, J. V. Badding, and A. C. Peacock, "Mid-Infrared Transmission Properties of Amorphous Germanium Optical Fibers" *Appl. Phys. Lett.* 2010, 97, 071117.

[32] R. He, P. J. A. Sazio, A. C. Peacock, N. Healy, J. R. Sparks, M. Krishnamurthi, V. Gopalan, and J. V. Badding, "Integration of Gigahertz-Bandwidth Semiconductor Devices Inside Microstructured Optical Fibres" *Nature Photon*. **2012**, 6, 174.

[33] R. He, T. D. Day, M. Krishnamurthi, J. R. Sparks, V. Gopalan, P. J. A. Sazio, and J. V. Badding, "Silicon p-i-n Junction Fibers" *Adv. Mater.* **2012**, DOI: 10.1002/adma.201203879.

[34] N. Healy, J. R. Sparks, M. N. Petrovich, P. J. A. Sazio, J. V. Badding, and A. C. Peacock, "Large Mode Area Silicon Microstructured Fiber with Robust Dual Mode Guidance" *Opt. Express* **2009**, 17, 18076.

[35] B. Jalali and S. Fathpour, "Silicon Photonics" *J. Lightw. Technol.* **2006**, 24, 4600.

[36] M. A. Foster, K. D. Moll, and A. L. Gaeta, "Optimal Waveguide Dimensions for Nonlinear Interactions" *Opt. Express* **2004**, 12, 2880.

[37] M. Lipson, "Overcoming the Limitations of Microelectronics Using Si Nanophotonics: Solving the Coupling, Modulation and Switching Challenges" *Nanotechnol.* **2004**, 15, S622.

[38] V. Raghunathan, D. Borlaug, R. R. Rice, and B. Jalali, "Demonstration of a Mid-Infrared Silicon Raman Amplifier" *Opt. Express* **2007**, 15, 14355.

[39] V. Raghunathan, H. Renner, R. R. Rice, and B. Jalali, "Self-Imaging Silicon Raman amplifier" *Opt. Express* **2007**, 15, 3396.

[40] L. Yin, Q. Lin, and G. P. Agrawal, "Soliton Fission and Supercontinuum Generation in Silicon Waveguides" *Opt. Lett.* **2007**, 32, 391.

[41] N. Healy, J. R. Sparks, R. He, P. J. A. Sazio, J. V. Badding, and A. C. Peacock, "High Index Contrast Semiconductor ARROW and Hybrid ARROW Fibers" *Opt. Express* **2011**, 19, 10979.

[42] J. C. Knight, T. A. Birks, P. St. J. Russell, and D. M. Atkin, "All-Silica Single-Mode Optical Fiber with Photonic Crystal Cladding" *Opt. Lett.* **1996**, 21, 1547.

[43] J. M. Dudley and J. R. Taylor, "Ten Years of Nonlinear Optics in Photonic Crystal Fibre" *Nature Photon.* **2009**, 3, 85.

[44] W. J. Wadsworth, R. M. Percival, G. Bouwmans, J. C. Knight, and P. St. J. Russell "High Power Air-Clad Photonic Crystal Fibre Laser" *Opt. Express* **2003**, 13, 48.

[45] J. B. Jensen, L. H. Pedersen, P. E. Hoiby, L. B. Nielsen, J. R. Folkenberg, J. Riishede, D. Noordegraaf, K. Nielsen, A. Carlsen, and A. Bjarklev, "Photonic Crystal Fiber Based Evanescent-Wave Sensor for Detection of Biomolecules in Aqueous Solutions" *Opt. Lett.* **2004**, 29, 1974.

[46] R. F. Cregan, B. J. Mangan, J. C. Knight, T. A. Birks, P. St. J. Russell, P. J. Roberts, D. C. Allan, "Single-Mode Photonic Band Gap Guidance of Light in Air" *Science* **1999**, 285, 1537.

[47] N. M. Litchinitser, A. K. Abeeluck, C. Headley, and B. J. Eggleton, "Antiresonant Reflecting Photonic Crystal Optical Waveguides," *Optics letters*, 2002.

[48] N. M. Litchinitser, S. C. Dunn, B. Usner, and B. J. Eggleton, "Resonances in Microstructured Optical Waveguides" *Opt. Lett.* **2002**, 27, 1592.

[49] J. M. Stone, G. J. Pearce, F. Luan, T. A. Birks, J. C. Knight, A. K. George, and D. M. Bird, "An Improved Photonic Bandgap Fiber Based on an Array of Rings" *Opt. Express* **2006**, 14, 6291.

Chapter 4

High Pressure Organometallic Reactions for HPCVD of II-VI Semiconductors

A major challenge in depositing low loss, high quality compound semiconductor materials inside fiber pores is that the HPCVD precursor chemistry is much more complex than that for unary semiconductors like silicon and germanium, which can be deposited in the amorphous state from simple hydrides as discussed in **Chapters 2 and 3**. In this chapter, the synthesis of polycrystalline II-VI compound semiconductors such as ZnSe, ZnS, $ZnS_xSe_{(1-x)}$, and ZnO is discussed, which involves methods to "encapsulate" reactive species before they enter the high aspect ratio pores of MOFs. The principles of the chemistry and the materials characterization focus on ZnSe reaction chemistry, primarily because the goal of this dissertation is to demonstrate the first Cr^{2+}:ZnSe optical fiber laser, but they are generally applicable to other compound semiconductors.

4.1 Synthesis and Pyrolysis of Single Source Precursors

Pre-reaction of source molecules in HPCVD must be avoided because of the need to have the molecules intimately mixed at high pressure before they enter the reactor. Since many of the known reactions to deposit II-VI semiconductors are plagued by such detrimental pre-reactions, the first reactions that were studied were based on the pyrolysis of molecules that contain both elements in them, known as single source precursors. Initial studies of ZnSe deposition were performed using a synthesized solid state precursor, $Zn[(SePR_2)_2N]_2$, where R=phenyl or iPr, which has been shown to deposit thin films of ZnSe by low pressure organometallic chemical

vapor deposition.[1-3] The precursor was synthesized using reported methods[4,5] with the assistance of Matthew R. Dirmyer of the Sen group (Chemistry, PSU) and confirmed with NMR spectroscopy. The precursor chemical structure, determined by single crystal X-ray diffraction (XRD), is shown in **Figure 4.1a**.

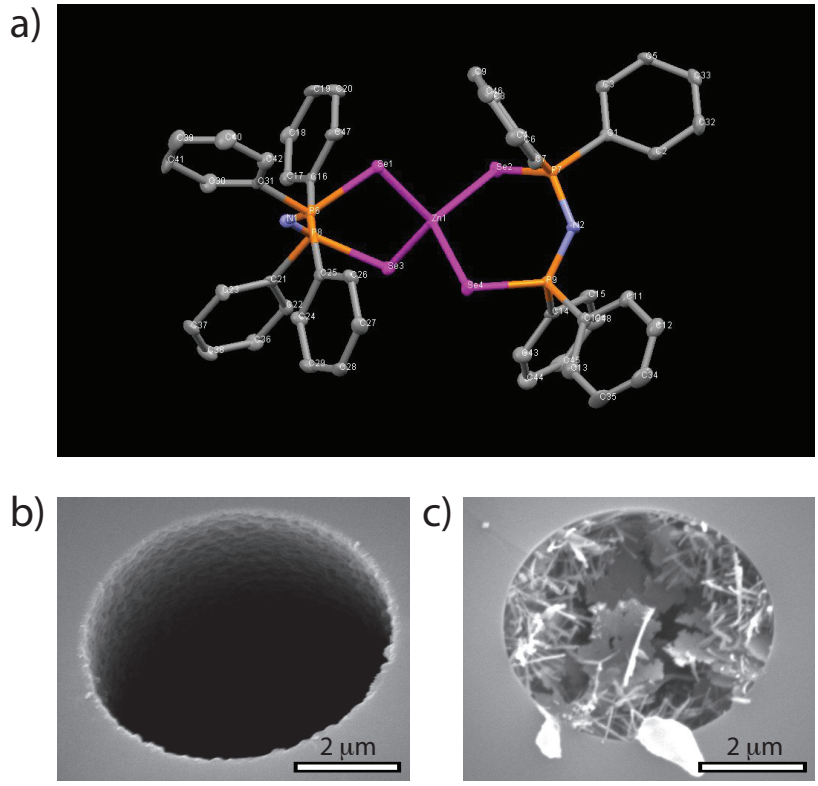

Figure 4.1: Deposition of ZnSe from single source precursors. (a) Structure of the $Zn[(SePPh_2)_2N]_2$ determined by single crystal XRD. The R=Ph precursor produces rough films (b), while the R=iPr precursor produces wires and platelets.

The precursor was dissolved in supercritical CO_2 and configured to flow down a capillary that was heated to 500 °C. The deposition was successful: polycrystalline, cubic ZnSe was deposited inside of capillary pores, as determined by powder XRD. However, the morphology of the film was very rough due to undesirable homogeneous growth in the fluid phase in addition to the desired heterogeneous growth on the surface. The R-group affected the resulting morphology;

the R=Ph precursor produced rough films (**Figure 4.1b**), while the R=iPr precursor produced wires and platelets (**Figure 4.1c**).

Controlling the concentration of the precursor in supercritical CO_2 resulted in a more uniform film, but it was still far too rough and could not be grown thick enough for waveguiding applications (**Figure 4.1b**); primarily because homogeneous growth could not be avoided along the entire length of the furnace. Furthermore, the material did not have the necessary high purity for optical applications, as evident from the intense visible photoluminescence under 514 nm excitation, typically associated with Se vacancies and P impurities. For these reasons, a dual source, high purity approach was taken, which allows for much more control over the reaction conditions, but requires a creative approach to the HPCVD chemistry.

4.2 Multiple Source Reactions with Alkyls

4.2.1 Sulfides and Selenides

An important practical difference in HPCVD compared to CVD is that reaction precursors must often be transported together for delivery into a heated reaction zone whereas conventional CVD reactors typically allow for the introduction of precursors separately to avoid prereaction before they reach a planar deposition target (see **Figure 2.4**). Thus the precursors selected for multi-source HPCVD must be chosen so that they do not prereact as they are transported to a desired deposition location at low temperature, yet do react once they reach it and are heated. Another challenge is that the deposition characteristics can change as a void is filled with semiconductor because the precursor flow rate is altered as a result of the changes in geometry due to pore closure, which was discussed in detail in **Chapter 2**. A significant difference from the amorphous silicon and germanium HPCVD is that the II-VI semiconductors

deposit as a polycrystalline film, in which mass transport rate to the surface affects grain growth.[6]

The organometallic molecules R_2Zn, R_2S, and R_2Se, where R=alkyl, are particularly suitable for HPCVD of II-VI semiconductors. These liquid precursors have appreciable vapor pressures, making them viable for vapor deposition reactions,[7,8] but they do not introduce as many impurities as the solid, single source precursors with complex aryl-carbon ligands discussed in the previous section.[9] Furthermore, the precursor reactivity can be controlled by tuning the metal-carbon bond strength with different R groups. For example, branched t-butyl groups allow for lower reaction temperatures.[10] These alkyl precursors also do not suffer from room temperature prereactions in contrast to the $R_2Zn/H_2S/H_2Se$ precursors commonly employed for zinc chalcogenide CVD.[11] R_2S and R_2Se are weaker Lewis bases than H_2S/H_2Se that do not react as readily with the Lewis acid alkyl zinc. Instead, the reactive, intermediate chalcogenide hydrides are formed in situ at the desired deposition location by reaction between alkyl-chalcogenides and H_2 (Reaction 2). The R=methyl precursors were chosen because they are volatile (vapor pressures ~20 – 40 kPa at room temperature) and readily available in electronic grade purity. The following reaction steps are thought to occur at the targeted deposition site:[12]

$$(CH_3)_2Zn_{(g)} + H_{2(g)} \rightarrow Zn_{(g)} + 2CH_{4(g)} \qquad \textbf{(Reaction 4.1)}$$

$$(CH_3)_2S/(CH_3)_2Se_{(g)} + 2H_{2(g)} \rightarrow H_2S/H_2Se_{(g)} + 2CH_{4(g)} \qquad \textbf{(Reaction 4.2)}$$

$$Zn_{(g)} + H_2S/H_2Se_{(g)} \rightarrow ZnS/ZnSe_{(s)} + H_{2(g)} \qquad \textbf{(Reaction 4.3)}$$

Thus the organometallic precursors "encapsulate" the more reactive Zn and H_2S/H_2Se species until the reaction temperature is high enough to induce Reactions 4.1 and 4.2, followed by 4.3.

In a typical deposition, the volatile organometallic precursor mixture is pressurized with H_2, which functions as a reactant and carrier, to a total pressure of 35 – 70 MPa and configured to flow through a heated (400 – 500 °C) capillary (see **Figure 2.4**) with the opposite end open to atmospheric pressure. The pressure differential between the ends allows for the transport of the

precursor molecules into the high aspect ratio pores. When the MOF is heated, a heterogeneous reaction occurs on the surface of the silica capillaries with a typical precursor conversion efficiency of ~15%[13,14] while the reaction byproducts, such as methane, unreacted precursors, and carrier gas are exhausted downstream. The conformal, heterogeneous nature of the early stages of deposition is highlighted in **Figure 4.2a**. In contrast to the single source precursors, the film continues to become thicker and the interior pore decreases in diameter as the completely heterogeneous reaction proceeds.

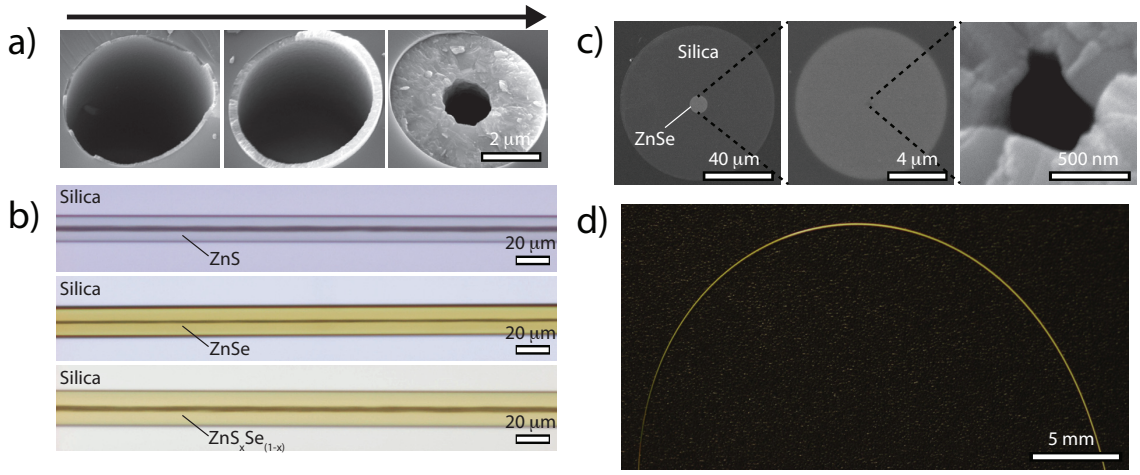

Figure 4.2: HPCVD of II-VI Semiconductors.[14] (a) SEM images of a HPCVD deposition as it progresses and conformally coats the inner surface of a silica capillary. (b) Diascopically illuminated optical micrographs from the side showing transparent, uniform ZnS, ZnSe, and $ZnS_xSe_{(1-x)}$ deposited in silica micro-capillaries. (c) Overview (left) and higher magnification (right) cross-sectional SEM images of a ZnSe infiltrated capillary. (d) Photograph of ZnSe microwires being bent while embedded in the silica MOF.

ZnS layers are formed by the reaction of $(CH_3)_2S$ and $(CH_3)_2Zn$ and ZnSe layers are formed by the reaction of $(CH_3)_2Se$ and $(CH_3)_2Zn$ in 15 μm capillaries (**Figure 4.2b**). The layers are transparent and conformally coat the capillaries so well that at the end of the deposition the remaining central void can be as small as 400 nm in diameter, when the reaction parameters are properly tuned (**Figure 4.2c**); see **Section 4.4.1**. By the introduction of both $(CH_3)_2S$ and $(CH_3)_2Se$ into the reactant flow, solid solutions of ZnSe and ZnS can be deposited in well-

developed layers (**Figure 4.2b**). The kinetic rate constants for decomposition of these two molecules differ, allowing the challenge of controlling the S to Se ratio of the $ZnS_xSe_{(1-x)}$ solid solution to be met by varying the temperature and precursor ratio. Employing R=iPr groups for the sulfur source would allow the stoichiometry to be controlled by only one variable (the ratio), because the reaction temperatures of $(CH_3)_2Se$ and $(iPr)_2S$ should be similar due to the weakened S-R bond. This is important for controlling the stoichiometry along centimeter length scales for optical fiber applications discussed in **Chapter 5**. The microwires can be several centimeters long (**Figure 4.2d**), which is ideal for fabricating short length optical fiber devices such as fiber lasers.

4.2.2 Effects of Reactant Ratio

The morphology, composition, and crystallinity of the deposited ZnSe material are very sensitive to the stoichiometric ratio of the precursors in the reactant flow **(Figure 4.3**). Only a very narrow range of stoichiometry produces well developed, conformal films. Similar trends are also observed for ZnS and $ZnS_xSe_{(1-x)}$. This sensitivity to precursor stoichiometry arises from the different kinetic rate constants for Reactions 4.1 and 4.2. When the VI/II precursor ratio is low (<1), a ZnSe film is deposited along with metallic zinc islands (**Figure 4.3a**). Complete conversion of Zn to ZnSe is achieved when the ratio is >1, with 2 being the best ratio with respect to morphology, texture, and stoichiometry (**Figure 4.3b**). A further increase of the ratio (>2.5) leads to columnar growth in the (111) direction, with a greater relative intensity of the (111) diffraction peak (**Figure 4.3c**). Elemental Se formation at even higher ratios (>5) is not observed, due to the high temperature needed for decomposition of H_2Se in H_2.[15] For ZnS deposition, the more stable sulfur-carbon bonds of the $(CH_3)_2S$ molecule result in a smaller Reaction 2 rate constant, requiring a higher VI/II ratio (~10). Again, these ratios can be tuned by changing the R group on the source molecule.

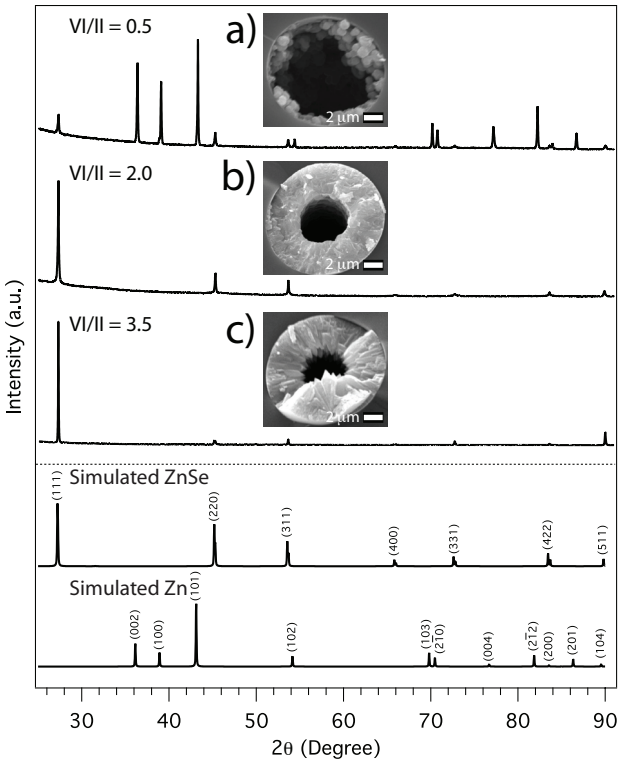

Figure 4.3: Effects of reactant ratio in II-VI semiconductor deposition.[14] XRD (Cu Kα) reveals the composition/morphology dependence on precursor ratio for ZnSe deposition. When the VI/II precursor ratio is too low (<1), a ZnSe film is deposited along with metallic zinc islands (a). Complete conversion of Zn to ZnSe with minimal texturing occurs when the ratio is >1 (b), while a high ratio (>2.5) results in columnar growth in the (111) direction (c).

Although $ZnS_xSe_{(1-x)}$ materials can crystallize in either the hexagonal wurtzite structure or the cubic zinc blende structure as the composition is varied,[16] powder XRD showed that only the cubic structure was formed in HPCVD when stoichiometries were varied over the entire range from x=0 to x=1. The S to Se ratio determined by energy dispersive spectroscopy for materials deposited at different temperature agreed well with that determined from the measured lattice parameters via Vegard's law (**Figure 4.4**). The ability to tune the lattice constant of the material allows for tuning of the refractive index and bandgap of the material, which allows for more design freedom in II-VI semiconductor optical fibers.

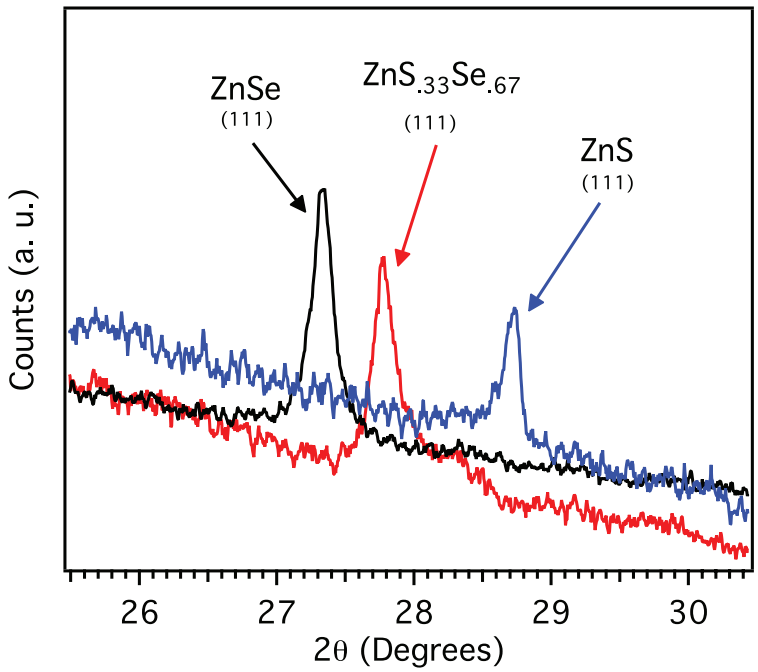

Figure 4.4: Vegard's law analysis of $ZnS_xSe_{(1-x)}$ alloys. The shift in the (111) diffraction peak is consistent with the stoichiometry of the material determined by energy dispersive spectroscopy.

4.3 The Central Void

4.3.1 Flow Effects on Filling: Minimizing the Void Size

The central void appears much larger than it actually is in the optical micrographs shown in **Figure 4.2** because it is magnified by cylindrical lensing of the semiconductor and the silica. Unlike the SiH_4 pyrolysis chemistry discussed in **Chapter 2**, the more complex chemistry of the II-VI semiconductors produces larger byproducts that cannot diffuse out of the silica capillary. Although higher order alkyls may form as byproducts, the predominant byproduct is likely methane, with a kinetic diameter of 3.8 Å compared to the interstitial spacing of ~3.0 Å in silica. This methane byproduct in the II-VI deposition reaction builds up in the pore once it clogs (**Figure 4.5**); with no way of exhausting it through the ~3.0 Å interstitial spacing of the silica, the

forward reaction becomes inhibited. In order to make the hole as small as possible, it is important to understand the formation mechanism of the plug; in contrast to the amorphous deposition of the unary semiconductors, the II-VI film deposits in the polycrystalline form.

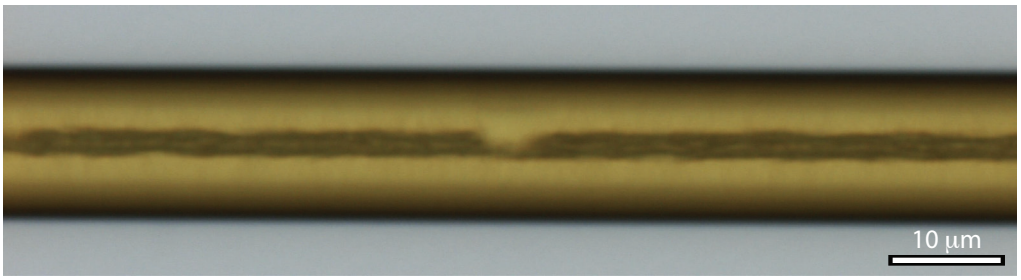

Figure 4.5: Plug formation in ZnSe deposition. Once a plug forms, the methane byproduct builds up and arrests the deposition of ZnSe.

As the deposition progresses and the tube interior diameter becomes smaller, the flow rate decreases, which decreases the rate of mass transport and the annular film growth rate. With a slower growth rate, reaction intermediates have more time to move to the low energy sites on the deposition surface and growth of larger grains is promoted. These large grains grow towards the inner cavity and form rough inner surfaces when they meet. The cross-sectional grain structure of ZnSe can be revealed with grain boundary etching with boiling NaOH solution and transmission electron microscopy (TEM) (**Figure 4.6**). It can be seen that as the deposition progresses and the pore decreases in diameter, the mass transport into the pore decreases (due to the D^4 dependence of compressible laminar flow), which results in the growth of larger grains. The grains grow from the outside-in in the (111) direction, however the grains pinch each other off as the pore gets smaller, which results in a few large grains that make up the final remaining hole cross-section.

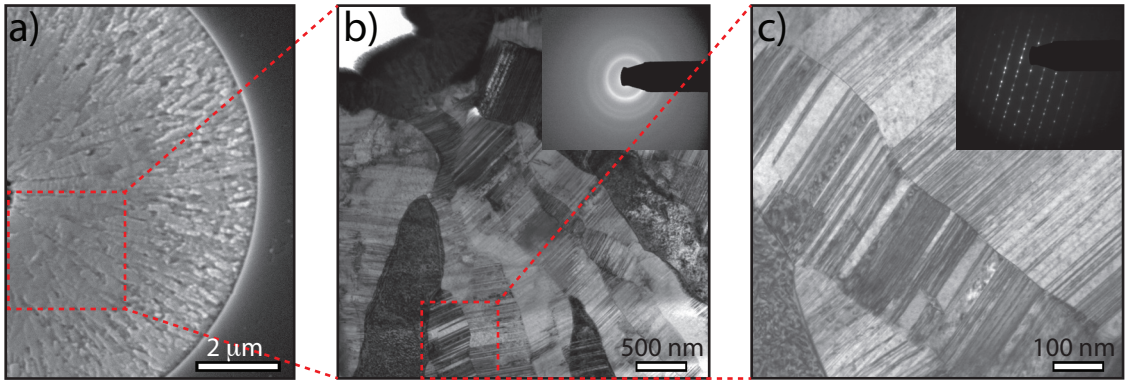

Figure 4.6: Cross-sectional grain structure in ZnSe deposition. (a) Grain structure revealed by etching in NaOH. (b,c) TEM images show the (111) direction of the polycrystalline growth, revealing significant stacking faults.

Increasing the pressure increases the flow rate and thus the mass transport, which will promote growth of smaller grains (due to the P^2 dependence of compressible laminar flow) that will not pinch each other off as quickly and form a smaller, smoother hole. Control experiments with deposition in 1.7 µm diameter silica capillaries confirm that slower flow rates lead to irregular deposition with large grain size while faster flow rates lead to more uniform deposition (**Figure 4.7**). When a total pressure of 70 MPa was used, growth proceeds until the tube interior diameter is as small as 400 nm (**Figure 4.2c**), forming a nearly void-free core. Thus the aspect ratio of the central ~400 nm nanopore is ~10^5 when deposition is halted by termination of flow, illustrating the ability of HPCVD to transport compound semiconductor precursors into very deep voids, similarly to silicon. Through the use of higher pressures, the interior diameter could be reduced even further or the hole could even be eliminated. The chemical reaction rate also affects the central hole size, with pure H_2 as a carrier gas providing the fastest deposition rate and thus the smallest resulting hole compared to helium dilutions of the precursor mixture. Using higher source molecule partial pressures by heating the liquid sources in the flow could also result in a smaller hole size.

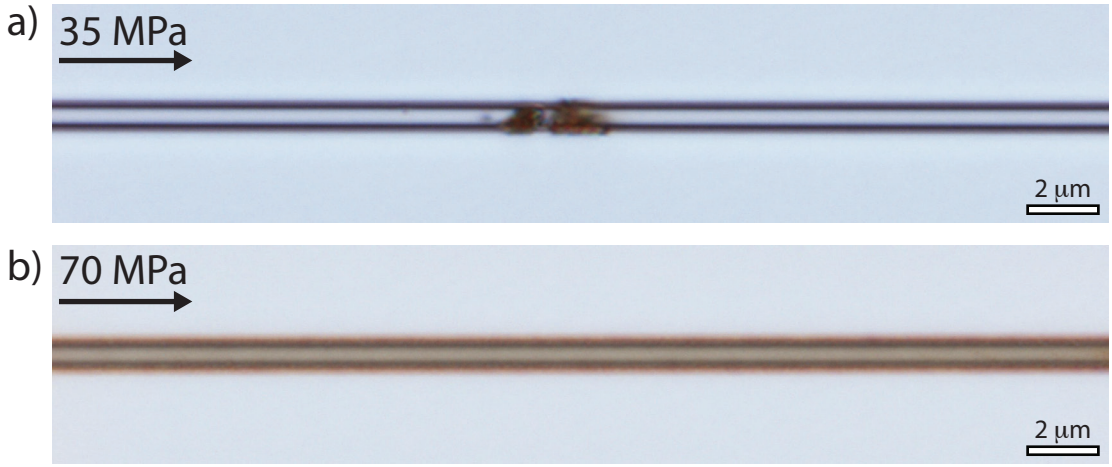

Figure 4.7: Effects of mass transport on ZnSe deposition in a 1.7 μm capillary.[13] When the flow of precursor mixture is driven by a 35 MPa pressure differential, well-developed films do not form on the pore walls (a). In contrast, a higher flow rate driven by 70 MPa allows for conformal, annular growth (b).

4.3.2 Equilibrium Annealing: Removing the Void

Although moving to higher pressures can result in a smaller central void, it seems likely that there will always be a small hole in the core due to the build up of methane as well as the competition between a D^4 dependence and P^2 dependence of mass transport. This hole will affect optical fiber performance: finite element modeling predicts that even a 10 nm hole will affect the mode structure of the waveguide. One could consider cycling the precursor in and out of the channel once the plug forms to fill in the remaining hole, but that would be a slow, layer-by-layer process. From what is known from the SiH_4 pyrolysis, it becomes evident that a reaction that does not have large, or any, byproducts is necessary to mimic the backfilling mechanism.

When exploring the literature of ZnSe crystal growth as well as the exploded preform in **Figure 1.2**, it becomes apparent that ZnSe is volatile at high temperature and can be transported in the vapor phase. This is a well-known way to grow a single crystal, which will be discussed in **Section 4.3.3**. Kato *et.al.* at Ibaraki University, Japan also noticed an interesting phenomenon

when annealing ZnSe substrates for epitaxial growth (**Figure 4.8**).[17] When the wafer was annealed at 1165 °C for 5 hours, the shape of the resulting crystal was no longer a wafer, but instead a sphere, with the total volume staying constant. They concluded that the mobility of the ZnSe at these temperatures allows the system to minimize the surface energy and transform from a disc into a sphere via the following reactions:

$2ZnSe_{(s)} \rightarrow 2Zn_{(g)} + Se_{2(g)}$ (**Reaction 4.4**)

$2Zn_{(g)} + Se_{2(g)} \rightarrow ZnSe_{(s)}$ (**Reaction 4.5**)

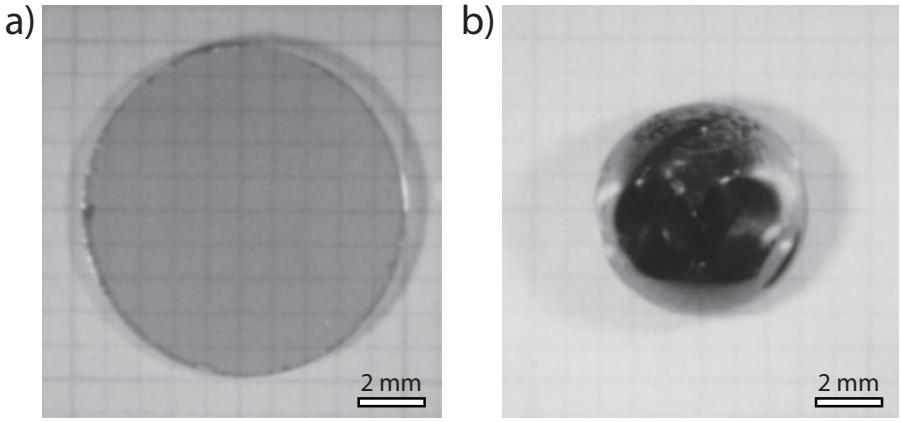

Figure 4.8: Minimization of surface energy in bulk ZnSe. After annealing at 1165 °C for 5 hours, a wafer (a) becomes a sphere (b). Images reproduced with permission from reference [17], © 2000 Elsevier.

In a HPCVD ZnSe wire, the fact that the small, high curvature void has a high surface energy should drive the system to eliminate the void. Indeed, a similar effect is observed in a HPCVD ZnSe wire that is removed from the silica capillary with HF etching. The wire becomes many smaller, void free spheres when heated to 900 °C in a sealed volume (**Figure 4.9**). However, it is desirable for the ZnSe to maintain the wire geometry and not form spheres. This surface energy minimization process should also occur in the templated regime, where the ZnSe wire is still embedded in the silica capillary, to remove the central void. Also, it is possible that spheres will not form because the silica/ZnSe interface is likely more energetically favorable than the bare ZnSe surface in the non-templated regime. It is important to note that this sublimation

and re-deposition reaction does not have any byproducts that would have to leave the capillary. Thus it should be possible to mimic the backfilling mechanism with this dissociative-sublimation/re-deposition reaction.

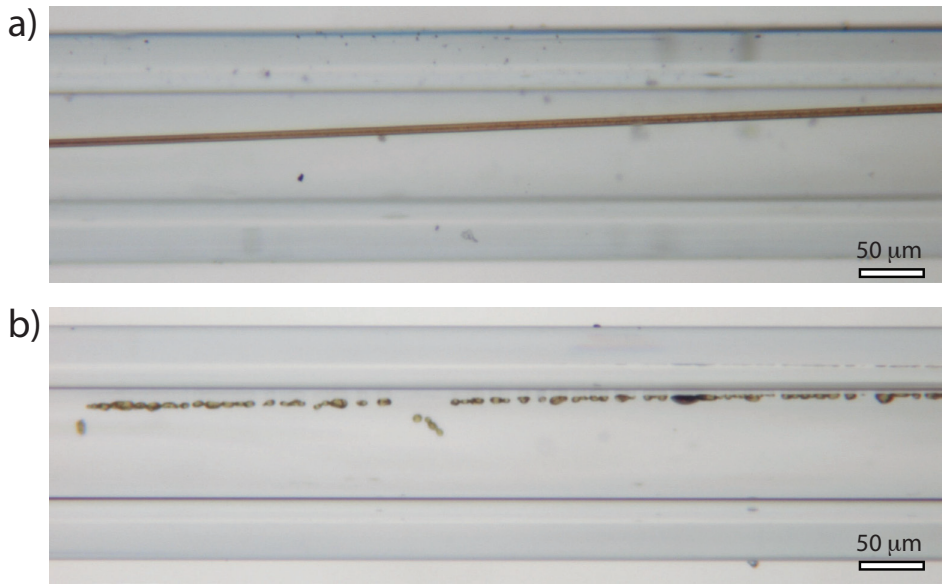

Figure 4.9: Minimization of surface energy in a HPCVD ZnSe wire. An etched out HPCVD wire (a) tends to form small, void free spheres (b) when heated at 900 °C for 36 hours and not confined in the capillary template.

A small volume ampoule is needed to carry out the templated experiment so that a vapor pressure can be established without all of the ZnSe exiting the capillary. To accomplish this, an optical fiber fusion splicer was used to fabricate micro-ampoules out of 150 µm inner diameter capillaries. The 125 µm outside diameter ZnSe sample can then be sealed under vacuum to anneal it at high temperature (**Figure 4.10a**). The results of the templated, equilibrium annealing are shown in **Figure 4.10**, where a HPCVD ZnSe fiber was annealed at 900 °C for 12 hours. Indeed, the central hole is removed over the length of the fiber, while maintaining the original wire geometry. The ends of the waveguide are sacrificed to fill in the central void and establish the vapor pressure in the ampoule. Since the dissociative-sublimation/re-deposition reaction does not produce a byproduct that has to exit the capillary, the backfilling mechanism can be mimicked because the annealing takes place in a small temperature gradient. Through a series of

experiments, it was found that complete filling of the fiber can be achieved in about 5 hours at 1000 °C, in 12 hours at 900 °C, and 48 hours at 800 °C. Also, the elevated temperatures result in significant grain growth (**Figure 4.9e**) as well as elimination of many of the stacking faults and twinning planes that were observed in **Figure 4.6**. As will be shown in **Chapter 5**, the main source of optical loss in the II-VI semiconductor optical fibers is from scattering from grain boundaries; thus, the increased sized of grains and elimination of the central hole will significantly improve the loss of the optical fibers.

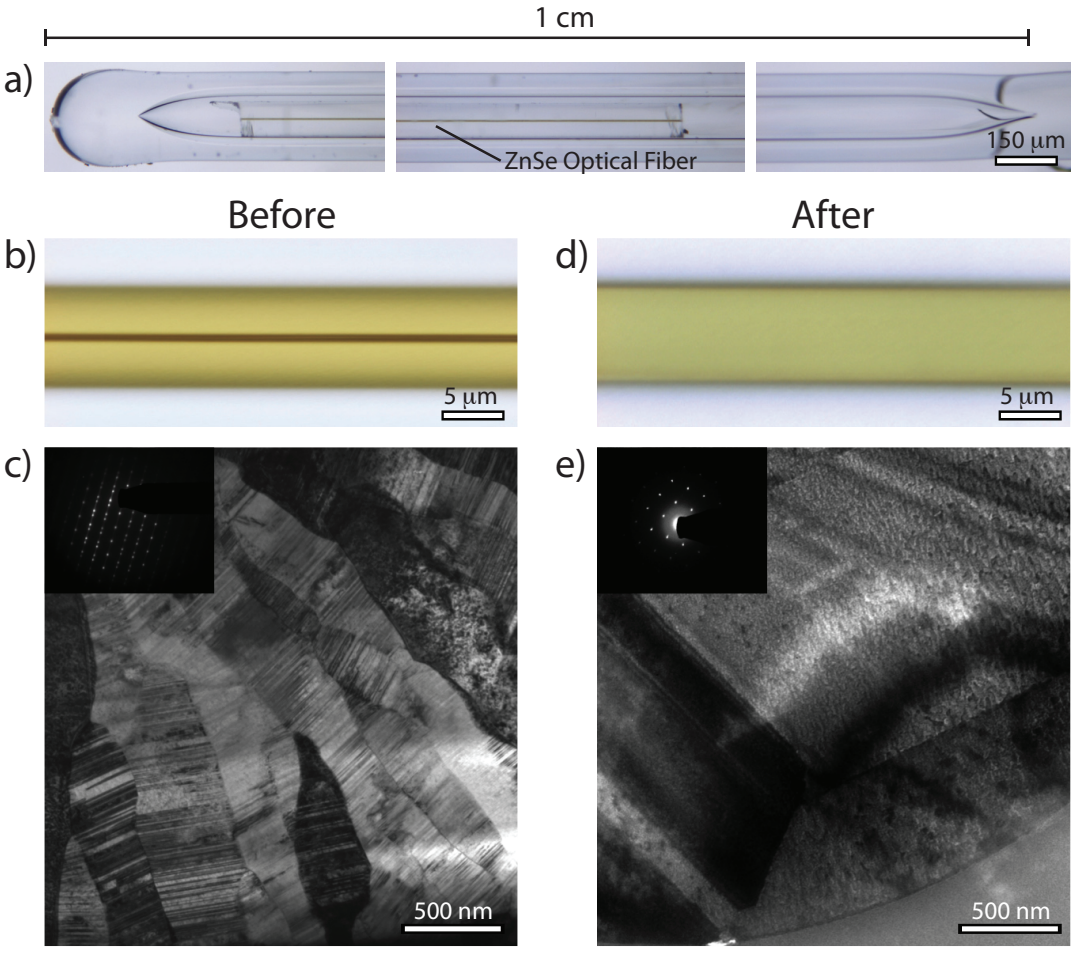

Figure 4.10: Templated, equilibrium annealing to remove the central void. a) Micro-ampoule fabricated with an optical fiber fusion splicer. Before annealing, the small hole is visible in the optical micrograph (b) and the grains are columnar with twinning defects as seen in TEM (c). After annealing, the central void is eliminated (d) and the grains grow into larger, less defective grains (e).

4.3.3 Single Crystal Vapor Transport in Micro-Ampoules

One traditional way to grow a single crystal is a chemical vapor transport (CVT) reaction,[18] where a material is placed in a temperature gradient and is transported from one end to the other by either evaporation or chemical reaction. For a chemical reaction, the transport direction is determined by the enthalpy change of the reaction.[18] ZnSe is a good candidate for CVT because it readily evaporates/dissociates into zinc and selenium dimer vapor without the need for a chemical transport agent (see reactions 4.4 and 4.5). This is shown in **Figure 4.11** for a bulk ampoule.[19] The transport is from left to right (high to low temperature) and is typically carried out around 900 – 1000 °C in vacuum or under H_2. Nucleation is favored at the tip of the taper since it is at the lowest temperature in the gradient and the shape of the taper tends to promote the nucleation of a single grain, which can grow into a larger single crystal.

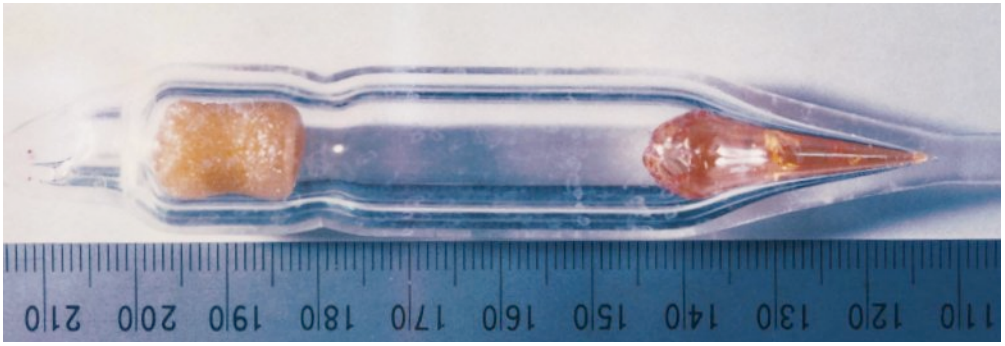

Figure 4.11: Inspiration for transport reactions within micro-capillaries. ZnSe can be transported from a powder source (left, high temperature) to grow a single crystal (right) at a lower temperature. Image reproduced with permission from reference [19], © 1998 Elsevier.

This type of reaction can be mimicked in a micro-ampoule, where a powder source (or a more pure ZnSe HPCVD waveguide as the source, as surface contamination of the powder is an issue) is loaded into a 150 μm fiber, similarly to the equilibrium annealing experiments in **Section 4.3.2**, which is then fusion spliced to a smaller sized target capillary (~10 μm) for transfer. **Figure 4.12a** shows a constructed micro-ampoule that can be fabricated using an optical fiber fusion

splicer. This ampoule can then be placed in a temperature gradient (source temperature = 1015 °C) to sublimate the ZnSe and deposit the material downstream in the targeted taper region that is at a lower temperature (860 °C) over a 24 hour time period (**Figure 4.12b**). Preliminary experiments show that the transport is possible, although there is a need for optimization of the process for the ZnSe to reach the seed point; this is likely due to the longer mean free path in the evacuated ampoule. Note that the mean free path will be on the order of micrometers at vacuum level pressures. Performing this micro-ampoule approach with a nitrogen/argon overpressure may allow the transport to take place in smaller pores that would allow the crystal growth to start at the seed point of the taper.

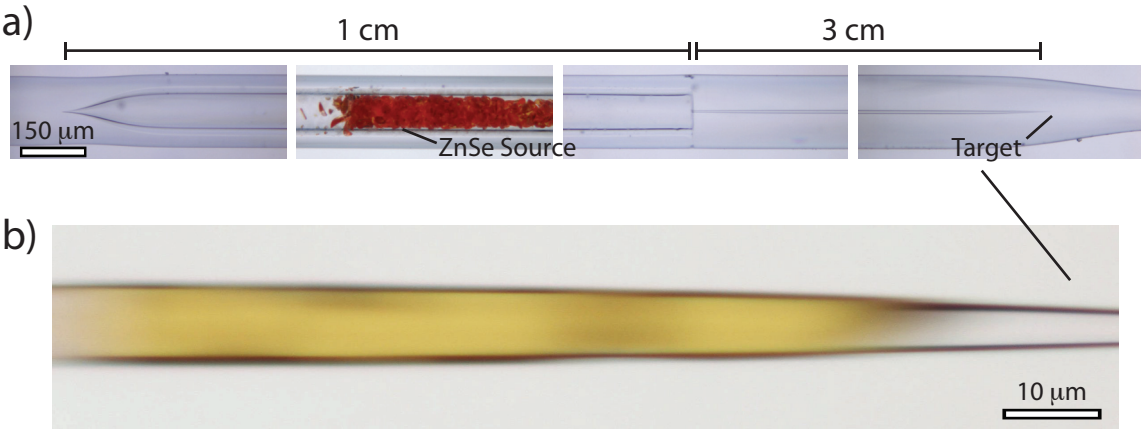

Figure 4.12: Single crystal ZnSe transport in a micro-ampoule. A micro-ampoule can be fabricated with an optical fusion splicer (a). After heating the ampoule in a temperature gradient (b), ZnSe is transported into the smaller 10 µm capillary to grow a single crystal back towards the source.

To determine whether or not the transported material is a single crystal, ion-induced secondary electron imaging was used to image the cross-section of a 50 µm diameter transported ZnSe wire (**Figure 4.13**). This technique can show contrast between different crystallographic planes at a surface and reveal grain structure.[20] Gallium ions were used to cut a trench into the sample (FEI Quanta 200 3D). Then, using gallium ions to induce secondary electron emission, the grain structure could be imaged along the axis of the fiber. For comparison, an as-deposited

HPCVD polycrystalline sample was also imaged (**Figure 4.13a,c**). The grain structure can be seen in the HPCVD sample, which agrees well to that observed with TEM and etching. In contrast, the fully filled CVT sample does not show such grain structure. Instead, it exhibits two levels of channeling contrast arranged in tilted streaks (**Figure 4.13b,d**). This type of contrast is consistent with a crystal that exhibits multiple twins. ZnSe often forms twins of this nature during crystal growth processes.[21-23] These preliminary results show that transport reactions within micro-capillaries can produce single crystals that should lead to lower loss optical fibers with minimal scattering from grain boundaries. A more thorough TEM study of the crystal is currently underway.

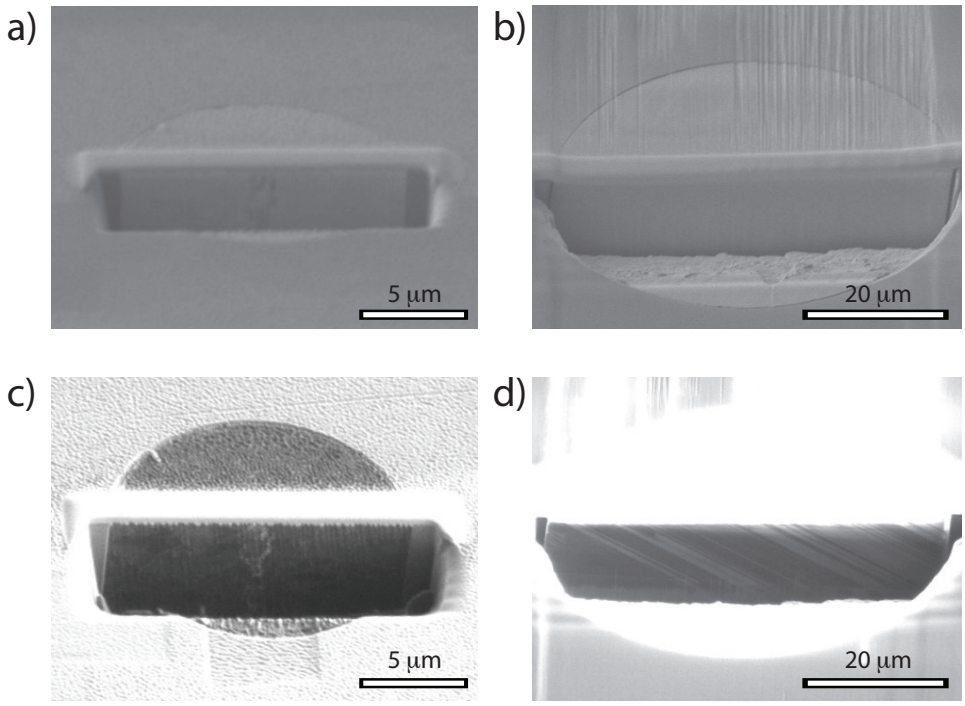

Figure 4.13: Ion-induced secondary electron imaging of a ZnSe single crystal. For comparison, a secondary electron (a,b) and ion-induced image (c, d) are shown for a HPCVD polycrystalline sample (a,c) and the transported, twinned single crystal (b,d).

Twinned crystals would have superior properties over polycrystalline materials for applications such as lasers, but for other applications such as exploitation of second order non-

linear phenomena, true single crystals are preferred. Formation of twins could be avoided by optimization of the growth conditions. Lower growth temperatures[21] enabled by high concentrations of a transporting agent such as H_2, which can accelerate the rate of transport because the Se in the ZnSe can react with it to form H_2Se, shifting the equilibrium further towards vaporization and transport, could lead to fewer defects. Alternatively, a different semiconductor for growth that is less susceptible to twinning could be employed. For example, ZnTe has much lower tendency to twin.[21] Furthermore, it would be especially desirable to orient this growth because seeded growth can also help to avoid the formation of twins. This seed could be obtained either by repeated deposition in a tapered fiber to nucleate and grow a particular orientation[24] or alternatively from a focused ion beam micro-machined wafer section placed within the ampoule.

4.3.4 Thermal Expansion Mismatch

Although there are many benefits of these annealing/transport processes, there is a significant barrier to use as optical fibers in that the exceptionally low thermal expansion coefficient of silica (0.5×10^{-6} K^{-1}) does not match that of ZnSe (5.0×10^{-6} K^{-1}).[25] This results in significant cracking of the sample as it is cooled down from the annealing or transport temperatures. As the fiber cools off, the ZnSe reduces in volume much more than silica and develops cracks every 20 μm (**Figure 4.14a**); very slow cooling rates (1.2 °C/hr) do not alleviate the cracking issues. To experimentally verify that the cracking is due to thermal expansion mismatch between ZnSe and silica and not from surface effects that could form small spheres[26] that were observed for the bare wire in **Figure 4.9**, a taper was etched in a HPCVD ZnSe waveguide prior to annealing at 900 °C for 15 minutes. This time period is too short for any surface energy minimization effects, but long enough for thermal expansion effects. As shown in **Figure 4.13b**, there are cracks after this short treatment even when the silica is very thin.

However, the completely exposed wire does not show any signs of cracking, which suggests that the thermal expansion mismatch is the cause of the cracking during the annealing/transport at high temperatures.

Cracking due to thermal expansion mismatch also becomes and issue even at the lower HPCVD reaction temperatures as the capillary size increases, with 50 μm being the largest capillary that can be filled with ZnSe with minimal crack density. Larger sizes, which are desirable for high power optical applications, form too many cracks to be useful as optical waveguides. This issue can be addressed by using different glass systems as micro-capillaries that have higher thermal expansion coefficients that are close to that of ZnSe. Aluminosilicate glasses have been drawn and investigated for HPCVD, which have shown promising signs of alleviating thermal expansion mismatch, but do not have a high enough glass transition temperature (T_g = 790 °C) for these high temperature processes. However, they are useful for fabricating large core optical fibers at the lower HPCVD temperatures, which will be discussed in **Chapter 5**.

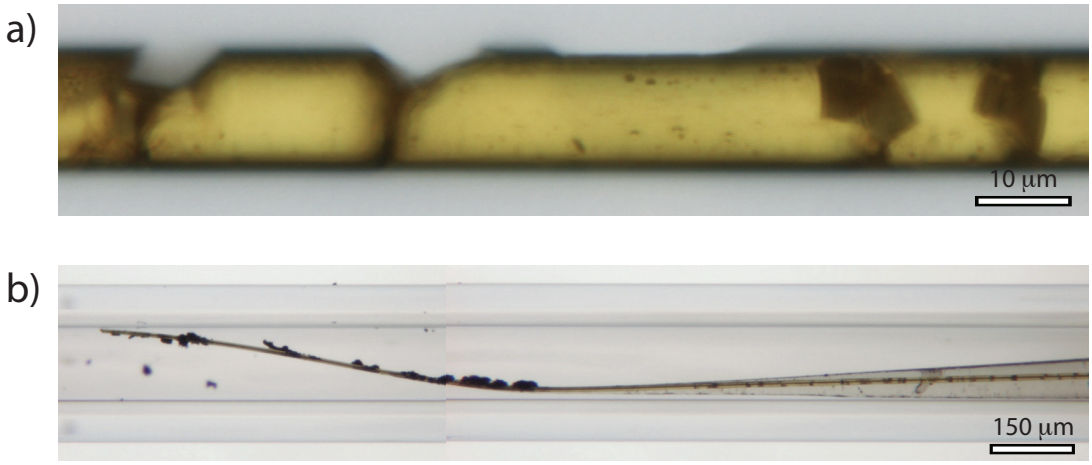

Figure 4.14: Thermal expansion mismatch of silica and ZnSe. (a) Cracking occurs every 20 μm in both equilibrium annealed samples and single crystals due to thermal expansion mismatch between silica and ZnSe. (b) Cracking occurs even when there is a very thin film of silica around the ZnSe. The black particles on the completely etched out wire (left) are residue left after etching the tapered structure.

With these void free filling techniques, it should be possible to produce long fully filled ZnSe optical fibers once a better thermal expansion matched capillary is obtained. Highly germania doped silica is an excellent candidate with a thermal expansion that is tunable with composition (and near that of ZnSe) while maintaining the mechanical properties of silica and high glass transition temperature (T_g > 900 °C).[27-29] This thermal expansion mismatch is an ongoing challenge in the field of semiconductor optical fibers and new cladding glasses are being developed.[30] For these reasons, all the optical fibers that will be presented in **Chapters 5 and 6** have a central void.

An alternative approach to cladding glass development is to first use a silica capillary as a template for a second cladding with desirable thermal properties such as SiC, Si_xN_y, or even diamond. The desired optical fiber can then be deposited within this second cladding. After the HPCVD process is completed, the silica can be etched away with HF to result in an optical fiber with a non-silica cladding consisting of the material that was first deposited. This structure would then be much less susceptible to thermal expansion mismatch during the annealing processes and could also provide better thermal conductivity than silica for high power fiber optic applications.

4.4 Zinc Oxide

ZnO has extensive optoelectronic and chemical/catalytic applications due to its wide bandgap and versatile photochemical properties,[31] but HPCVD of oxides has been challenging because nearly all potential chemical routes are inhibited by room temperature pre-reactions.

4.4.1 Oxidation of ZnSe Templates

An alternative route to ZnO is to use the ZnSe or ZnS microwires as templates that can be oxidized. Annealing of ZnSe in an oxygen atmosphere (100 kPa) at 800 – 1000 °C results in conversion to ZnO via the following reaction:[32]

$$2ZnSe_{(s)} + 3O_{2(g)} \rightarrow 2ZnO_{(s)} + 2SeO_{2(g)} \qquad \textbf{(Reaction 4.6)}$$

At these temperatures, the volatile SeO_2 is readily removed from the capillary via sublimation to result in a ZnO filled capillary (**Figure 4.15a**). Note that this reaction is not carried out in a micro-ampoule so that the SeO_2 can completely leave the capillary. The oxygen annealed material is porous with about 750 nm sized domains, a common morphology resulting from oxidation.[33] Powder XRD reveals that the remaining porous material is crystalline ZnO in the hexagonal phase. There is no indication of residual ZnSe, Se, SeO_2, or Zn (**Figure 4.15b**). The ZnO is crystalline, with A_1 transverse optical (TO), E_1(TO), E_2, and A_1 longitudinal optical (LO) phonon modes present in the Raman spectrum (**Figure 4.15c**). The HPCVD ZnSe microwires have low concentrations of impurities and should oxidize to ZnO with similarly low concentrations of impurities. Evidence of the purity of the ZnO microwires is observed in the efficient room temperature bandgap photoluminescence around 3.3 eV (**Figure 4.15d**). Further improvement in the materials quality of ZnO could lead to the development of room temperature exciton fiber lasers and piezoelectric tubes that can serve as valves for micro and nanofluidic applications.

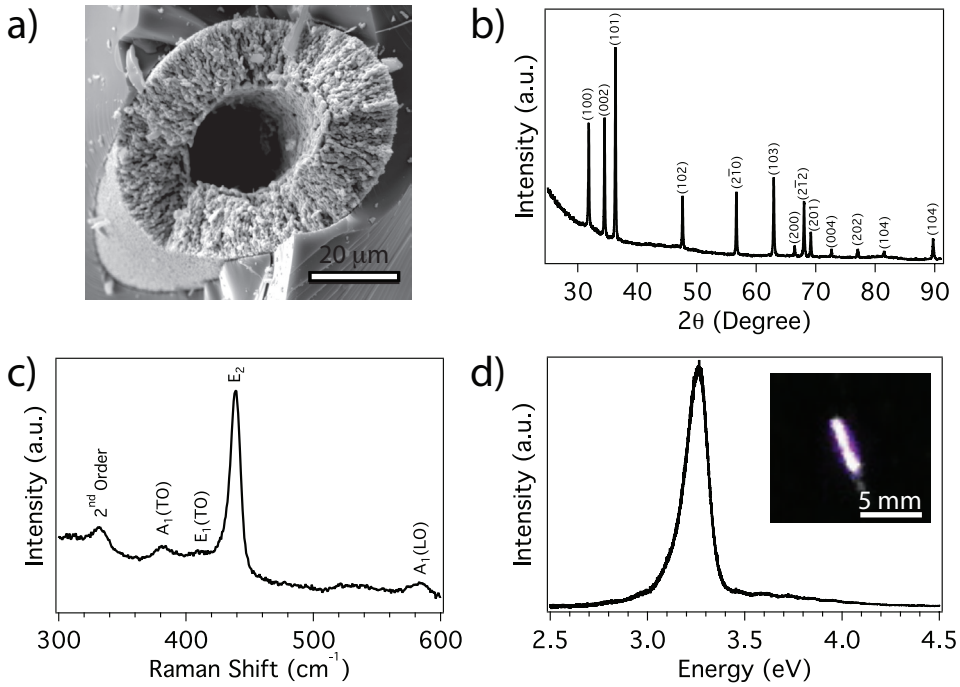

Figure 4.15: Oxidation of ZnSe to ZnO.[14] (a) SEM image of porous ZnO resulting from heating ZnSe in an oxygen atmosphere at 800 °C. (b) XRD reveals that the ZnO is in the hexagonal phase. (c) Raman spectroscopy with 488 nm excitation shows the characteristic phonon modes of ZnO. (d) Room temperature bandgap photoluminescence (244 nm laser excitation) is observed over the length of a 5 mm long, 50 µm diameter microwire (inset).

4.4.2 Reverse Water Gas Shift Reaction

The morphology of ZnO produced from the oxidation of ZnSe is not ideal for waveguide applications as the 725 nm domains will scatter light significantly. For this reason, it is desirable to develop encapsulation methods for the production of oxidizing species in the HPCVD regime. For example, a common way to deposit ZnO is to oxidize $(CH_3)_2Zn$ with H_2O, but there is considerable prereaction at room temperature between these two molecules. However, water can encapsulated and later produced at high pressure using a reaction known as the reverse water gas shift reaction:

$$CO_{2(g)} + H_{2(g)} \rightarrow H_2O_{(g)} + CO_{(g)} \qquad \textbf{(Reaction 4.7)}$$

The water that is produced can react with the Zn produced from Reaction 4.8 to deposit ZnO:

$(CH_3)_2Zn_{(g)} + H_{2(g)} \rightarrow Zn_{(g)} + 2CH_{4(g)}$ (**Reaction 4.8**)

$Zn_{(g)} + H_2O_{(g)} \rightarrow ZnO_{(s)} + H_{2(g)}$ (**Reaction 4.9**)

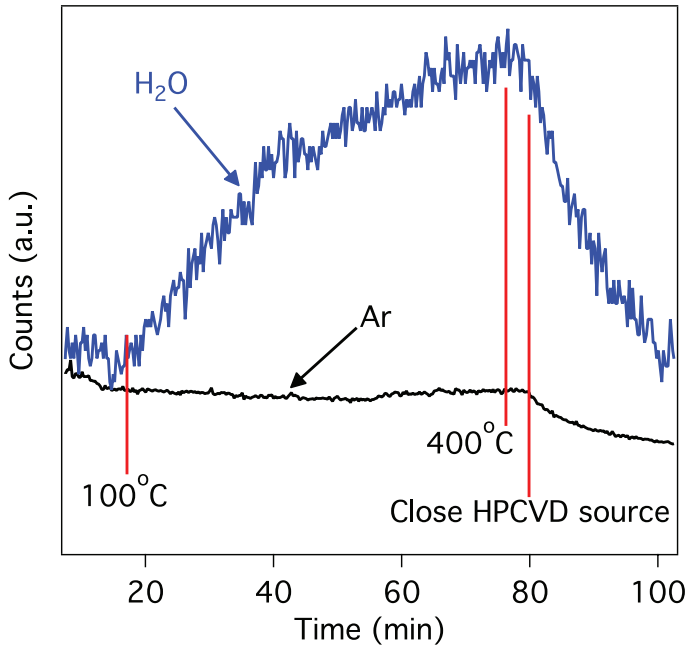

Figure 4.16: Formation of water at high pressure via the reverse water gas shift reaction. The water signal from the end of the capillary fed into a mass spectrometer increases as the HPCVD furnace is ramped from 100 °C to 400 °C over the course of one hour. When the HPCVD source is closed, the water signal decreases. A small argon pressure in the reservoir is used as a baseline.

At atmospheric pressure, the reverse water gas shift reaction typically occurs at temperatures of ~600 °C,[34] which is too high of a temperature for the $(CH_3)_2Zn$, which starts to produce Zn ~200 °C. However, as was mentioned in **Chapter 2**, the chemical potential of H_2 can be increased with pressure to make the molecule much more reactive, while the overall reaction rates can be increased due to the high number of molecular collisions. This is demonstrated in **Figure 4.16**, where the formation of water is observed at temperatures as low as 150 °C when the total reaction pressure is 35 MPa. In this experiment, the output flow from the capillary is fed into

a mass spectrometer (Hiden Analytical HPR-20QIC gas analyzer) to measure the water signal as a function of temperature of the heated capillary.

With the ability to produce water at low temperatures within the silica capillary, it then opens up many areas of oxidation chemistry via HPCVD encapsulation methods. A ZnO wire that was deposited using this reaction is shown in **Figure 4.17**. It is immediately obvious that the quality of this structure is superior to that described in **Section 4.4.1**. Thorough characterization of this material is needed as zinc acetate formation is also possible under these conditions,[35,36] although preliminary Raman spectra show evidence for ZnO. Further improvements in this chemistry will lead to the ability to deposit Al_2O_3, TiO_2, SiO_2, GeO_2, and many other oxides to exploit their properties in the optical fiber geometry. Jesse L. Bischof of the Badding group is already making progress in developing this chemistry further.

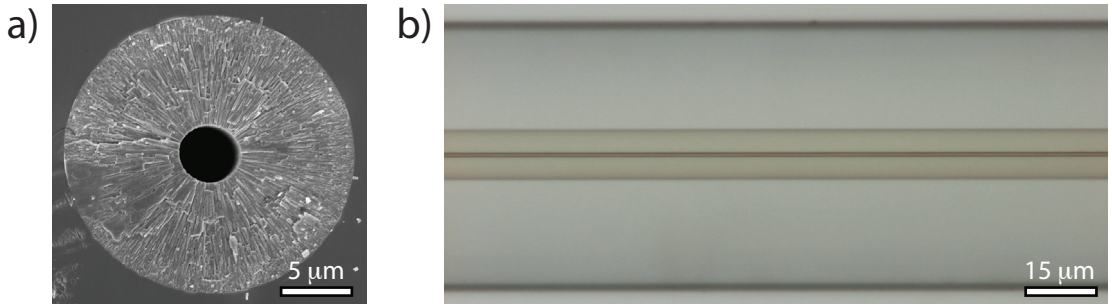

Figure 4.17: Deposition of ZnO using the reverse water gas shift reaction. (a) Cross-sectional SEM image of a ZnO filled capillary. (b) Optical micrograph of the transparent material. Image credit (a): Jesse L. Bischof.

4.5 Materials Characterization

In addition to surface roughness and geometric uniformity, materials quality is very important to waveguide optical loss and performance. For example, as a wide band gap semiconductor, pure ZnSe does not absorb infrared light by band-to-band transitions, but

impurities and defects that result in light scattering and absorption must be minimized. Although established CVD chemistries are known to deposit high quality ZnSe, the quality of material deposited by the HPCVD method needs to be assessed. Raman spectroscopy, photoluminescence, and optoelectronic measurements are established techniques for the characterization of impurities and defects in semiconductor materials.

4.5.1 Surface Characterization

The near atomically smooth (0.1 nm RMS roughness[37]) silica pore surfaces are coated with well-developed films from the "outside in". Thus it is important to assess whether the microwires and tubes formed in these pores have comparable outer surface roughness.[38] An array of 168 ZnSe wires 8 μm in diameter deposited in a silica template were removed by etching with HF (**Figure 4.18a**). The surface roughness was characterized by means of optical interference profilometry (Zemetrics ZeScope), which uses interference between two split beams in a microscope to allow the RMS roughness to be determined over areal dimensions of hundreds of square micrometers with sub-Ångstrom sensitivity. The ZnSe microwires etched out of their template have a RMS surface roughness of 0.1 nm (**Figure 4.18b**), comparable to the surface roughness of the template walls. The capillary templates have extraordinary diameter uniformity along their length as well, such that variations of only tens of nanometers in diameter over lengths of centimeters are possible.[39] Since the II-VI semiconductor microwires conform to the silica template walls, similar uniformity in diameter along their length can be expected.

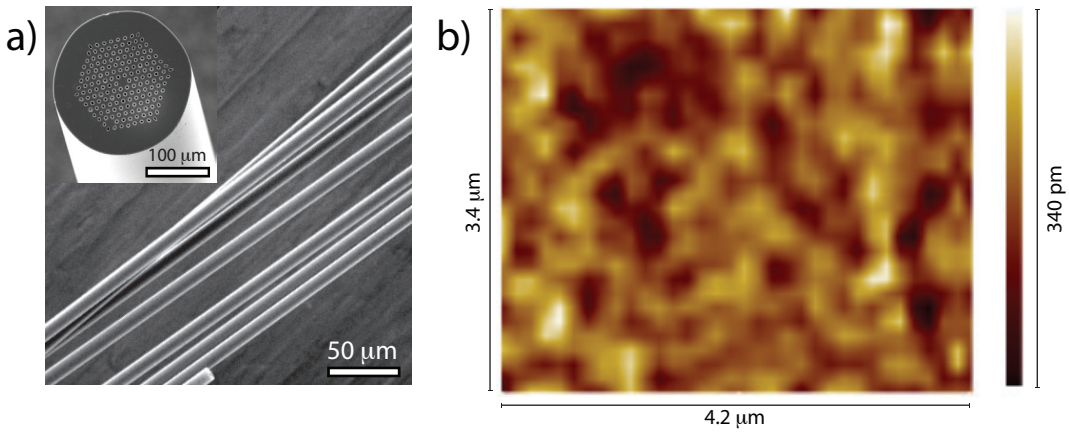

Figure 4.18: Surface roughness of ZnSe wires.[14] (a) SEM image of ZnSe wires removed from the silica MOF template (inset) (b) Optical interference profilometry measurement of 0.1 nm RMS surface roughness.

Since the deposition results in a wire, or more specifically a tube with a very small central void, it is then important to assess this inner surface roughness; especially because the annealing techniques that remove the void result in cracking, which limits current optical fiber characterizations to structures with the central hole. As mentioned earlier, the CH_4 byproduct results in a <400 nm diameter inner hole in the microwire. The roughness of this inner surface will thus be determined by the grain size and shape at this interface. The cross-sectional grain structure of the microwire was discussed earlier in **Section 4.3.1**. Changing the flow rate via the pressure can provide control of this inner surface grain size and thus the remaining pore size. Further optimization of the reaction chemistry should result in a smoother, smaller inner pore. Ultimately, as appropriate cladding glasses are developed to alleviate cracking, the central void will be removed to result in wires of high geometric perfection.

4.5.2 Raman Spectroscopy

The Raman spectrum (514 nm excitation, Renishaw inVia micro-Raman spectrometer) of the deposited ZnSe has peaks at 204.9 cm^{-1} and 251.2 cm^{-1} that arise from the TO and LO optical

phonons of ZnSe (**Figure 4.19a**). The Lorentzian components of their peak widths, 4.7 cm^{-1} (TO) and 6.1 cm^{-1} (LO) respectively, are comparable to the values of 4.1 cm^{-1} and 5.9 cm^{-1} obtained from an optical grade ZnSe reference (Alfa Aesar), indicating that the HPCVD ZnSe is highly crystalline. The symmetry of the LO peak is further evidence for the high crystallinity, as asymmetry can be caused by a high concentration of crystalline defects.[40] For the alloys, the Raman spectra (488 nm excitation, Dilor XY triple monochromator micro-Raman spectrometer) of the deposited materials are characteristic of $ZnS_xSe_{(1-x)}$, exhibiting TO_{ZnSe}, LO_{ZnSe}, and LO_{ZnS} phonon modes that shift continuously with x (**Figure 4.19b**).[41,42] Although the TO_{ZnS} phonon is present in pure ZnS (x=1) deposited by HPCVD, it is very weak in the $ZnS_xSe_{(1-x)}$ spectra, which is consistent with previous reports.[41] As the ZnS mole fraction is increased, the TO_{ZnSe} and LO_{ZnSe} modes shift towards each other, with the TO_{ZnSe} shifting up in frequency and the LO_{ZnSe} shifting down. The LO_{ZnS} mode shifts to lower frequency as the Se concentration increases. The asymmetric broadening observed with increasing Se concentration has been attributed to a disordering effect.[41]

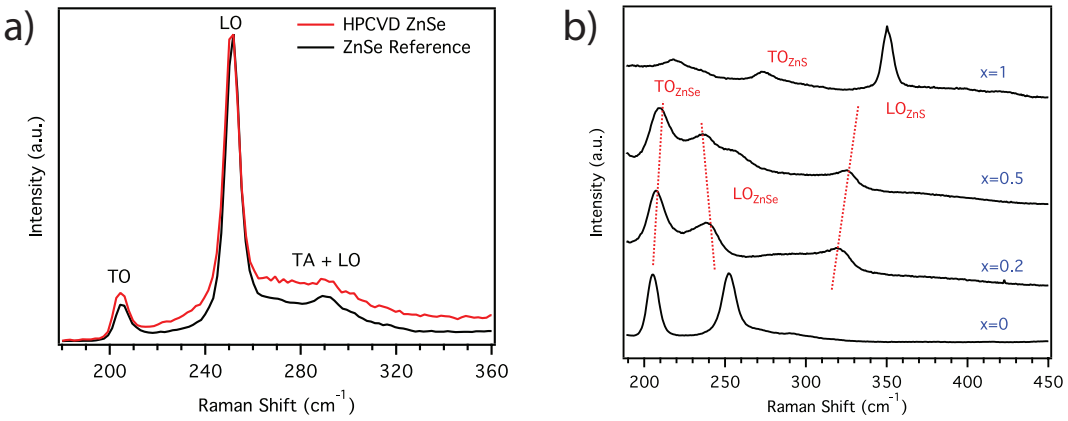

Figure 4.19: Raman spectroscopy of II-VI materials.[13,14] (a) Comparison of HPCVD ZnSe to a single crystal standard. (b) Continuous shifting of the phonon modes of $ZnS_xSe_{(1-x)}$ as a function of stoichiometry.

4.5.3 Band Edge Photoluminescence

The photoluminescence spectra of the ZnSe samples at 4.2 K have no discernible broad band emissions in the low energy region (~1.2 – 2.6 eV) that are typically associated with defects and impurities.[43] Near the band edge at about 2.8 eV (**Figure 4.20a**), exciton emissions are present, with the free exciton E_x at 2.801 eV and the donor bound exciton I_2 at 2.797 eV being the dominating peaks. The I_2 peak is generally attributed to the chlorine donor impurity introduced from alkyl precursors.[44] Other peaks of low intensity include the deep acceptor bound exciton I_1^d at 2.782 eV (generally attributed to Zn vacancies),[45] the broad donor-acceptor pair (DAP) emission peak at 2.73 eV (along with its LO phonon replica at 2.70 eV), and the dislocation bound exciton I_v^0 at 2.775 eV.[46] These defect bound excitons are frequently observed in high quality films deposited by means of conventional organometallic CVD,[8] and may be associated with the stacking faults that are observed in TEM. Temperature dependent photoluminescence shows that the band gap emission is visible up to room temperature (**Figure 4.20b**), implying that the HPCVD material has a low Se vacancy density, as Se vacancies are able to quench photoluminescence above 100 K.[47]

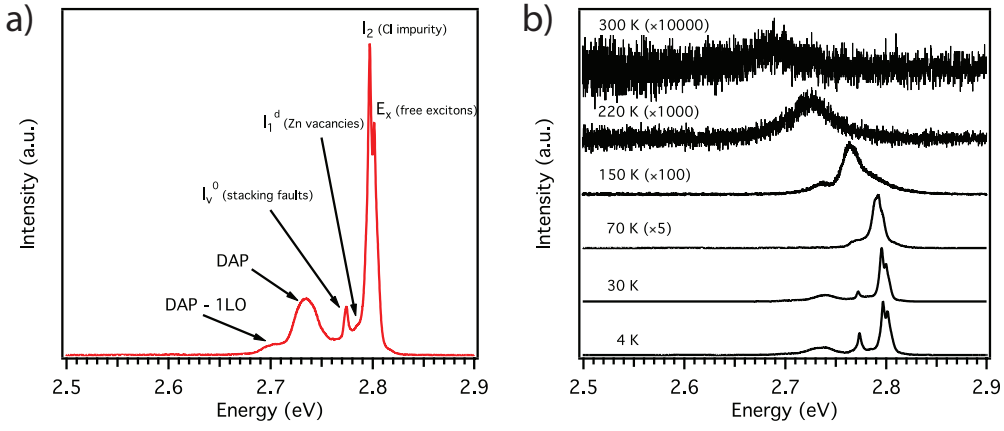

Figure 4.20: Band edge photoluminescence from ZnSe.[13] a) A low temperature (4.2 K) spectrum with peak assignments. b) Temperature dependent photoluminescence spectra showing band to band transitions up to room temperature. The spectra were collected with a Renishaw inVia micro-Raman spectrometer fitted with a liquid helium Janis cryostat at 364 nm excitation.

4.5.4 Photoresponse Characterization

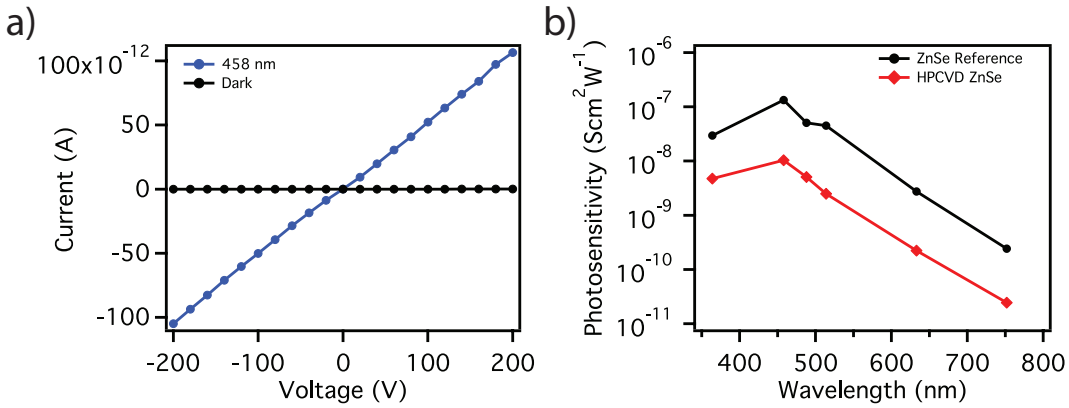

Figure 4.21: Photoresponse of ZnSe optical fibers.[13] (a) The current through a 50 μm diameter ZnSe wire increases dramatically under illumination with 458 nm light compared to dark. (b) Photosensitivity as a function of wavelength measured on a ZnSe wire and an optical grade reference wafer. The curves peak at approximately 458 nm, corresponding to the ZnSe bandgap. The photosensitivity at wavelengths longer than 458 nm originates from defect states in the bandgap; the rapid fall-off observed in the ZnSe wire is comparable to that in the optical grade reference and implies a low density of impurities and defects. The decrease in photosensitivity at shorter wavelengths (e.g. 364 nm) is due to an enhanced surface recombination process for carriers.

The dark electrical conductivity (Keithley 6430 source meter) at room temperature of the ZnSe wires etched out from silica and contacted with aluminum is less than 10^{-13} Scm^{-1}, implying that the chlorine donor impurity concentration observed in the low temperature photoluminescence is very low and that the free carriers are depleted by trapping states at the grain boundaries.[48] Upon illumination, the conductance increases dramatically (**Figure 4.21a**). This photoresponse is characterized by the photosensitivity:

$$S = \frac{Pl}{Gw} \qquad \textbf{(Equation 4.1)}$$

where P is the power density of incident light, G is the conductance, l and w are the length and width of the wire respectively. This value varies from 10^{-8} to 10^{-7} Scm^2W^{-1} at the wavelength of 458 nm for the deposited ZnSe wires, comparable to the value of 1×10^{-7} Scm^2W^{-1} obtained from

the optical grade reference (**Figure 4.21b**). The photosensitivity is proportional to the mobility-lifetime product.[49] Thus the similarity of the photosensitivity of the deposited material to that of the optical grade reference indicates that the mobility-lifetime product is high, consistent with the low density of impurities and defects revealed by the photoluminescence measurements.

4.6 Applying HPCVD to II-VI Semiconductor Optical Fiber Fabrication

The reaction chemistries and principles presented in this chapter can be extended to II-VI materials containing Cd, Hg, and Te, the quaternary alloys, and to other families of materials such as III-V semiconductors. Furthermore, in view of their excellent materials quality and smooth exterior surfaces, the II-VI semiconductor filled capillaries should function well as low loss waveguides. In the next chapter, the optical properties of these structures will be investigated and their performance as optical fibers will be assessed. Structuring capabilities in the transverse plane (shown in **Chapter 3**) as well as layering techniques will be applied to II-VI semiconductors. As was discussed earlier, the central void will be present in all of the optical fibers due to the thermal expansion mismatch issues with the void-free filling techniques.

4.7 References

[1] M. Afzaal, D. Crouch, M. A. Malik, M. Motevalli, P. O'Brien, J. Park, and J. D. Woollins, "Deposition of II-VI Thin Films by LP-MOCVD Using Novel Single-Source Precursors" *Eur. J. Inorg. Chem.* **2004**, 171.

[2] M. Afzaal, S. M. Aucott, D. Crouch, P. O'Brien, J. D. Woollins, and J. Park, "Deposition of MSe (M = Cd, Zn) Films by LP-MOCVD from Novel Single-Source Precursors $M[(SePPh_2)_2N]_2$" *Chem. Vap. Deposition* **2002**, 8, 187.

[3] M. Chunggaze, J. McAleese, P. O'Brien, and D. J. Otway, "Deposition of Thin Films of CdSe or ZnSe by MOCVD Using Simple Air Stable Precursors" *Chem. Comm.* **1998**, 833.

[4] D. Cupertino, D. J. Birdsall, A. M. Z. Slawin, and J. D. Woollins, "The Preparation and Coordination Chemistry of $^{i}Pr_2P(E)NHP(E')^{i}Pr_2$ (E, E'=Se; E=Se, E'=S; E=S, E'=O; E,E'=O" *Inorg. Chim. Acta* **1999**, 290, 1.

[5] F. T. Wang, J. Najdzionek, K. L. Leneker, H. Wasserman, and D. M. Braitsch, "A Facile Synthesis of Imidotetraphenyldiphosphinic Acids" *Synth. React. Inorg. Met.-Org. Chem.* **1978**, 8, 119.

[6] T. Kamins, "*Polycrystalline Silicon for Integrated Circuits and Displays*" Kluwer Academic Publishers, **1998**.

[7] H. Ando, H. Inuzuka, M. Konagai, and K. Takahashi, "Photoenhanced Metalorganic Chemical Vapor Deposition of ZnSe Films Using Diethylzinc and Dimethylselenide" *J. Appl. Phys.* **1985**, 58, 802.

[8] T. Yokogawa, M. Ogura, and T. Kajiwara, "High Quality ZnSe Films Grown by Low Pressure Metalorganic Vapor Phase Epitaxy Using Methylalkyls" *Appl. Phys. Lett.* **1987**, 50, 1065.

[9] M. Afzaal, M. A. Malik, and P. O'Brien, "Preparation of Zinc Containing Materials" *New J. Chem.* **2007**, 31, 2029.

[10] W. Kuhn, A. Naumov, H. Stanzl, S. Bauer, K. Wolf, H. P. Wagner, W. Gebhardt, U. W. Pohl, A. Krost, W. Richter, U. Dumichen, and K. H. Thiele, "Low Temperature MOVPE Growth of ZnSe with Ditertiarybutylselenide" *J. Cryst. Growth* **1992**, 123, 605.

[11] G. B. Stringfellow, "*Organometallic Vapor-phase Epitaxy: Theory and Practice*" Academic Press, **1999**.

[12] H. Mitsuhashi, I. Mitsuishi, and H. Kukimoto, "Growth Kinetics in the MOVPE of ZnSe on GaAs Using Zinc and Selenium Alkyls" *J. Cryst. Growth* **1986**, 77, 219.

[13] J. R. Sparks, R. He, N. Healy, M. Krishnamurthi, A. C. Peacock, P. J. A. Sazio, V. Gopalan, and J. V. Badding, "Zinc Selenide Optical Fibers" *Adv. Mater.* **2011**, 23, 1647.

[14] J. R. Sparks, R. He, N. Healy, S. Chaudhuri, T. C. Fitzgibbons, A. C. Peacock, P. J. A. Sazio, and J. V. Badding, "Conformal Coating by High Pressure Chemical Deposition for Patterned Microwires of II-VI Semiconductors" *Adv. Funct. Mater.* **2012**, DOI: 10.1002/adfm.201202224.

[15] N. Maung, G. H. Fan, T. L. Ng, J. O. Williams, and A. C. Wright, "Mass-Spectrometric Study of the Pyrolysis Reactions in the MOVPE of Ga_2Se_3 by in-situ Gas Sampling" *J. Cryst. Growth* **1996**, 158, 68.

[16] H. Xu, Y. Liang, Z. Liu, X. Zhang, and S. Hark, "Synthesis and Optical Properties of Tetrapod-like ZnSSe Alloy Nanostructures" *Adv. Mater.* **2008**, 20, 3294.

[17] H. Kato and I. Kikuma, "Effect of Seed Annealing on ZnSe Single-Crystals Grown by Vertical Sublimation Method" *J. Cryst. Growth* **2000**, 212, 92.

[18] H. Schafer, "*Chemical Transport Reactions*" Academic Press, **1964**.

[19] C. Su, W. Palosz, S. Feth, and S. L. Lehoczky, "Heat Treatments of ZnSe Starting Materials for Physical Vapor Transport" *J. Cryst. Growth* **1998**, 192, 386.

[20] N. Yao, "*Focused Ion Beam Systems: Basics and Applications*" Cambridge University Press, **2007**.

[21] T. Matsumoto and T. Ishida, "Chemical Vapor Deposition of Zinc Chalcogenides Using Elemental Source Materials" *J. Cryst. Growth* **1984**, 67, 135.

[22] P. Rudolph, N. Schafer, and T. Fukuda, "Crystal Growth of ZnSe from the Melt" *Mat. Sci. Eng.* **1995**, R15, 85.

[23] J. R. Cutter, G. J. Russell, and J. Woods "The Growth and Defect Structure of Single Crystals of Zinc Selenide and Zinc Sulpho-Selenide" *J. Cryst. Growth* **1976**, 32, 179.

[24] E. Schonherr, M. Freiberg, and H. Hartmann, "Preferred [111] Growth of ZnSe Crystals from the Vapor Due to Repeated Twinning" *J. Cryst. Growth* **1997**, 179, 423.

[25] C.H. Su, S. Feth, and S. L. Lehoczky, "Thermal Expansion Coefficient of ZnSe Crystal Between 17 and 1080 °C by Interferometry" *Mater. Lett*. **2009**, 63, 1475.

[26] J. J. Kaufman, G. Tao, S. Shabahang, E.H. Banaei, D. S. Deng, X. Liang, S. G. Johnson, Y. Fink, and A. F. Abouraddy, "Structured Spheres Generated by an In-Fibre Fluid Instability" *Nature* **2012**, 487, 463.

[27] Y. Y. Huang, A. Sarkar, and P. C. Schultz, "Relationship Between Composition, Density, and Refractive Index for Germania Silica Glasses" *J. Non-Cryst. Solids* **1978**, 27, 29.

[28] J. Kobelke, K. Schuster, D. Litzkendorf, A. Schwuchow, J. Kirchhof, V. Tombelaine, H. Bartelt, P. Leproux, V. Couderc, A. Labruyere, and R. Jamier, "Highly Germanium and Lanthanum Modified Silica Based Glasses in Microstructured Optical Fibers for Non-Linear Applications" *Opt. Mater.* **2010**, 32, 1002.

[29] E. M. Dianov and V. M. Mashinsky, "Germania-Based Core Optical Fibers" *J. Lightw. Technol.* **2005**, 23, 3500.

[30] S. Morris, T. Hawkins, P. Foy, J. Ballato S. W. Martin, and R. Rice, "Cladding Glass Development for Semiconductor Core Optical Fibers" *Int. J. Appl. Glass Sci.* **2012**, 3, 144.

[31] U. Ozgur, Y. I. Alivov, C. Liu, A. Teke, M. A. Reshchikov, S. Dogan, V. Avrutin, S. J. Cho, and H. Morkoc, "A Comprehensive Review of ZnO Materials and Devices" *J. Appl. Phys.* **2005**, 98, 041301.

[32] O. Maksimov, "Oxidative Annealing of ZnSe/GaAs Heterostructures" *Mater. Lett.* **2008**, 62, 3969.

[33] V. V. Ursaki, V. V. Zalamai, A. Burlacu, C. Klingshirn, E. Monaico, and I. M. Tiginyanu, "Random Lasing in Nanostructured ZnO Produced from Bulk ZnSe" *Semicond. Sci. Technol.* **2009**, 24, 085017.

[34] F. Bustamante, R. M. Enick, A. Cugini, R. P. Killmeyer, B. H. Howard, K. S. Rothenberger, M. V. Ciocco, B. D. Morreale, S. Chattopadhyay, and S. Shi, "High-Temperature Kinetics of the Homogeneous Reverse Water–gas Shift Reaction" *AIChE J.* **2004**, 50, 1028.

[35] Z. Z. Zhi, Y. C. Liu, B. S. Li, X. T. Zhang, Y. M. Lu, D. Z. Shen, and X. W. Fan, "Effects of Thermal Annealing on ZnO Films Grown by Plasma Enhanced Chemical Vapour Deposition from $Zn(C_2H_5)_2$ and CO_2 Gas Mixtures" *J. Phys. D.: Appl. Phys.* **2003**, 36, 719.

[36] S. Jain, T. T. Kodas, and M. Hampden-Smith, "Synthesis of ZnO Thin Films by Metal-Organic CVD of $Zn(CH_3COO)_2$" *Chem. Vap. Deposition* **1998**, 4, 51.

[37] P. J. Roberts, F. Couny, H. Sabert, B. J. Mangan, D. P. Williams, L. Farr, M. W. Mason, A. Tomlinson, T. A. Birks, J. C. Knight, and P. St. J. Russell, "Ultimate Low Loss of Hollow-Core Photonic Crystal Fibres" *Opt. Express* **2005**, 13, 236.

[38] N. Healy, L. Lagonigro, J. R. Sparks, S. Boden, P. J. A. Sazio, J. V. Badding, and A. C. Peacock, "Polycrystalline Silicon Optical Fibers with Atomically Smooth Surfaces" *Opt. Lett.* **2011**, 36, 2480.

[39] "*Internal Diameter Measurement of Small Bore Capillary Tubing*" http://www.polymicro.com/tech/applicationnotes/appnote_2003JUN.htm (July **2012**)

[40] T. Ganguli and A. Ingale, "Raman and Photoluminescence Investigations of Disorder in ZnSe Films Deposited on n-GaAs" *Phys. Rev. B* **1999**, 60, 11618.

[41] O. Brafman, I. F. Chang, G. Lengyel, S. S. Mitra, and E. Carnall, "Optical Phonons in ZnS_xSe_{1-x} Mixed Crystals" *Phys. Rev. Lett.* **1967**, 19, 1120.

[42] E. A. Vinogradov, B. N. Mavrin, N. N. Novikova, and V. A. Yakovlev, "Mode Dispersion in the Optical-Phonon Spectra of Mixed Crystals $ZnS_{1-x}Se_x$" *Phys. Solid State* **2006**, 48, 1940.

[43] R. N. Bhargava, "The Role of Impurities in Refined ZnSe and Other II-VI Semiconductors" *J. Cryst. Growth* **1982**, 59, 15.

[44] A. Schneider, K. P. Geyzers, F. E. G. Guimaraes, and M. Heuken, "Photoluminescence Spectroscopy as a Tool to Assess Extrinsic Impurities and Quality of ZnSe and ZnS_xSe_{1-x} Grown by MOVPE" *Adv. Mater. Opt. Electron.* **1994**, 3, 261.

[45] H. Cheng, S. K. Mohapatra, J. E. Potts, and T. L. Smith, "Effects of Beam Pressure Ratios on Film Quality in MBE Growth of ZnSe" *J. Cryst. Growth* **1987**, 81, 512.

[46] K. Shahzad, J. Petruzzello, D. L. Olego, D.A. Cammack, and J. M. Gaines, "Correlation Between Radiative Transitions and Structural Defects in Zinc Selenide Epitaxial Layers" *Appl. Phys. Lett.* **1990**, 57, 2452.

[47] K. Yoshino, Y. Matsushima, S. Tiong-Palisoc, K. Ohmori, and M. Hiramatsu, "Temperature Dependence of Luminescence in ZnSe" *Mater. Sci. Eng.* **1995**, B35, 68.

[48] G. I. Rusu, M. E. Popa, G. G. Rusu, and I. Salaoru, "On the Electronic Transport Properties of Polycrystalline ZnSe Films" *Appl. Surf. Sci.* **2003**, 218, 222.

[49] R. A Street, "*Hydrogenated Amorphous Silicon*" Cambridge University Press, **1991**.

Chapter 5

II-VI Semiconductor Optical Fibers

After depositing high refractive index II-VI semiconductors within low refractive index silica capillaries, the structures naturally form simple step index cylindrical waveguides. In view of their excellent materials quality and smooth exterior surfaces discussed in **Chapter 4**, the structures function well as low loss optical fibers. In this chapter, II-VI semiconductor optical fiber structures and their properties are discussed. Having control over the waveguiding properties of the optical fibers is paramount to optical fiber laser performance.

5.1 Step Index II-VI Semiconductor Optical Fibers

5.1.1 Wavelength Dependent Loss

Measurements of the transmission loss over the wavelength range of 0.500 – 10.6 μm of ZnSe optical fibers fabricated to have core diameters of 15 μm and 50 μm confirm the expectation of low loss (**Figure 5.1**). In both cases the losses decrease with increasing wavelength and become as low as 0.5−0.9 dB/cm in the 2000 – 2400 nm mid-IR region. The loss α as a function of the wavelength can be fitted from 540 – 2400 nm to a power law with an exponent of -3.9±0.2. This functional dependence is well matched to the λ^{-4} dependence characteristic of Rayleigh scattering, suggesting that scattering from bulk refractive index inhomogeneities (possibly due to grain boundaries) in the material is the dominant loss mechanism. Thus despite the presence of the central ~400 nm pore, surface scattering[1] does not appear to be the dominant loss mechanism. As discussed in **Chapter 1**, the intrinsic loss of ZnSe over its transparency range

is very low; thus further engineering of the grain size by optimization of the deposition conditions or thermal or laser annealing may allow for even lower waveguide losses.

At longer wavelengths, the silica cladding begins to influence the loss of the optical fiber due to silica's narrow transmission window compared to ZnSe (**Table 1.1**). Silica begins to absorb in the mid-IR at 3 μm and is very strongly absorbing at 10.6 μm. Since part of the mode of the optical fiber interacts with the silica cladding, there is associated absorption. This can be seen in **Figure 5.1**, where the loss of the 50 μm core deviates from the $\lambda^{-3.9}$ fit due to the introduction of the absorptive loss mechanism. To reduce the influence of the silica, a larger core fiber or IR transparent cladding layers are needed, which are discussed in **Section 5.2.1**.

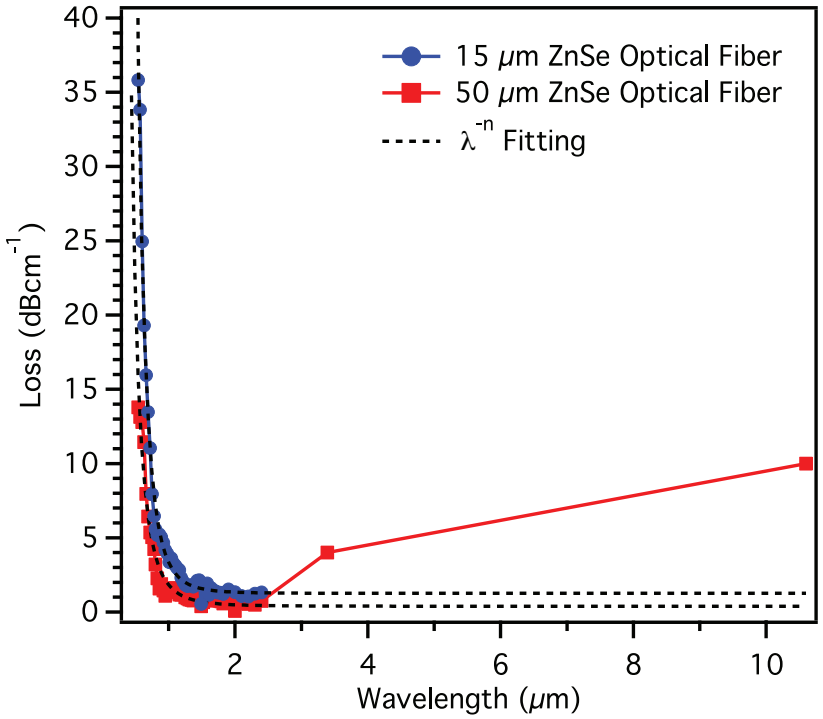

Figure 5.1: Wavelength dependent loss in ZnSe optical fibers. Optical loss of 50 μm (square/red) and 15 μm (circle/blue) diameter ZnSe core optical fibers as a function of wavelength. Dashed lines are fit to a $\lambda^{-3.9}$ dependence.

In contrast, ZnS optical fibers have a higher loss of 16 dB/cm at 1550 nm, while $ZnS_{0.2}Se_{0.8}$ optical fibers have a loss of 7 dB/cm. As the ZnS and $ZnS_xSe_{(1-x)}$ materials have

comparable surface quality and crystallinity to ZnSe, it is likely that the larger losses measured in these materials can be attributed to impurity related absorption due to use of lower purity $(CH_3)_2S$; the $(CH_3)_2S$ was 99% pure versus electronic grade for $(CH_3)_2Se$ and $(CH_3)_2Zn$. When light is waveguided over centimeter distances, the presence of even small quantities of impurities can have an adverse effect on optical loss. With further development of precursor chemistry to reduce impurity levels, the optical losses in the sulfur-based materials should approach the loss values that have already been demonstrated for ZnSe optical fibers.

5.1.2 Comparison to Planar Waveguides

The loss in the ZnSe optical fibers is very low with respect to semiconductor waveguides; in fact, the fibers are among the lowest loss semiconductor optical fibers fabricated to date.[2] In general, a semiconductor waveguide with a loss < 1 dB/cm is considered useful for photonic applications. There have not been many reports on planar ZnSe waveguides, which were initially investigated for modulation, nonlinearity, and electro-optic applications in the visible range.[3,4] These structures have not been thoroughly investigated in the mid-IR, but have reported losses of 17 dB/cm and 1550 nm,[5] 9 dB/cm at 1047 nm,[6] and 3 – 40 dB/cm in the visible range.[7-13] Recently a 10 μm Cr^{2+}:ZnSe planar waveguide has been fabricated (for laser power scaling advantages of waveguides) which does not have a reported loss, but does have quite a high surface roughness (7 nm RMS)[14] compared to that of the HPCVD structures presented in **Chapter 4**. This waveguide could not demonstrate continuous wave (CW) lasing, which implies high losses in the mid-IR. The losses of the ZnSe optical fibers presented in this chapter can thus be considered "low-loss" and in general have losses low enough for a variety of device demonstrations such as nonlinear optics (**Section 5.3**) and fiber lasers (**Chapter 6**).

5.1.3 Power Handling

An important aspect of an optical fiber, or any optical material, is the power density that can be coupled into the core for high power applications. As the goal of this dissertation is to develop high power optical fiber lasers, it is important to assess the power handling capabilities of the fabricated fibers. An important note is that the quality of the optical polish on the facet is very important to in determining the damage threshold; especially in relation with the small hole remaining in the fiber core. Debris from polishing processes can infiltrate into the central void and be a source for a "hot spot" that can result in heating and destruction of the sample. Therefore, once a thermal expansion matched glass is used in conjunction with the annealing techniques that remove the central void, it can be expected that the power handling capability of the structures will increase beyond those presented below.

In the continuous wave regime, where heating plays the major role in the damage mechanism, 10 W of 1.9 μm light has been coupled into a 15 μm core ZnSe optical fiber. Thus, the resulting power density is ~ 5.6 MW/cm^2. However, the available power in the CW range limited the determination of the damage threshold of the sample, which could be orders of magnitude higher. In the pulsed regime, where nonlinear absorption plays the major role in the damage mechanism, 3.5 kW peak power at 1.0 μm has been coupled into a 10 μm core before the core is damaged, which results in a damage threshold of 4.5 GW/cm^2.

The HPCVD process has thus fabricated some of the highest power handling fiber optics in the mid-IR to date, owing to the ability to fabricate optical fibers from materials that are very refractory and cannot be drawn. To compare to the competitive fiber optic platforms in the mid-IR: chalcogenides have very low power handling capabilities on the order of 10 – 20 kW/cm^2,[15] while hollow core Omniguide fibers have power handling levels in the 6.5 kW/cm^2 range.[16] Thus, the ZnSe optical fibers can be considered a new high power IR fiber optic platform with

orders of magnitude higher damage thresholds than current technologies, which will be very useful for power scaling Cr^{2+}:ZnSe lasers.

5.1.4 Large Core Optical Fibers

To additionally increase the power handling capabilities, the size of the core can be increased to guide high powers of light at low overall power densities. The ability to deliver high power mid-IR light with optical fibers is useful for a variety of industrial applications as well as sensing and infrared countermeasures. However, as was mentioned in **Chapter 4**, the thermal expansion mismatch between silica and ZnSe becomes more of an issue as the size of the core increases. This is because the ZnSe is more susceptible to cracking under the stress that the low expansion silica adds to the material as the ZnSe wire diameter is increased. Overall, this limits the core size to be 50 μm or less when using silica as the capillary template, which results in a few cracks along the length that can be screened out.

In order to fabricate larger core optical fibers, a new glass is needed that has a thermal expansion coefficient near that of ZnSe (~5×10^{-6} K^{-1}). A good candidate to start with is an aluminosilicate glass. Schott 8253 has a linear expansion coefficient of 4.7×10^{-6} K^{-1} and is readily available in high purity tubes that can be drawn with conventional fiber drawing techniques. This glass was purchased and drawn into micro-capillaries at the University of Southampton, UK by Pier J. A. Sazio. Many different sizes can be drawn by varying the process parameters; for these experiments, a 150 μm and 15 μm internal diameter capillary were used. The flow rate through a 150 μm capillary would be far too high for HPCVD, which would result in emptying the HPCVD source in a matter of seconds. Also, the flow would be in the turbulent regime (**Figure 2.3**), which would affect precursor transport to the capillary walls. To control the flow to be laminar, a 2 cm long, 15 μm section was spliced on to the end of the 150 μm capillary

(similar to **Figure 4.12**) to reduce the flow rate. The resulting deposition is shown in **Figure 5.2**, where a 150 μm core that is completely crack-free has been fabricated. Although this glass works well to alleviate cracking during the ~ 450 °C temperatures of the HPCVD process, it does not have high enough glass transition temperature for the annealing methods presented in **Chapter 4**. Depending on the size of the structure and surface quality, the power handling can scale either linearly (diameter) or with the square (area) of the spot size.[17,18] The continuous wave power that this fiber should be able to deliver can be calculated using the damage thresholds from the previous section: 4000 W (scaled by area) or 100 W (scaled by diameter). There was not a laser source readily available to test this power handling calculation and determine which scaling factor is appropriate for the ZnSe optical fibers.

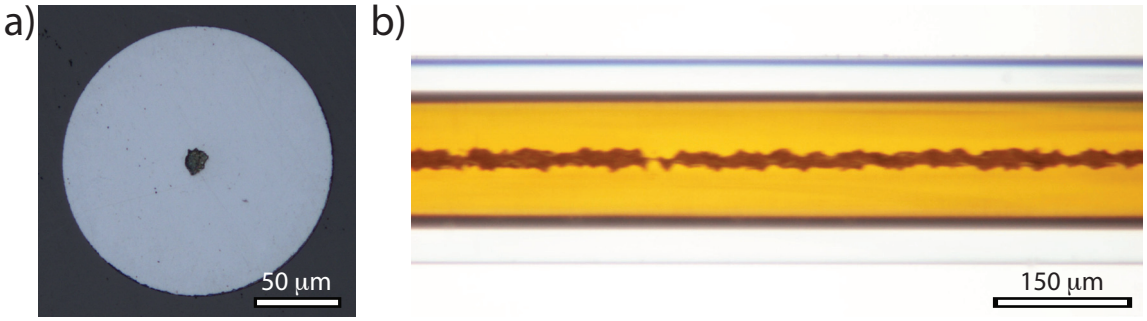

Figure 5.2: Large core ZnSe optical fibers. Schott 8253 glass capillaries are thermal expansion matched to ZnSe, which allows for large core, crack free optical fibers to be fabricated. The polished facet (a) and diascopically illuminated optical micrograph from the side (b) of a 150 μm core ZnSe optical fiber show no signs of cracking.

5.1.5 Mode Structure

A mode of a waveguide is a solution to Maxwell's equations for an electromagnetic wave confined with boundary conditions, which results in a certain distribution of the light in the cross-section of the waveguide. From a chemist's perspective, a mode is conceptually similar to atomic orbitals for an electron, which are the states available to an electron when bound on an atom.

Instead of having different energy, the states that the photon bound in a waveguide can be in (modes) each have a different propagation constant, or speed through the fiber. From a ray trace point of view, high order modes tend to have higher incident angles in the total internal reflection model. For a rigorous discussion of optical fiber modes see [19]. For a step index cylindrical waveguide, the number of modes that the fiber supports is given by the follow equation:[20]

$$M \approx \frac{4}{\pi^2} V^2 \qquad \textbf{(Equation 5.1)}$$

$$V = 2\pi \frac{a}{\lambda_0} \sqrt{n_{core}^2 - n_{cladding}^2} \qquad \textbf{(Equation 5.2)}$$

where a is the core radius, n is the refractive index, and λ_0 is the vacuum wavelength. The $\sqrt{n_{core}^2 - n_{cladding}^2}$ term is also referred to as the NA of the fiber, which is related to the acceptance cone of the waveguide. The number of allowable modes can also be calculated with finite element modeling, which provides a more accurate result for high index contrast systems such as semiconductor optical fibers. At 1550 nm wavelength, a 10 μm diameter ZnSe optical fiber supports ~670 modes, while a 15 μm core supports ~790 modes. Such multimode waveguides are not desirable for many applications. For example, for a fiber laser, it is ideal to have the mode of the pump wavelength overlap as much as possible with the mode of the lasing wavelength. This can be achieved using low mode number optical fibers, with both wavelengths in the fundamental (lowest order) mode of the waveguide at their respective wavelengths. Another example is modal dispersion of a high energy pulse such as those in the second harmonic experiments in **Section 5.3**. Different modes travel at different speeds through a fiber, which results in a spreading of the optical pulse in time in a multimoded waveguide and an over reduction in the peak optical power, which is not ideal for nonlinear processes.

For highly multimode optical fibers, the output is a superposition of all the modes that can be excited or cross-coupled to and results in the mode structure shown in **Figure 5.3**. This intensity profile of 1550 nm light at the output of a 15 μm diameter ZnSe optical fiber is characteristic of multimode behavior, where the central dip in the intensity is due to the small 400 nm diameter central pore. Individual modes cannot be isolated.

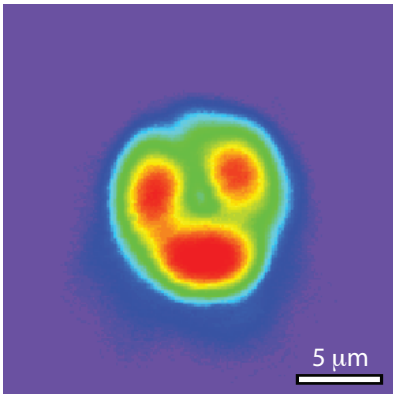

Figure 5.3: Multimode nature of step index ZnSe optical fibers. The output of a simple step index ZnSe optical fiber with silica cladding is a superposition of many modes.

5.2 Microstructured II-VI Semiconductor Optical Fibers

In general, high refractive index semiconductor (n=2.45 for ZnSe at 1550 nm) waveguides with either silica (n=1.44) or air (n=1) cladding have a large index contrast and thus are highly multimode. Realizing micrometer sized semiconductor waveguides with more desirable low order mode or single mode behavior is still an ongoing challenge in photonics that requires proper refractive index grading (see **Section 3.3.1**). For single mode operation at 2400 nm, a ZnSe optical fiber would need to have an overall core diameter less than 930 nm. However, such a small core would have limited power handling ability for fiber laser applications. Thus it is important to control the refractive index profile in the transverse plane of the waveguide to reduce

the NA and allow for low-mode operation at larger core diameters. This has been accomplished in a two ways: chemical composition and microstructured templates.

5.2.1 Mode Structure Control with $ZnS_xSe_{(1-x)}$ Layers

The chemical synthesis approach to reduce the index contrast is to deposit a layer of $ZnS_xSe_{(1-x)}$ first, followed by filling in the structure with ZnSe. Since ZnS has a lower refractive index (n=2.27 at 1550 nm) compared to ZnSe (n=2.45 at 1550 nm), doping a small atomic percent of S in ZnSe results in a slight reduction in the refractive index. This allows for low index contrast core/cladding waveguides to be fabricated, which drastically decreases the number of modes supported by the waveguide and will lead to single mode operation, improved beam quality, and more controllable mode overlap between the pump and signal for laser and nonlinear applications. Owing to its optical transparency in the IR, $ZnS_xSe_{(1-x)}$ also serves to alleviate the influence that silica absorption has on the output spectrum in the mid-IR that was seen for wavelengths above 3 μm for silica cladded ZnSe fibers (**Figure 5.1**). Core/shell structures using $ZnS_{0.2}Se_{0.8}$ as a cladding material have been fabricated. At these low (x=0.2) levels, sulfur incorporation into ZnSe lowers the refractive index of the material by about 0.01,[21,22] producing a low NA, IR transparent optical fiber with much more control over mode structure. The effects of a 1 μm and 5 μm $ZnS_{0.2}Se_{0.8}$ layer in a 15 μm and 30 μm capillaries, respectively that are then filled with ZnSe are shown in **Figure 5.4** at 1550 nm wavelength. It can be seen that low order modes can readily be excited and isolated in this fiber that agree well with the solved modes using finite element calculations. For comparison to the silica clad ZnSe optical fibers, these $ZnS_{0.2}Se_{0.8}$ clad fibers support tens of modes, depending on the ZnSe core size.

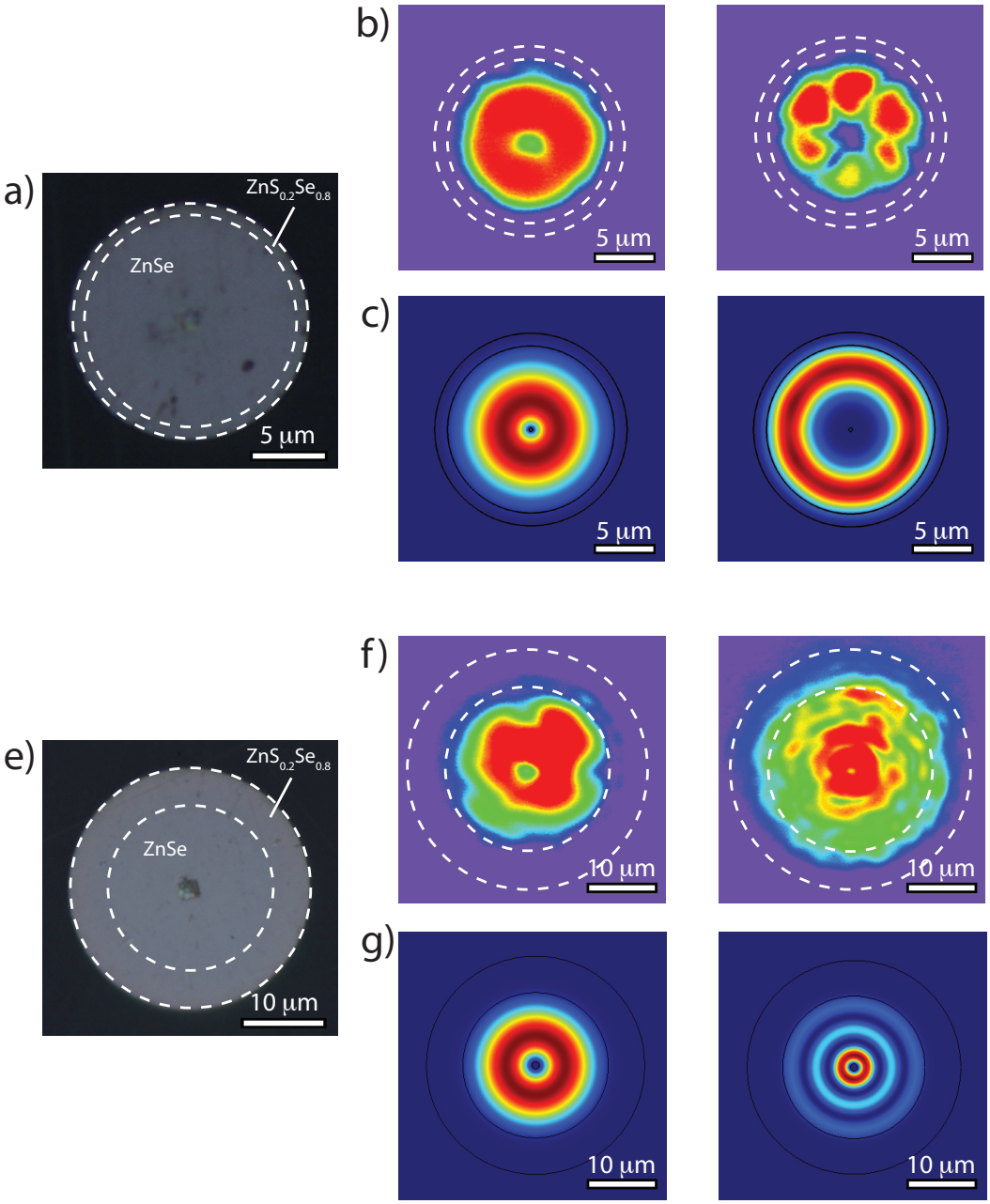

Figure 5.4: Mode structure control with $ZnS_xSe_{(1-x)}$ layers. (a) A 1 μm $ZnS_{0.2}Se_{0.8}$ cladding / 13 μm ZnSe core optical fiber allows for low order modes to be isolated experimentally (b), which agree well with finite element modeling simulations (c). (e) Larger core fibers (5 μm $ZnS_{0.2}Se_{0.8}$ cladding / 20 μm ZnSe core) allow for more effective isolation of mid-IR light from the silica cladding, while still having a low NA. Although the larger core size results in more modes than (a), individual modes can be isolated (f) that agree well with modeling (g).

A major challenge in developing the cladding layer chemistry is the need to have a uniform stoichiometry (and thus refractive index) of the cladding over the length of the fiber. Any variations of the stoichiometry will lead to differing modal properties along the length, which will result in cross-coupling between modes and increased loss. Because of these issues, the fibers shown in **Figure 5.4** are limited to millimeter length scales, where the stoichiometry is uniform. This non-uniformity in the cladding arises from the different rate constants of the $(CH_3)_2S$ and $(CH_3)_2Se$ reactions with H_2 in the deposition of $ZnS_xSe_{(1-x)}$ that lead to different stoichiometries at both different temperatures and different ratios of precursor. To eliminate these effects and just have one variable to tune in the deposition, one could employ the $(iPr)_2S$ molecule as a sulfur source that will have a weaker bond compared to $(CH_3)_2S$ and allow for the reaction rates for the production of H_2S an H_2Se production to be similar at a given temperature. Therefore, the stoichiometry of the deposited material could be controlled mainly by the ratio of the source molecules and allow for more uniform stoichiometry over the length of the fiber.

5.2.2 Large Mode Area ZnSe Optical Fibers

As previously mentioned, a key advantage of HPCVD in MOFs is the ability to deposit materials in complex 2D geometries to modify the guiding properties of light in the semiconductor wires. In particular, the structure shown in **Figure 5.5a** is the first demonstration of a ZnSe MOF, similar to the silicon MOF that was characterized in **Chapter 3**. The fiber was fabricated by filling the air holes of a hollow core silica photonic bandgap fiber with ZnSe via HPCVD. The resulting structure has a 9 μm ZnSe core with a cladding of 3 μm ZnSe wires with ~150 nm silica struts separating each wire. Compared to the silica clad, ZnSe core step index fibers, the ZnSe MOF has a cladding with a higher effective index than pure silica so that a reduced number of core modes can be selectively coupled. This ZnSe fiber is effectively dual

mode over a wide wavelength range (**Figure 5.5b,c**), though with further optimization of the MOF template and deposited material it should be possible to design a ZnSe MOF for effective single mode operation.[23] Transmission measurements in this microstructured ZnSe fiber at 1550 nm show it has a loss of 1.9 dB/cm. This slightly higher loss value than in a silica clad, step index ZnSe optical fiber is likely to be due to the enhanced interaction of the core guided light with the high index microstructured cladding, which could result in scattering losses.

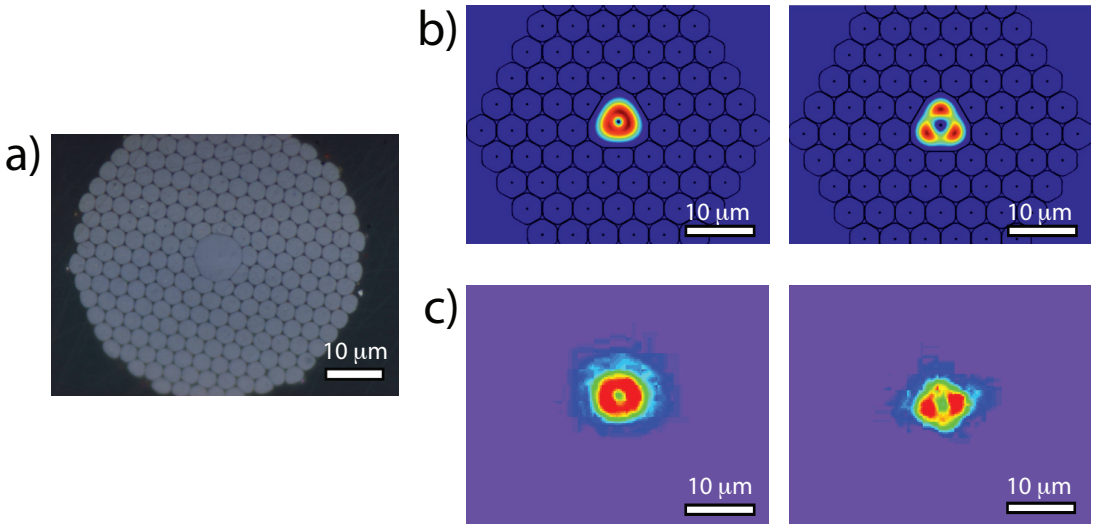

Figure 5.5: Large mode area ZnSe optical fiber. Due to the low core/cladding index contrast of the structured fiber, only two modes are supported (b), which can be isolated experimentally (c).

5.3 Nonlinear Properties of ZnSe Optical Fibers

Nonlinear fiber optics is a very exciting field owing to the long interaction lengths possible with optical fibers that can exploit weak optical effects.[24] For almost any nonlinear process, it is ideal to maximize the intensity of the light and the length of interaction; therefore, the small core size and long length of optical fibers make them the ideal choice of geometry. Nonlinear optical effects arise when high peak power densities of light are impingement on a material, which leads to an intensity-dependent refractive index. At high optical field intensities,

the polarization of a material system depends on the strength of the applied optical field and can be defined as:[18]

$$P(t) = \varepsilon_0[\chi^{(1)}E(t) + \chi^{(2)}E^2(t) + \chi^{(3)}E^3(t) + \ldots] \quad \textbf{(Equation 5.3)}$$

where ε_0 is the permittivity of free space, $P(t)$ is the induced polarization, and $E(t)$ is the time varying applied optical field.

The quantities $\chi^{(n)}$ are the *n*th order susceptibilities. Depending on the symmetry of the material system, the second order susceptibility ($\chi^{(2)}$) can be zero (centrosymmetric systems) or non-zero (noncentrosymmetric systems). Silica does not have second order susceptibility because of its structure; however, ZnSe ($F\bar{4}3m$ space group) is noncentrosymmetric and therefore has a non-vanishing $\chi^{(2)}$ value. It is worth noting that second order processes have been observed in silica fibers, but they are generally attributed to impurities and are very weak.[25] Second order nonlinearity has also been demonstrated in chalcogenide glass fibers designed with unique compounds that exhibit short range order.[26] While third order nonlinearity is a very useful property of a material for a variety of applications (it led to the development of the supercontinuum fiber laser), having second order function in an optical fiber enables a variety of unique processes.

5.3.1 Second Order Nonlinearity

Second order nonlinear processes are three photon events. A useful application of such processes is to generate laser light at wavelengths that are not accessible by conventional lasers. Two photons can be combined in a process called sum frequency generation (SFG) to produce a third photon that has an energy that is the sum of two. In contrast, one photon can be split into two photons of different energies in optical parametric generation (OPG). This is the basis for an

optical parametric oscillator, which is a laser system that is used extensively throughout this dissertation to access mid-IR wavelengths. Below are the equations for SFG, OPG, and a special case of SFG, second harmonic generation (SHG):

$$SFG: \omega_1 + \omega_2 \rightarrow \omega_3 \qquad \textbf{(Equation 5.4)}$$

$$OPG: \omega_1 \rightarrow \omega_2 + \omega_3 \qquad \textbf{(Equation 5.5)}$$

$$SHG: \omega_1 + \omega_1 \rightarrow \omega_2 \qquad \textbf{(Equation 5.6)}$$

Energy is conserved in all cases. In this section, SHG, which is sometimes referred to as frequency doubling, will be demonstrated in ZnSe optical fibers.

5.3.2 Phase Matching

In order for a SHG process to be efficient, the phases of the three waves must be matched such that they coherently add up as the two beams propagate in the material. If the two wavelengths are not in phase, the optical power can flow back and forth from the converted waves to the pumping waves to result in low conversion efficiency. In the polycrystalline ZnSe optical fibers, phase matching can be achieved in two ways: modal phase matching and random quasi phase matching. In modal phase matching, the mode of the pump wavelength and the mode of the SHG signal both have the same propagation constant and are thus in phase; the efficiency of the process scales with the square of the interaction length. This is difficult to achieve without proper dispersion and waveguide engineering. In random phase matching,[27] the relative phases of the pump and signal can be coherently added by the random motion of the phases as the light enters each grain of the polycrystalline material. Such an effect is not observed in a single crystal, but the SHG can occur with reasonable efficiency with a linear dependence on interaction length when this random walk effect occurs in polycrystalline material. This is likely the mechanism that

will occur in simple step index ZnSe optical fibers. Another way to achieve phase matching is to pole the material to introduce a controlled periodic domain profile, known as quasi phase matching. Methods to pole the optical fibers are currently being investigated in the Badding group. Nonlinear processes typically require high optical power densities, which make the high damage threshold ZnSe optical fibers very good candidates.

5.3.3 Second Harmonic Generation in ZnSe Optical Fibers

Second harmonic generation was observed and characterized in a silica clad, 15 μm diameter core ZnSe optical fiber. A Mai Tai HP mode-locked Ti:Sapphire laser that generates ~100 fs pulses at a repetition rate of 80 MHz with ~2 W average power (250 kW peak power) was used as a pump beam. For longer wavelengths, an optical parametric oscillator (which uses OPG processes) was pumped with the Mai Tai laser to generate wavelengths out to 1700 nm. This light was coupled into the ZnSe optical fiber with a 40× objective. Light was coupled out with another objective and coupled into a spectrometer for spectral measurements or to a power meter for power measurements. A photograph of the optical fiber generating 500 nm light while being pumped with 1000 nm light is shown in **Figure 5.6**.

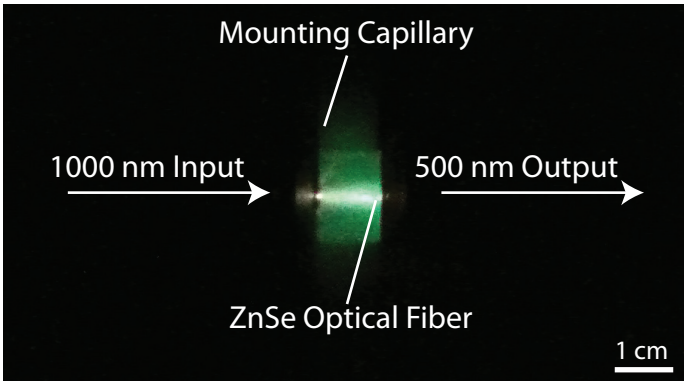

Figure 5.6: Photograph of a ZnSe optical fiber generating second harmonic light.

The SHG signal is observed over a broad wavelength range from 460 – 850 nm as shown in **Figure 5.7a**. The low wavelength limit is due to bandgap absorption, while the upper limit was simply due to a pump laser source not being available at the time of the measurement. The power conversion efficiency was measured as a function of wavelength (**Figure 5.7b**). The efficiency increases as the SHG signal approaches the bandgap, which is consistent with observations in poled, quasi phase matched single crystal waveguides.[4,28]

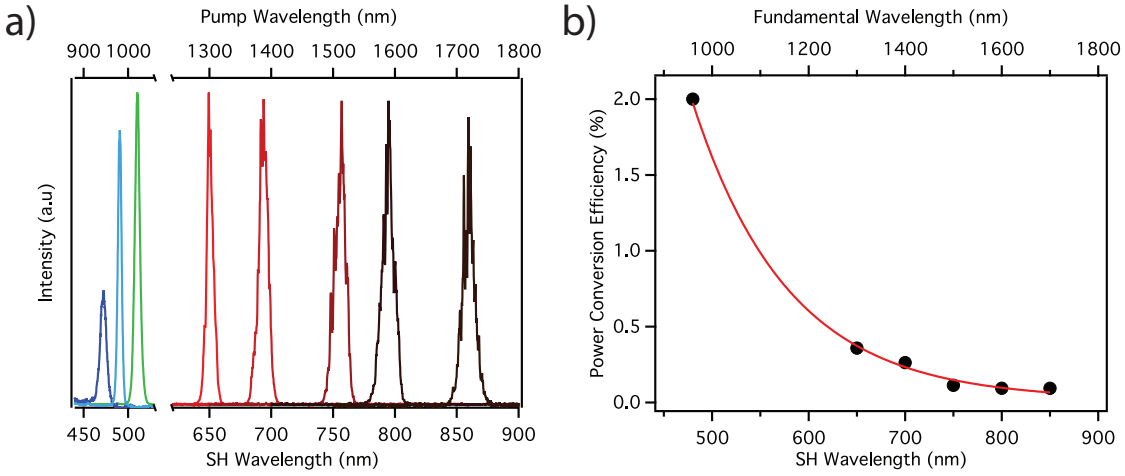

Figure 5.7: Spectral dependence of second harmonic generation in ZnSe optical fibers. (a) SHG spectra as a function of fundamental wavelength input. (b) The efficiency of the SHG process increases as the SHG wavelength approaches the bandgap.

To determine the maximum efficiency for the SHG process, the power conversion efficiency as a function of input power was determined at 1300 nm pump wavelength (**Figure 5.8a**). As the power increases, the system appears to saturate at 4.5% power conversion efficiency at a power density of 2.5 GW/cm^2. Overall, the efficiency is comparable to literature, where 0.8% efficiency (1400 nm pump 3 GW/cm^2) has been reported.[29]

In order to determine the mechanism of the process (modal versus random phase matching), two experiments were carried out. In the first experiment, the efficiency of the SHG conversion versus length was determined (**Figure 5.8b**), which resulted in a linear length dependence; a characteristic result of random quasi phase matching. In the second experiment, a

low-mode, large mode area ZnSe optical fiber was employed (**Section 5.2.2**). Since this fiber has far fewer modes than a silica step index ZnSe fiber, it is very unlikely that modes will exist at the pump and SHG wavelengths that have the same propagation constant. If the mechanism relies on modal phase matching, then the LMA fiber would have considerably less efficiency. However, it was found that the LMA fiber had similar efficiency to a simple step index fiber. Both of these experiments indicate that random quasi phase matching is the mechanism of SHG in ZnSe optical fibers.

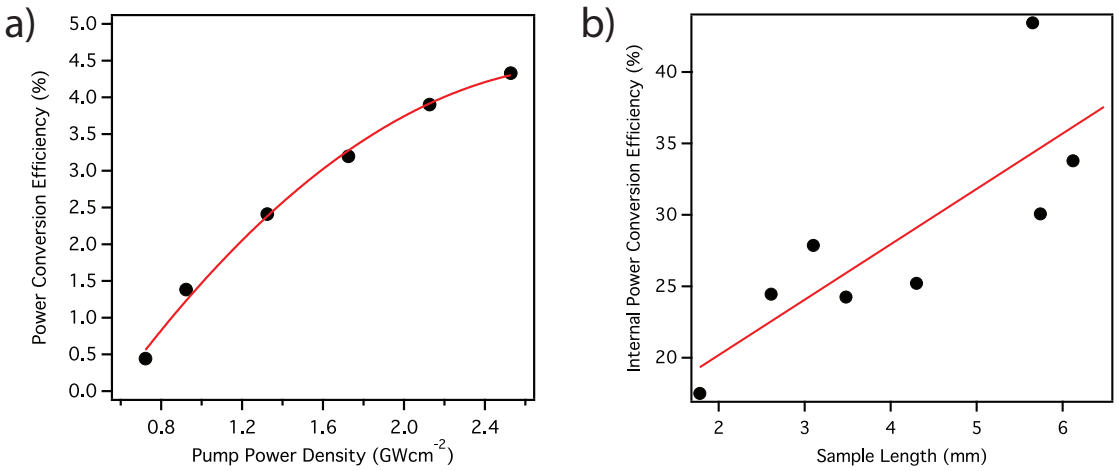

Figure 5.8: Input power and length dependence of second harmonic generation efficiency in ZnSe optical fibers. (a) The efficiency at a pump wavelength of 1300 nm tends to saturate to 4.5%. (b) The efficiency scales roughly linearly with length, which indicates that random quasi phase matching is the dominant mechanism. The "internal" efficiency was calculated by taking into account the high loss of the optical fiber waveguide in the visible region.

With further optimization and engineering of the waveguides, higher efficiencies should be possible. For example, the ideal core area for SHG efficiency can be calculated[30] to be 400 nm diameter for 1.3 μm pump. Further improvements in the HPCVD reactions are needed to fabricate such structures such as the single crystal transport reactions presented in **Chapter 4**. Instead of relying on the polycrystalline grain structure of the material for phase matching, it would be desirable to employ a poled single crystal with a well-defined periodicity for the desired wavelengths for quasi phase matching. Furthermore, the ability to generate new wavelengths in

the mid-IR from Cr^{2+}:ZnSe optical fiber lasers as the sources for OPG and other processes opens up a new platform for mid-IR fiber optic laser sources.

5.4 Tapered Fibers for Sub-Wavelength Imaging in the IR

This work was carried out in collaboration with Mahesh Krishnamurthi and Eftihia Barnes of the Gopalan group (Materials Science and Engineering, PSU).[31,32] Modified figures and sections from references [31,32] are reproduced with permission.

5.4.1 Motivation

Infrared imaging with high resolution is of increasing importance in research areas such as chemical sensing, biomedical diagnosis, thermography, non-destructive testing and astronomy.[33-38] Contemporary high resolution infrared imaging tools are based either on solid immersion lenses or near-field scanning techniques, or a combination of both.[39-42] The solid immersion lens offers diffraction limited imaging over larger areas with high optical throughput, while the near-field technique offers excellent resolution beyond the diffraction limit,[43,44] but with low optical throughput and longer acquisition times. For far-field infrared imaging, flexible optical fiber bundle endoscopes are a preferred technique for rapid imaging of specimens with restricted optical access in a minimally invasive manner.[45] The incumbent technology for infrared imaging between 2 – 10 μm wavelengths using coherent optical fiber bundles is based on arrays of either hollow metallic or chalcogenide core waveguides. These imaging bundles operate over a broad wavelength range, but have been limited to modest pixel sizes of the order of 50 – 100 μm. Therefore, there is a need for low-loss, broadband imaging systems with high resolution at mid-IR wavelengths.

The conceptual design, fabrication scheme, and optical characterization of an imaging system based on deposited semiconductor waveguides in tapered MOFs are discussed in this section. The transfer of an image with magnification across the fiber element is demonstrated at 3.39 μm and 10.6 μm.

5.4.2 Fabrication

A tapered MOF, fabricated using a standard fusion splicer (**Figure 5.9**), acts as the template for an array of infrared waveguides within each of its capillaries. The MOF has 168 capillaries (to-be-pixels) in a hexagonal arrangement, and the length of the tapered section is 300 μm. At the wider end, the capillaries have a diameter of 9 μm (**Figure 5.9d**), whereas at the narrow end they are tapered down to 3 μm (**Figure 5.9e**). First, a 1 μm layer of ZnSe (n~2.4) was deposited in the capillaries, followed by completely filling them with germanium (n~4) from GeH_4 pyrolysis; therefore each of these ZnSe clad, germanium core infrared cylindrical waveguides acts like a pixel. In this design, a magnified image is transmitted from the near-field at the input (narrow end) with sub-wavelength resolution to the un-tapered output (wider end) of the MOF. Tapering the waveguide to sub-wavelength dimensions is feasible since the symmetric cylindrical waveguides have no cut-off diameter. The un-tapered output (wider end) is shown in **Figure 5.9d**, while the polished input (narrow end) of the fiber element is shown in **Figure 5.9e**. The diameter of the germanium core is 2 μm at the input and 7 μm at the output; whereas the center-center spacing between adjacent capillaries is 14 μm at the input and 9.5 μm at the output. The ZnSe cladding thickness is < 1 μm at the input and 1 μm at the output. Therefore, the tapered geometry has a 2 μm resolution, 3.5× pixel magnification and 1.5× pitch magnification.

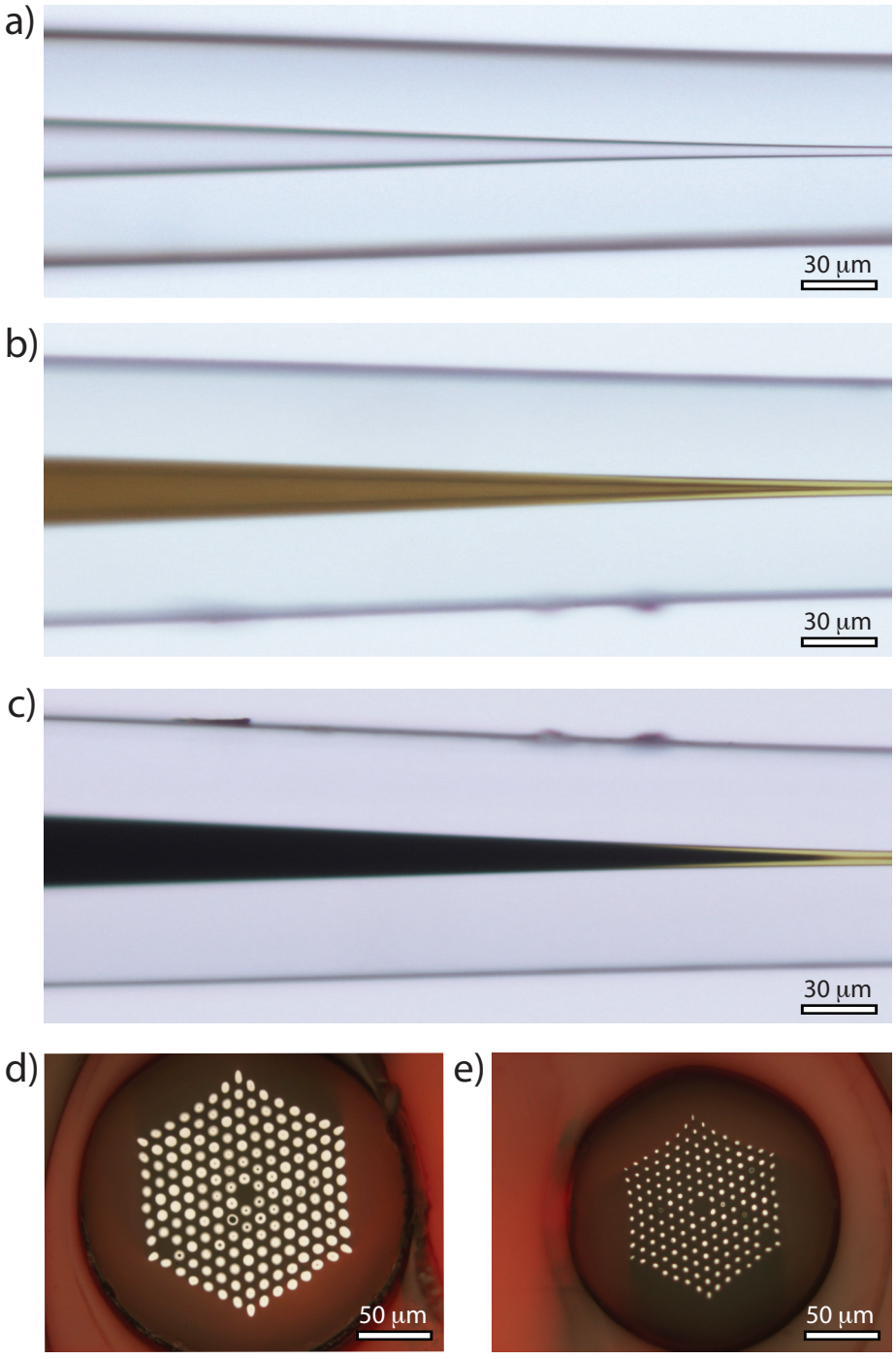

Figure 5.9: Fabrication of tapered ZnSe/Ge waveguide arrays. For simplicity, a single tapered capillary (a) is used to demonstrate the deposition process of depositing a ZnSe layer first (b), followed by completely filling in the channel with germanium (c). The deposition process is readily extended to the MOF, where (d) is the polished output facet and (e) is the polished input facet of the fiber element.

5.4.3 Characterization

The fiber element was employed to transmit the magnified image of an object with sub-wavelength features from the near-field of its input to its output (**Figure 5.10a**). In order to imitate an object with sub-wavelength feature size, a metal mask with the "λ/N" pattern was fabricated in contact with the input of the fiber element, as shown in **Figure 5.10b**. A uniform layer of 10 nm of chromium (adhesion layer) and 100 nm of gold were deposited onto the input facet, and the "λ/N" pattern was selectively milled with gallium ions in a focused ion beam system. Therefore the metal mask itself can be considered as the sample to be imaged.

Under uniform illumination, the "λ/N" pattern at the fiber element input was transmitted to its output plane as shown in **Figure 5.10c** for $\lambda = 3.39$ μm and **Figure 5.10d** for $\lambda = 10.64$ μm. In addition, the scale bars for **Figure 5.10c,d** have been calibrated with respect to the "λ/N" dimensions at the input of the fiber element. The variation in the intensity profile of each guiding pixel can be attributed to variation in the germanium core diameters as shown in **Figure 5.9**; the uniformity can be improved by optimizing the HPCVD reactions in tapered structures. Pixel cross-talk, which is defined as the ratio of the power at the output of a pixel which is not illuminated and is located next to an illuminated pixel, to the power output of the illuminated pixel, was estimated to be ~ 7% and 12% for $\lambda = 3.39$ μm and $\lambda = 10.64$ μm, respectively. These values are somewhat higher than theoretical calculations (< 2%) and could be further reduced by decreasing the interface roughness between the germanium core and the ZnSe cladding and reducing the variability of the ZnSe cladding thickness in the pixels. In addition, since the actual ZnSe cladding thickness of the fiber element was measured to be ~1 μm, a slightly thicker cladding layer would more efficiently confine the guided modes inside the cores.

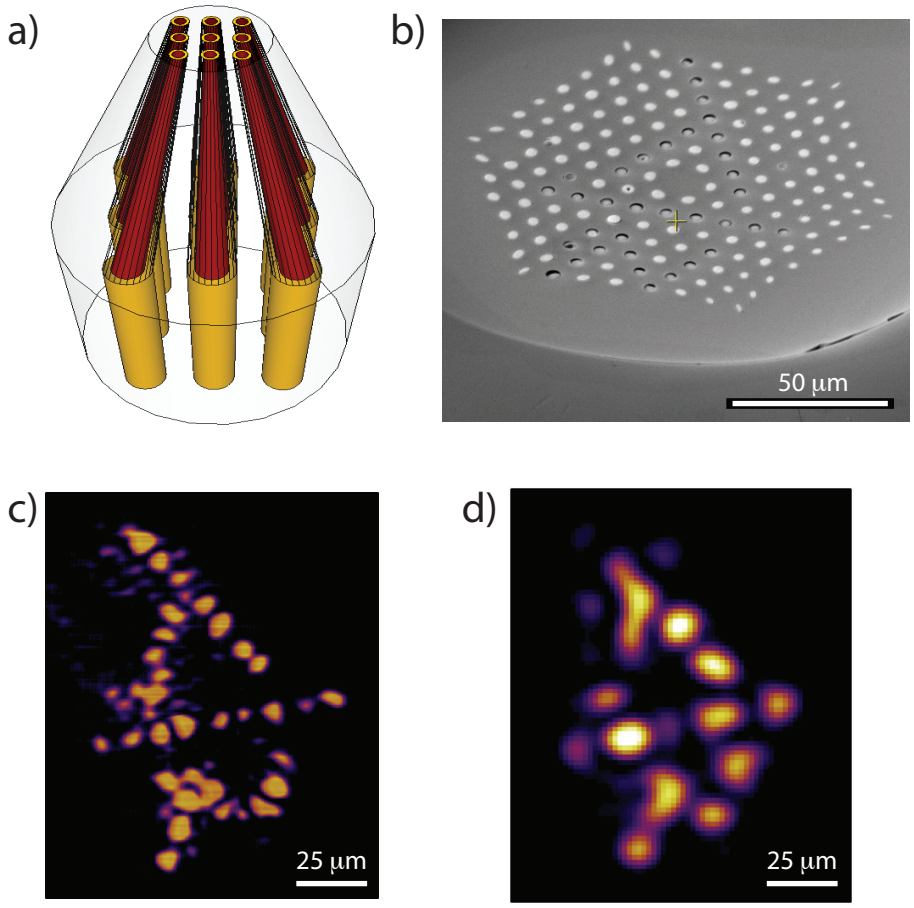

Figure 5.10: Sub-wavelength imaging in the mid-IR. (a) Schematic of the tapered fiber element that is used for image transfer. (b) A sub-wavelength feature is patterned on the input end of the fiber element for near field imaging. The transferred image at the output facet is shown in (c) for 3.39 μm and (d) for 10.6 μm wavelengths. Credit: Mahesh Krishnamurthi.

Even with this high cross-talk, IR imaging with sub-wavelength pixel size using a semiconductor filled fiber element has been demonstrated. A near-field image with sub-wavelength feature size (< 3 μm) was efficiently transmitted with a built-in pixel magnification of 3.5× and pitch magnification of 1.5× at λ = 3.39 μm and λ = 10.64 μm. This device can be used for near-field imaging applications in the 2 – 15 μm mid-infrared regime, owing to the transparency of germanium and ZnSe (**Table 1.1**). The primary advantage of this imaging technique is the high information throughput (parallel process) with sub-wavelength resolution

combined with built-in magnification. With further improvements to optical losses in materials, these features could be useful in fields such as near-field photolithography, and IR endoscopy.

5.5 Improving Loss

Although the losses in the structures presented in this chapter are low, it is desirable to continue to decrease the loss towards the theoretical limits discussed in **Chapter 1**. Likely sources of loss in the II-VI semiconductor optical fibers are geometric imperfections associated with the central void and material imperfections such as chemical impurities, grain boundaries and defects within grains. The presence of the central hole is certainly not desirable for optics applications as it can affect the mode structure of the waveguide and cause scattering. The surface roughness of this interior pore is determined by the texture of the deposited film, which can be controlled and optimized via the reactant ratio. Higher pressure deposition at higher precursor concentrations and/or cycling the precursor pressure should allow for smaller pore diameters via smaller grain growth. Another approach to reducing the scattering of light associated with this central imperfection would be to increase the waveguide diameter to reduce the impact of the central pore on loss. Also, there are many stacking faults and twinning defects in the material, which can cause scattering of light as it propagates through the structure.

Thermal and laser annealing could reduce these defects and allow for the growth of larger grains. Further reduction in chemical impurities, particularly for ZnS as mentioned previously, could also allow for lower loss. An obvious route to lowering the losses is to eliminate the central hole with the annealing techniques discussed in **Chapter 4**, which also grows larger grains that will reduce scattering losses. High purity, single crystal structures fabricated by vapor transport reactions are also a means to reduce the loss. Large core fibers have been fabricated (**Section 5.1.4**), with thermal expansion matched aluminosilicate glass, but this glass does not have a high

enough glass transition temperature (T_g= 790 °C) for the annealing and transport reactions. A GeO_2 doped silica glass will have the desired properties for these high temperature processes but it is significantly more difficult to synthesize and draw. However, Pier J. A. Sazio and collaborators at the University of Southampton are making progress in this area. Nonetheless, the losses and structures demonstrated in this chapter are adequate to move on to fabricating the first Cr^{2+}:ZnSe optical fiber laser.

5.6 References

[1] P. J. Roberts, F. Couny, H. Sabert, B. J. Mangan, D. P. Williams, L. Farr, M. W. Mason, A. Tomlinson, T. A. Birks, J. C. Knight, and P. St. J. Russell, "Ultimate Low Loss of Hollow-Core Photonic Crystal Fibres" *Opt. Express* **2005**, 13, 236.

[2] S. Morris, T. Hawkins, P. Foy, J. Hudson, L. Zhu, R. Stolen, R. Rice, and J. Ballato, "On Loss in Silicon Core Optical Fibers" *Opt. Mater. Express* **2012**, 2, 1511.

[3] G. Bacher, M. Illing, A. Forchel, D. Hommel, B. Jobst, and G. Landwehr, "Deep Etched ZnSe-Based Nanostructures for Future Optoelectronic Applications" *Phys. Stat. Sol. B* **1994**, 187, 371.

[4] H. P. Wagner, "Second Harmonic Generation in Thin Film II-VI Optical Waveguides" *Phys. Stat. Sol. B* **1995**, 187, 363.

[5] K. Akita, R. Akimoto, B. S. Li, T. Hasama, and Y. Takanashi, "Fabrication of High-Mesa Waveguides Based on Wide-Band-Gap II-VI Semiconductors for Telecom Wavelength Applications" *Jpn. J. Appl. Phys.* **2007**, 46, 200.

[6] M. Kuhnelt, T. Leichtner, S. Kaiser, B. Hahn, H. P. Wagner, D. Eisert, G. Bacher, and A. Forchel, "Quasiphase Matched Second Harmonic Generation in ZnSe Waveguide Structures Modulated by Focused Ion Beam Implantation" *Appl. Phys. Lett.* **1998**, 73, 584.

[7] W. E. Martin and D. B. Hall, "Optical Waveguides by Diffusion in II-VI Compounds" *Appl. Phys. Lett.* **1972**, 21, 325.

[8] H. F. Taylor, W. E. Martin, D. B. Hall, and V. N. Smiley, "Fabrication of Single-Crystal Semiconductor Optical Waveguides by Solid-State Diffusion" *Appl. Phys. Lett.* **1972**, 21, 95.

[9] B. G. Kim, E. Garmire, N. Shibata, and S. Zembutsu, "Optical Bistability and Nonlinear Switching Due to Increasing Absorption in Single-Crystal ZnSe Waveguides" *Appl. Phys. Lett.* **1987**, 51, 475.

[10] H. Babucke, P. Thiele, T. Prasse, M. Rabe, and F. Henneberger, "ZnSe-Based Electro-Optic Waveguide Modulators for the Blue-Green Spectral Rang," *Semicond. Sci. Technol.* **1998**, 13, 200.

[11] M. A. Haase, H. Cheng, D. K. Misemer, T. A. Strand, and J. M. DePuydt, "ZnSe-ZnSSe Electro-Optic Waveguide Modulators" *Appl. Phys. Lett.* **1991**, 59, 3228.

[12] M. H. Jupina, E. M. Garmire, N. Shibata, and S. Zembutsu, "ZnSe/$ZnSe_{0.92}S_{0.08}$/GaAs Single-Crystal Waveguides as Visible Modulators" *Appl. Phys. Lett.* **1990**, 57, 2894.

[13] W. E. Martin, "Waveguide Electro-Optic Modulation in II-VI Compounds" *J. Appl. Phys.* **1973**, 44, 3703.

[14] J. E. Williams, V. V. Fedorov, D. V. Martyshkin, I. S. Moskalev, R. P. Camata, and S. B. Mirov, "Mid-IR Laser Oscillation in Cr^{2+}:ZnSe Planar Waveguide" *Opt. Express* **2010**, 18, 25999.

[15] B. J. Eggleton, B. Luther-Davies, and K. Richardson, "Chalcogenide photonics" *Nature Photon.* **2011**, 5, 141.

[16] B. Temelkuran, S. D. Hart, G. Benoit, J. D. Joannopoulos, and Y. Fink, "Wavelength-Scalable Hollow Optical Fibres with Large Photonic Bandgaps for CO_2 Laser Transmission" *Nature* **2002**, 420, 650.

[17] R. M. Wood, "*Laser-Induced Damage of Optical Materials*" Institute of Physics Publishing, **2003**.

[18] R. W. Boyd, "*Nonlinear Optics*" Elsevier, **2008**.

[19] C. R. Pollock, "*Fundamentals of Optoelectronics*" Ceramic Book and Literature Service, **1995**.

[20] B. E. A. Saleh and M. C. Teich, "*Fundamentals of Photonics*" Wiley-Interscience, **2007**.

[21] M. Ashraf, S. M. J. Akhtar, M. Mehmood, and A. Qayyum, "Optical and Structural Properties of ZnS_xSe_{1-x} Thin Films Deposited by Thermal Evaporation" *Eur. Phys. J. Appl. Phys.* **2009**, 48, 10501.

[22] M. Kuhnelt, L. Reindl, E. Griebl, B. Hahn, S. Kaiser, M. Kastner, H. Preis, T. Frey, T. Reisinger, H. P. Wagner, and W. Gebhardt, "Ternary II-VI Compounds for Optical Waveguides" *J. Cryst. Growth* **1998**, 184, 1165.

[23] N. Vukovic, N. Healy, and A. C. Peacock, "Guiding Properties of Large Mode Area Silicon Microstructured Fibers: A Route to Effective Single Mode Operation" *J. Opt. Soc. Am. B* **2011**, 28, 1529.

[24] J. M. Dudley and J. R. Taylor, "Ten Years of Nonlinear Optics in Photonic Crystal Fibre" *Nature Photon.* **2009**, 3, 85.

[25] W. Margulis and U. Osterberg, "Second-Harmonic Generation in Optical Glass Fibers" *J. Opt. Soc. Am. B* **1988**, 5, 312.

[26] I. Chung, J. I. Jang, C. D. Malliakas, J. B. Ketterson, and M. G. Kanatzidis, "Strongly Nonlinear Optical Glass Fibers from Noncentrosymmetric Phase-Change Chalcogenide Materials" *J. Am. Chem. Soc.* **2009**, 132, 384.

[27] M. Baudrier-Raybaut, R. Haidar, P. Kupecek, P. Lemasson, and E. Rosencher, "Random Quasi-Phase-Matching in Bulk Polycrystalline Isotropic Nonlinear Materials" *Nature* **2004**, 432, 374.

[28] H. P. Wagner, M. Kuhnelt, W. Langbein, and J. M. Hvam, "Dispersion of the Second-Order Nonlinear Susceptibility in ZnTe, ZnSe, and ZnS" *Phys. Rev. B* **1998**, 58, 10494.

[29] H. Yang, P. Xie, S. K. Chan, Z. Q. Zhang, I. K. Sou, G. K. L. Wong, and K. S. Wong, "Efficient Second Harmonic Generation from Large Band Gap II-VI Semiconductor Photonic Crystal" *Appl. Phys. Lett.* **2005**, 87, 131106.

[30] M. A. Foster, K. D. Moll, and A. L. Gaeta, "Optimal Waveguide Dimensions for Nonlinear Interactions" *Opt. Express* **2004**, 12, 2880.

[31] M. Krishnamurthi, E. Barnes, J. R. Sparks, R. He, N. F. Baril, P. J. A. Sazio, J. V. Badding, and V. Gopalan, "A Magnifying Fiber Element with an Array of Sub-Wavelength Ge/ZnSe Pixel Waveguides for Infrared Imaging" *Appl. Phys. Lett.* **2012**, 101, 021108.

[32] M. Krishnamurthi, J. R. Sparks, R. He, I. A. Temnykh, N. F. Baril, Z. Liu, P. J. A. Sazio, J. V. Badding, and V. Gopalan, "Array of Tapered Semiconductor Waveguides in a Fiber for Infrared Image Transfer and Magnification" *Opt. Express* **2012**, 20, 4168.

[33] P. W. Kruse, and D. D. Skatrud *"Uncooled Infrared Imaging Arrays and Systems*" Academic Press, **1997**.

[34] R. Weissleder, C. H. Tung, U. Mahmood, A. Bogdanov, "In Vivo Imaging of Tumors with Protease-Activated Near-Infrared Fluorescent Probes" *Nature Biotech.* **1999**, 17, 375.

[35] O. S. Wolfbeis, "Fiber-Optic Chemical Sensors and Biosensors" *Anal. Chem.* **2004**, 76, 3269.

[36] J. Zhang, Y. Kim, Y. Kim, R. Valencia, T. D. Milster, and D. Dozer, "High Resolution Semiconductor Inspection by Using Solid Immersion Lenses" *Jpn. J. Appl. Phys.* **2009**, 48, 03A043.

[37] M. H. Li, J. J. Wu, and Y. B. Gianchandani, "Surface Micromachined Polyimide Scanning Thermocouple Probes" *J. Microelectromech. Sys.* **2001**, 10, 3.

[38] Y. Kim, J. Zhang, and T. D. Milster, "GaP Solid Immersion Lens Based on Diffraction" *Jpn. J. Appl. Phys.* **2009**, 48, 03A047.

[39] C. A. Michaels, "Mid-Infrared Imaging with a Solid Immersion Lens and Broadband Laser Source" *Appl. Phys. Lett.* **2007**, 90, 121131.

[40] F. Huth, M. Schnell, J. Wittborn, N. Ocelic, and R. Hillenbrand, "Infrared-Spectroscopic Nanoimaging with a Thermal Source" *Nature Mater.* **2011**, 10, 352.

[41] T. Masaki, Y. Inouye, and S. Kawata, "Submicron Resolution Infrared Microscopy by Use of a Near-Field Scanning Optical Microscope with an Apertured Cantilever" *Rev. Sci. Instrum.* **2004**, 75, 3284.

[42] B. A. Flusberg, E. D. Cocker, W. Piyawattanametha, J. C. Jung, E. L. M. Cheung, and M. J. Schnitzer, "Fiber-Optic Fluorescence Imaging" *Nature Methods* **2005**, 2, 941.

[43] S. Szunerits and D. R. Walt, "The Use of Optical Fiber Bundles Combined with Electrochemistry for Chemical Imaging" *Chem. Phys. Chem*. **2003**, 4, 186.

[44] A. D. Mehta, J. C. Jung, B. A. Flusberg, and M. J. Schnitzer, "Fiber Optic in vivo Imaging in the Mammalian Nervous System" *Curr. Opin. Neurobiol.* **2004**, 14, 617.

[45] P. Lu, X. Bao, T. Whidden, and S. Y. Lee, "Application of a Mid-Infrared Fiber Bundle in Remote Measurement of Gas Concentrations in a Chemical Vapor Deposition Chamber" *Appl. Opt.* **2000**, 39, 1112.

Chapter 6

Transition Metal Doped II-VI Semiconductor Optical Fiber Lasers

ZnSe optical fibers can guide high powers of infrared light, which suggests that they hold promise for applications such as non-linear frequency conversion and high power fiber lasers. Cr^{2+} transition metal doped ZnSe lasers have many attractive characteristics, including high efficiency and tunability from 2 – 3 μm wavelengths. Unfortunately, ZnSe has a large thermo-optic coefficient that gives rise to thermal lensing and limits the power of lasers that use bulk gain media to ~10W. Fibers are noted for their excellent thermal management properties and they also tend to be less susceptible to thermal lensing. One of the first applications of ZnSe fibers may thus be high power tunable fiber lasers, which are discussed and demonstrated in this chapter.

6.1 Introduction to Transition Metal Doped II-VI Semiconductor Lasers

6.1.1 Substitutional Transition Metal Doping in the Zinc Blende Lattice

Cr^{2+} doped into the Zn lattice sites of polycrystalline ZnSe has been shown to be a useful nonlinear material as well as a tunable broadband laser in the mid-IR from 2.0 – 3.1 μm,[1] capable of generating ~10 W of CW power.[2,3] When chromium is substituted into the Zn sites with tetrahedral (T_d) symmetry in cubic ZnSe, the *e* set and t_2 set valence 3d orbitals of the ion are very weakly split. Two quintet states, with the term symbols ^5E and $^5T_2$, are the lowest energy states available to the system.[4] All other states close in energy are either singlets or triplets, so the only spin allowed electronic transition is between these two electronic states. The two states are further split by the Jahn-Teller effect to produce a four level system. Therefore, Cr^{2+}:ZnSe

does not exhibit any excited state spin allowed transitions from these quintet states, which makes it an ideal four-level laser with high gain (approximately 70% slope efficiency). Furthermore, the matrix, ZnSe, has a low phonon frequency of 250 cm^{-1} that plays three roles in the laser system.[5] First, relaxation of an electron from the excited state back to the ground state is almost always accompanied by radiation because it would take an unlikely combination of many phonons to relax the electron down to the ground state; resulting in a quantum yield near unity. Second, since the phonon states are closely spaced, and the system is a vibronic laser, it is continuously tunable from 2.0 – 3.1 μm. Due to this tunability, Cr^{2+}:ZnSe is often referred to as the Ti^{3+}:sapphire of the mid-IR.[5] Third, even at room temperature, the phonons are not significant enough to result in radiationless relaxation, which allows for room temperature operation. Cr^{2+}:ZnSe is the only known room temperature laser that operates in this wavelength range.

By changing the transition metal or the host material, the wavelength of emission from transition metal doped II-VI semiconductors can be tuned over much of the IR spectrum. Fe^{2+} is a smaller ion and thus experiences an even weaker crystal field splitting in ZnSe, which results in the transition occurring further into the IR from 3.7 – 5.1 μm. The crystalline lattice can also be substituted with smaller sulfur ions in ZnS creating a stronger crystal field that splits the Cr^{2+} d-shell orbitals to transitions from 1.9 – 2.8 μm in Cr^{2+}:ZnS. Therefore, the high transparency of II-VI semiconductors in the IR along with their ability to generate light in the same region make them ideal materials for IR optics.[6] Fabricating these materials into the optical fiber geometry will create a new platform of mid-IR fiber optic lasers.

6.1.2 Thermo-Optic Effects in Bulk Cr^{2+}:ZnSe Lasers

High power lasers in the mid-IR are very useful for a variety of applications such as sensing, surgery, and infrared countermeasures. For example, the vibrational absorption of water

overlaps with the Cr^{2+}:ZnSe tuning range. Therefore, tuning the wavelength of the laser will determine the penetration depth in tissue for surgical cutting applications. The chemical fingerprint region of the electromagnetic spectrum is from 2 – 20 μm, which makes the II-VI laser materials useful for trace gas sensing and monitoring of smoke plumes and industrial waste. However, many of these applications require tens of Watts of power.

The power output of Cr^{2+}:ZnSe has been limited because of the high thermo-optic coefficient of ZnSe ($dn/dT = 70 \times 10^{-6}$ K^{-1}) and other II-VI compounds.[4] The effects of this are shown in **Figure 6.1** for Cr^{2+}:ZnS.[7] As the laser is pumped, the material absorbs the energy through small amounts of radiationless decay and the quantum defect and the temperature increases. The bulk crystal cannot radiate this heat effectively, and thus a temperature gradient is created across the material.[8] This temperature gradient induces a large change in the refractive index, which is manifested as a thermal lens that destroys the mode structure and quality of the laser. With poor overlap of the mode and pump laser, the output power becomes limited. To date, the highest power CW Cr^{2+}:ZnSe laser that has been achieved is 12 W by I. S. Moskalev *et. al.*,[6] which is primarily limited by these thermal effects. There has been a tremendous effort in the research community to develop novel pumping and cooling schemes to reduce this thermal load on the material. For a thorough review of the state of the art bulk Cr^{2+}:ZnSe lasers and geometries, see reference [6].

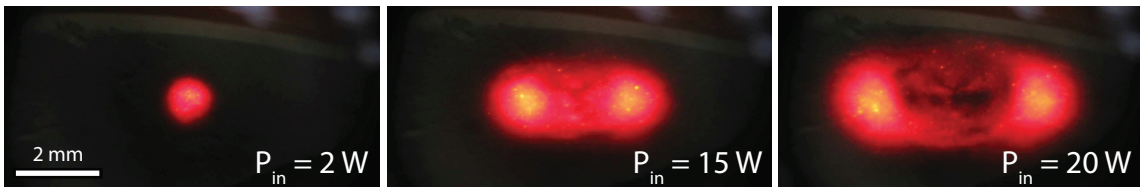

Figure 6.1: Thermal lensing in a Cr^{2+}:ZnS bulk laser. As higher pump power is used, the sample begins to develop a temperature gradient that causes lensing and distortion of the output beam, which limits the output power. Images modified with permission from reference [7], © 2009 OSA.

6.1.3 Advantages of the Waveguide / Optical Fiber Geometry

Moving to new geometries that have a high surface area to volume ratio are of interest for power scaling the lasers up to the levels needed for a variety of applications. Smaller structures such as planar waveguides can have much higher surface area to effectively radiate heat away from the laser. The first planar waveguide Cr^{2+}:ZnSe laser was demonstrated by J. E. Williams *et. al.* in 2010 with the goal of alleviating such effects.[9] The structure had a RMS surface roughness of 7 nm, much higher than that which can be achieved with HPCVD, and thus had high passive losses. These high losses have limited the laser to function only in the pulsed regime, with CW lasing not yet shown even at multi-watt pumping powers.[10] Most planar semiconductor waveguides have much smaller cores than optical fibers, limiting their power handling capability. Furthermore very long waveguides and circular cross-section waveguides that radiate heat symmetrically are in general more difficult to realize via planar fabrication. Asymmetric radiation of heat may have deleterious consequences, such as thermal lensing or generation of mechanical stresses due to thermal expansion mismatch.

Optical fibers are less susceptible to thermal lensing effects because of their long, small diameter cores that radiate heat much more effectively than bulk optics and thermo-optic induced changes in refractive index do not alter their light guiding properties significantly if they are symmetrical. Heat arising from light absorption and/or quantum defects in fiber laser gain media is radiated equally well over 360° of cross-sectional angle; the large surface area-to-volume ratio and long length of the fiber also facilitates management of this heat. The long length of an optical fiber allows for lower concentrations of active ions to be used, while still efficiently absorbing all of the pump light, which reduces the thermal load per unit length on the fiber. Owing to these effects, most of the world's most powerful commercially available lasers are fiber lasers.[11] In

view of these advantages, a fiber configuration is likely to be the most promising approach to Cr^{2+}:ZnSe lasers with good mode quality and powers of many tens of Watts or more.

6.2 Cr^{2+}:ZnSe Optical Fiber Fabrication by HPCVD

6.2.1 Diffusion Doping ZnSe Optical Fibers

Since the diffusion of chromium into ZnSe is by far the most common way to synthesize Cr^{2+}:ZnSe[12-14] (vapor transport of the bulk crystal,[15,16] or molecular beam epitaxy[17,18] have been demonstrated, but are much less common), it was the first approach that was explored. In this case, it can be considered a longitudinal diffusion mechanism, which is the diffusion of chromium along the axis of the waveguide from the two facets. This is not an ideal method in the fiber geometry as there will be a chromium concentration gradient (and thus a thermal load gradient) along the length of the fiber, due to the exponential nature of diffusion processes that occurs over short (millimeter) distances, but it provided a means to fabricate preliminary samples. Radial diffusion by first depositing chromium films in capillaries before the deposition of ZnSe, followed by the diffusion annealing in the radial direction is one way to produce structures with uniform chromium concentration along the length, but the deposition of pure chromium from various organometallic precursors [bis(benzene)chromium, chromium carbonyl, and chromium acetylacetonate] was not successful. Depositing pure, elemental chromium from organometallic precursors is notoriously difficult as carbide and oxide phases are readily formed.[19]

For longitudinal diffusion doping experiments, some of the micro-ampoule techniques that were presented in **Chapter 4** were employed. Using a 150 μm internal diameter capillary as an ampoule that can be sealed with an optical fiber fusion splicer allows for a much more clean, controlled way to treat the 125 μm outside diameter ZnSe waveguides as compared to putting

them into a "bulk" ampoule: a millimeter sized quartz tube. Furthermore, the small volume is necessary to keep the ZnSe from completely leaving the capillary to establish the vapor pressure at elevated temperature (see **Chapter 4**). The dopant used in these experiments was CrSe powder. The overall design is shown in **Figure 6.2**. A 5 mm long, 15 μm diameter core ZnSe optical fiber was placed in the ampoule along with CrSe powder. An empty 50 μm capillary spacer was used to keep the powder from physically touching the sample so that only CrSe vapor reached the facets for diffusion. The total length of the ampoule was 2 cm. The ampoule was sealed under vacuum using a fusion splicer, and then heated to 850 °C for 6 days to allow chromium to diffuse into the optical fiber.

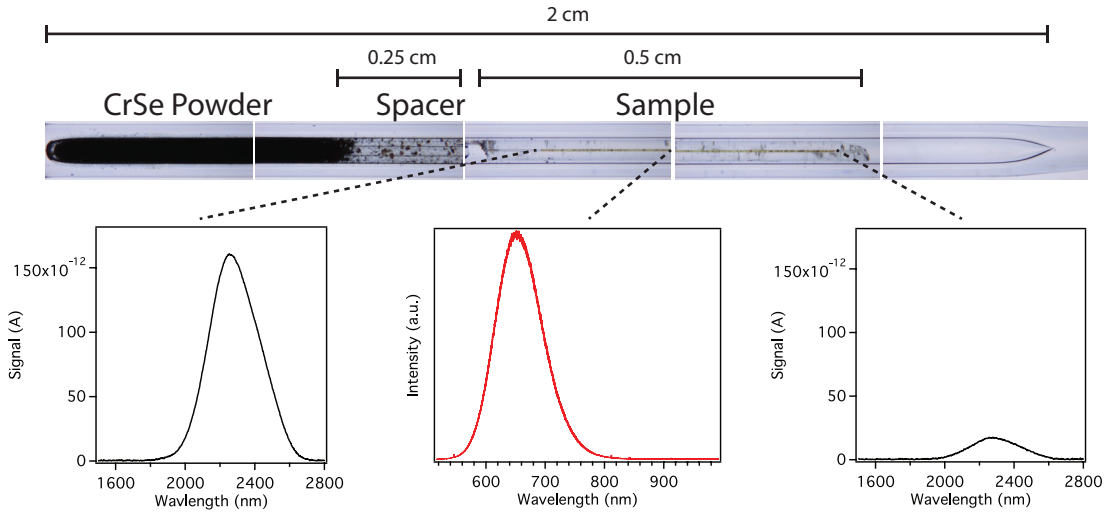

Figure 6.2: Cr^{2+} diffusion doping of ZnSe in a micro-ampoule. When the diffusion is carried out at 850 °C, the sample is doped only on the ends, with self activated emission from the central part of the optical fiber.

CW mid-IR fluorescence (pumped at 1550 nm erbium fiber laser or 1908 nm thulium fiber laser) from the Cr^{2+}:ZnSe is used throughout this chapter to qualitatively compare doping levels. The CW signal was chopped and dispersed through a motorized Monospec 18 spectrometer with a 300 g/mm, 2 μm blazed diffraction grating. The signal was measured with a Hamamatsu G5853-203 InGaAs or an Infrared Associates IS-0.5 InSb detector and processed

with a lock-in amplifier (SRS SR830). Mid-IR fluorescence from the Cr^{2+}:ZnSe was observed only to about 250 μm in from each facet of the 5 mm sample, showing the disadvantage of the longitudinal diffusion technique in that it is not applicable to the long optical fiber geometry (**Figure 6.2**). Also, due to the temperature gradient across the sample, the doping concentration is different at each end, as seen in the fluorescence intensity. The emission in the central region of the waveguide is dominated by self-activated emission, which is typically observed in samples when they are annealed at high temperatures. This emission results from Zn/Se vacancies and other defects that can develop without proper Se or Zn overpressure considerations. The inhomogeneities that can be seen in the structure are from cracking of the sample due to thermal expansion mismatch between the ZnSe and the silica capillary. This was observed in **Chapter 4** as well for single crystal/annealing experiments. Future glass development of systems such as germania/silica glasses for HPCVD should eliminate these problems. An alternative approach is to deposit a layer of refractory material (such as SiC or Si_xN_y) to act as the new cladding before deposition of the II-VI semiconductor. After etching the silica template away with HF, the structure could then be annealed without the thermal expansion constraints of silica and also allow for a higher thermal conductivity cladding that would be advantageous for high power laser applications. Although the longitudinal diffusion technique has significant drawbacks, it provided a means to characterize the fluorescence from the optical fibers and led to the drive to develop novel in-situ doping reactions.

6.2.2 Doping with Novel Organometallic Reactions in HPCVD

$Zn_{(1-x)}Cr_xSe$ solid solutions with a considerable range (x = 0 – 0.01) of stoichiometries exist as thermodynamically stable phases,[18] so doping during deposition should be feasible. In-situ doping of ZnSe during the deposition should result in a more uniform doping concentration

along the sample length as well as more control over the doping levels. Also, high temperature processing is not needed so cracking due to thermal expansion mismatch is not an issue. The major challenge is that the CVD of Cr^{2+}:ZnSe has not been reported in literature, so the chemistry to chemically deposit Cr^{2+}:ZnSe needed to be developed.

6.2.2.1 Chromium Carbonyl

There are not many volatile organometallic chromium sources that are applicable to HPCVD. In fact, $Cr(CO)_6$ seemed to be the only candidate that could be useful for initial experiments. Solid $Cr(CO)_6$ has a ~130 Pa vapor pressure at room temperature, so it can simply be added to the HPCVD reservoir in the solid state before the $(CH_3)_2Se$ and $(CH_3)_2Zn$ precursors. The main challenge with $Cr(CO)_6$ is that it decomposes at a much lower temperature (~250 °C) than the reaction temperature for ZnSe deposition (450 °C). This causes a chromium rich precursor mixture early in the furnace resulting in Cr/Zn rich islands forming on the surface of a thin ZnSe film. A SEM micrograph of the islands as well as energy dispersive spectroscopy showing the high level of Zn/Cr in them is shown in **Figure 6.3a,b**. Metallic zinc islands are very common in HPCVD when the VI/II precursor ratio is too low and can typically be eliminated by increasing the ratio. By changing the ratios of the $Cr(CO)_6$, $(CH_3)_2Se$, and $(CH_3)_2Zn$ in the reaction ($Cr(CO)_6$ vapor pressure; 4:1 VI/II ratio), a uniform film can be deposited, but the fluorescence intensity is much lower than that seen with diffusion doping (**Figure 6.3c,d**), which is likely due to the decomposition temperature differences of the chromium source and the ZnSe. As was discussed in **Chapter 4**, changing the R-group on the source molecule could provide a means to a lower ZnSe reaction temperature. In this case the $(t\text{-butyl})_2Se$ molecule may allow for very low temperature ZnSe deposition, where the $Cr(CO)_6$ molecule is much more thermally compatible.

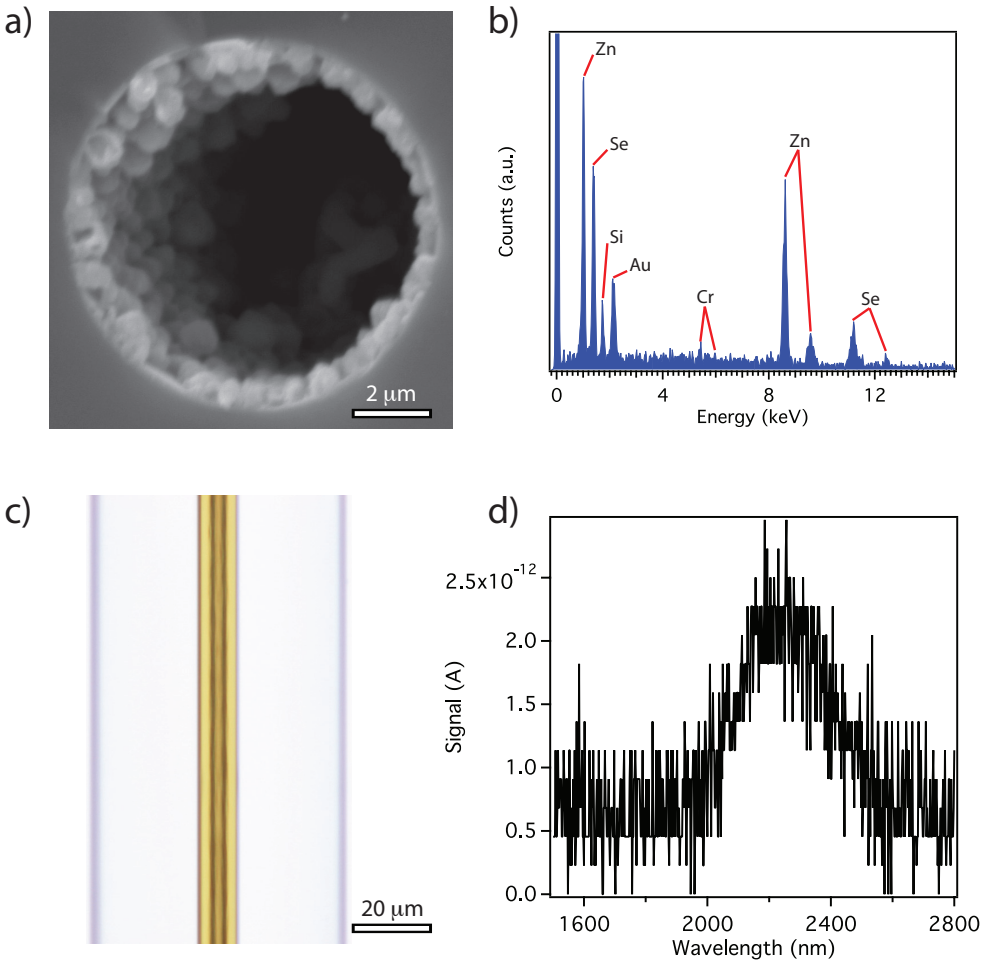

Figure 6.3: Deposition of Cr^{2+}:ZnSe with $Cr(CO)_6$ as the chromium source. Cr/Zn islands are observed in SEM (a) and EDS (b) when the reactant ratios are not optimized. After optimization, Cr^{2+}:ZnSe films can be deposited (c), but the doping level is very low as indicated by mid-IR emission (d) due to the low thermal stability of $Cr(CO)_6$ compared to the ZnSe reaction.

6.2.2.2 Splice Designs for Introduction of Solid State Precursors

Since the ZnSe deposition chemistry was thoroughly optimized with $(CH_3)_2Se$ and $(CH_3)_2Zn$, and because the $Cr(CO)_6$ could introduce oxygen contamination, other precursor molecules were investigated. As was stated earlier, many of the oxygen free chromium compounds are not volatile at room temperature and thus cannot be simply added to the HPCVD reservoir: the source needs to be heated to vaporize the molecules into the stream of the HPCVD

flow. This presents quite a challenge because the polymer tubing (polyether ether ketone-PEEK) that connects the capillary to the high pressure equipment softens above ~140 °C, while hydrogen embrittlement of the stainless steel becomes an issue at elevated temperatures.[20] Therefore, heating the HPCVD equipment is not ideal.

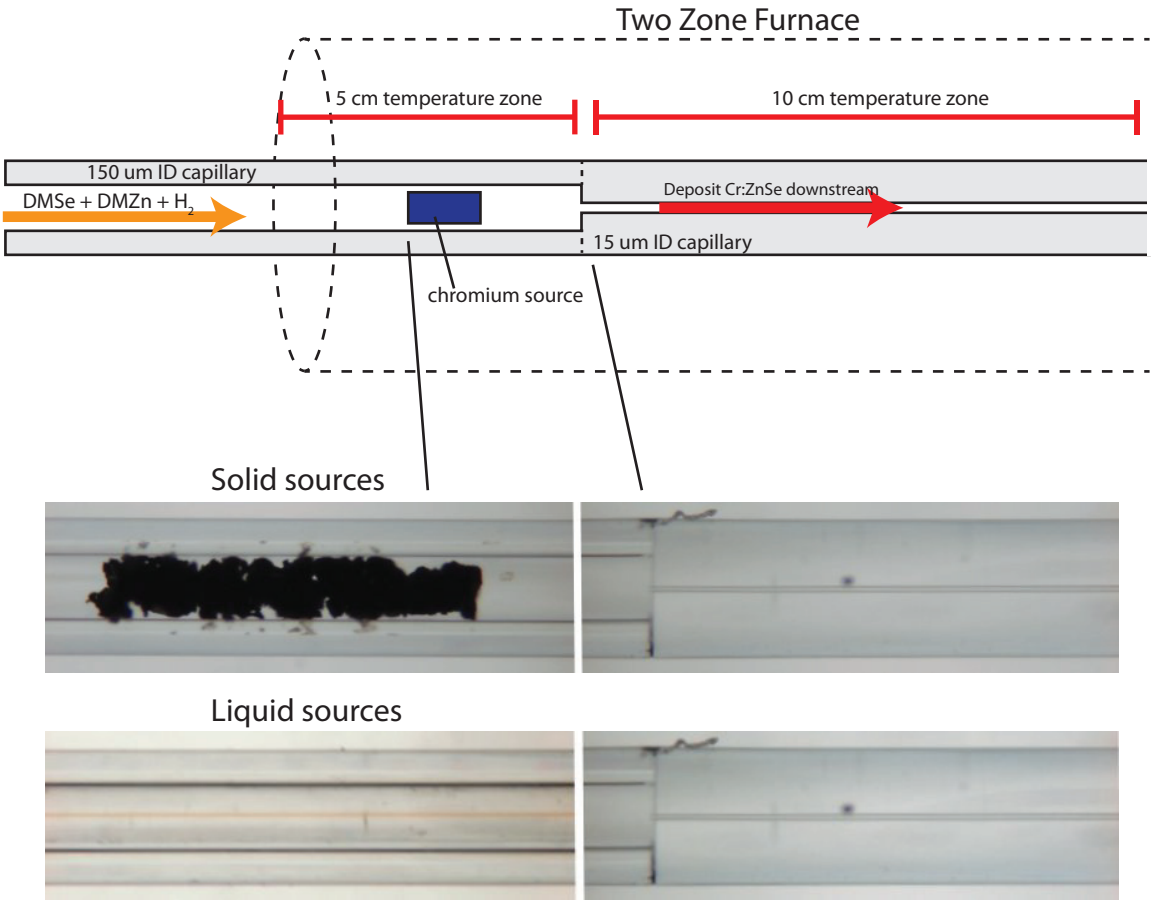

Figure 6.4: Splicing geometry to heat and introduce chromium sources during HPCVD. A two-zone furnace is used to heat a solid or liquid precursor that is contained in a larger capillary that is spliced to the targeted deposition capillary.

The highest purity way to approach this problem is shown in **Figure 6.4**, where a splice of a 150 μm internal diameter capillary to the target deposition capillary (15 μm diameter) is used to store the solid or liquid precursor, which can be heated without any of the before mentioned issues. By using a two-zone furnace to heat the capillary, the temperature, and thus the vapor pressure of the chromium source, can be controlled independently of any other variables. This

does complicate the HPCVD reaction in that the geometry of the fuse must be perfect (minimal tapering, no leaking, etc.) to not affect the deposition profile and stoichiometry of the Cr^{2+}:ZnSe. For example, if the splice results in a tapered target deposition capillary, a nozzle can form, which can cause a compression of the gas and lead to cooling (for H_2) of the carrier gas via the Joule-Thomson effect. This cooling of the HPCVD stream as it passes through the splice was modeled by the Borhan group in Chemical Engineering at PSU and can be significant (hundreds of °C; see **Chapter 2**) to result in the precipitation of the chromium precursor before it reaches the target deposition site in the second zone of the furnace.

6.2.2.3 Chromocene Derivatives

With a way to use heated precursors as chromium sources developed, many new molecules could be investigated. The first molecule that was investigated with this splice design was bis(cyclopentadienyl)chromium, chromocene [$Cr(Cp)_2$], which is a solid at room temperature and melts at ~250 °C. $Cr(Cp)_2$ does not decompose until ~525 °C, which makes it much more thermally compatible to the ZnSe deposition chemistry. When the reaction is carried out with the $Cr(Cp)_2$ source at 200 °C, a film of Cr^{2+}:ZnSe is deposited of similar structural quality compared to the ZnSe optical fibers that were presented in previous chapters (**Figure 6.5a**). The film has much higher fluorescence signal than the $Cr(CO)_6$ precursor, which is likely due to the thermal compatibility of the $Cr(Cp)_2$ molecule. Also, the signal is uniform over centimeter length scales, which indicates that the doping concentration is uniform (**Figure 6.5b**); a significant advantage over diffusion doping. Moving to higher source temperatures to achieve a higher vapor pressure and higher chromium doping level exacerbates the issues of a non-uniform splice, as the temperature drop increases with increasing starting gas temperature. Instead of increasing the

source temperature for higher doping levels, the stability of the molecule can be tailored so that it reacts at the same temperature as the ZnSe precursors.

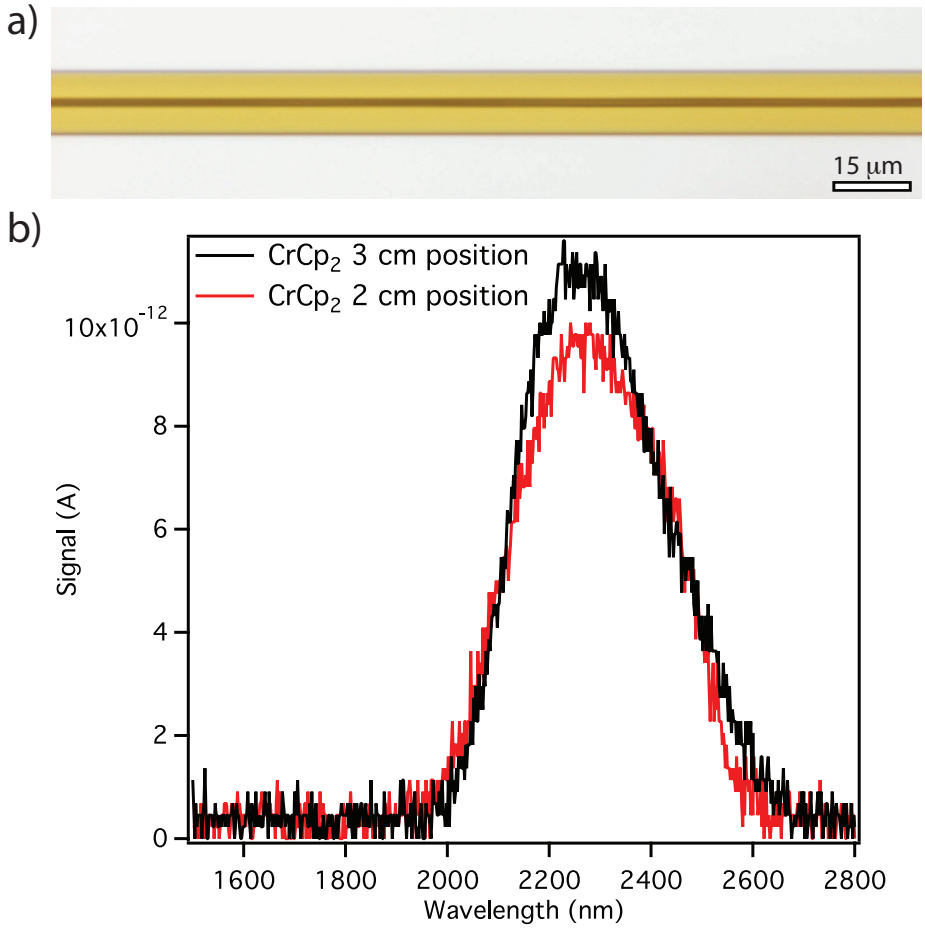

Figure 6.5: Cr^{2+}:ZnSe fluorescence signal from material deposited with $Cr(Cp)_2$ as the chromium source. The deposition quality is similar to that shown for intrinsic ZnSe (a), while the signal, and thus the doping level, is uniform over centimeter length scales (b).

The simplest way to make the $Cr(Cp)_2$ molecule more reactive is to substitute the hydrogens on the cyclopentadienyl ring to make the resulting ring byproduct more stable.[21] This ring stability results in a less stable Cr-Cp bond, which leads to a lower decomposition temperature. Not only does the substitution change the stability, it also changes the vapor pressure at a given temperature as well. The molecules that were investigated were bis(pentamethylcyclopentadienyl)chromium [$Cr(Me_5Cp)_2$], bis(ethylcyclopentadienyl)chromium

[$Cr(EtCp)_2$], and bis(isopropylcyclopentadienyl)chromium [$Cr(iPrCp)_2$]. In order of stability the molecules can be ordered from the most stable to least stable as:[21]

$$Cr(Cp)_2 > Cr(Me_5Cp)_2 > Cr(EtCp)_2 > Cr(iPrCp)_2$$

In terms of vapor pressure at a given temperature, they can be ordered from lowest to highest as:

$$Cr(Me_5Cp)_2 < Cr(Cp)_2 < Cr(iPrCp)_2 < Cr(EtCp)_2.$$

The effects of both vapor pressure and stability on the end concentration of Cr^{2+} in the material are thus coupled.

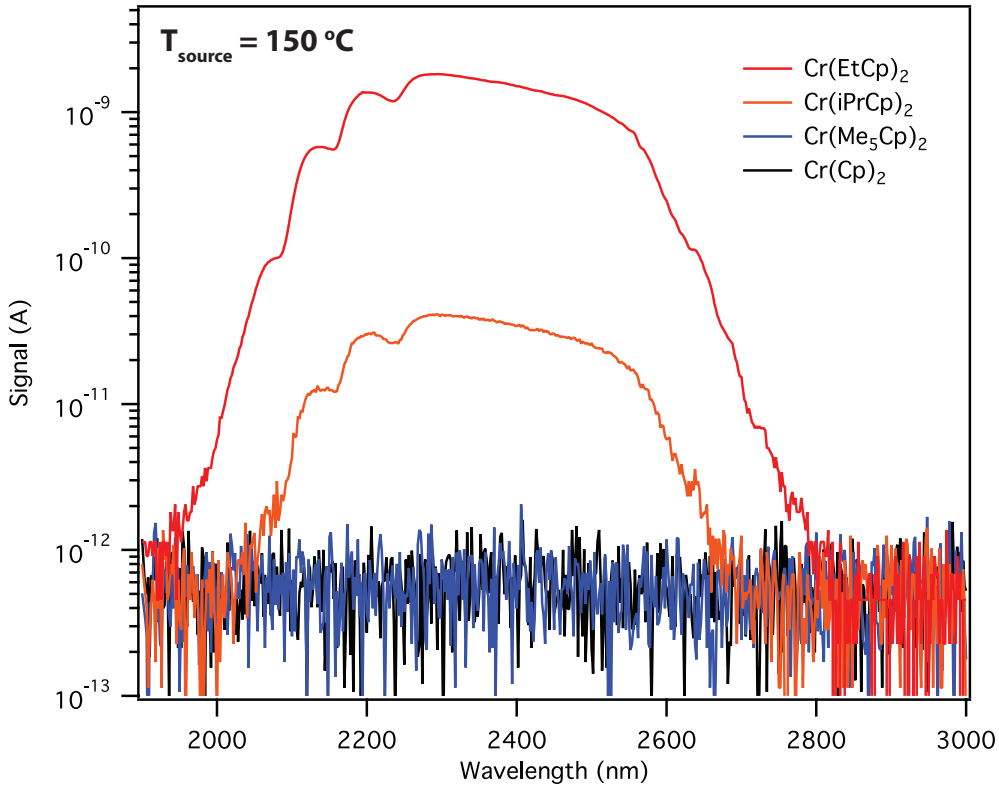

Figure 6.6: Cr^{2+}:ZnSe signal as a function of ring substitution on chromocene at fixed source temperature. (150 °C) The precursor with the highest vapor pressure gives the highest fluorescence signal. The two solid sources do not produce enough vapor for a measurable doping level at this source temperature.

The fluorescence spectra of the resulting Cr^{2+}:ZnSe material deposited with these precursors as chromium sources were used to qualitatively investigate these effects. In **Figure**

6.6, the effects on chromium concentration as a function of source molecule at a fixed source temperature of 150 °C are shown. The two solid sources with low vapor pressures do not result in a measurable fluorescence, but the two liquid sources do, with the $Cr(EtCp)_2$ resulting in the highest chromium concentration, as expected since it also has the highest vapor pressure of the four molecules. It is much more difficult to de-couple the stability of the molecule from this vapor pressure difference without knowing the vapor pressure equations of the molecules. These equations were not found in literature, so an experiment at constant vapor pressure of the chromium source could not be carried out. Measuring the vapor pressure as a function of temperature is an experiment that should be carried out in the future to de-couple these effects to understand the reaction chemistry more thoroughly. **Figure 6.7** shows the coupled nature of the process, with the liquid sources at 150 °C and the solid $Cr(Cp)_2$ source at 225 °C. It can be seen that the doping level of $Cr(EtCp)_2$ and $Cr(Cp)_2$ is comparable at different source temperatures and is uniform over centimeter length scales, which is important for laser applications. The low stability of the $Cr(iPrCp)_2$ precursor is also highlighted in this plot; a very significant difference in the emission intensity is observed over a 1 cm length. The "front" of the fiber (the side closest to the HPCVD sources – dashed lines) is significantly more doped than the downstream region, which indicates that the $Cr(iPrCp)_2$ precursor is not stable enough for the ZnSe chemistry and decomposes at too low of a temperature, similar to that which was observed with $Cr(CO)_6$. However, it is possible that the $Cr(iPrCp)_2$ precursor is resulting in very high doping levels, which would result in concentration quenching and a reduced photoluminescence intensity. In order to determine this, the lifetime of the fluorescence should be characterized (see **Section 6.3.2**); a shorter lifetime than 5 μs will indicate concentration quenching.[22,23] With all of these effects taken into account, the $Cr(EtCp)_2$ precursor was chosen to the best for HPCVD as it allowed for uniform doping (good thermal match with ZnSe reaction chemistry) as well as high vapor

pressure at 150 °C compared to $Cr(Cp)_2$, which requires 225 °C (where splice geometry begins to become very important due to Joule-Thomson effects).

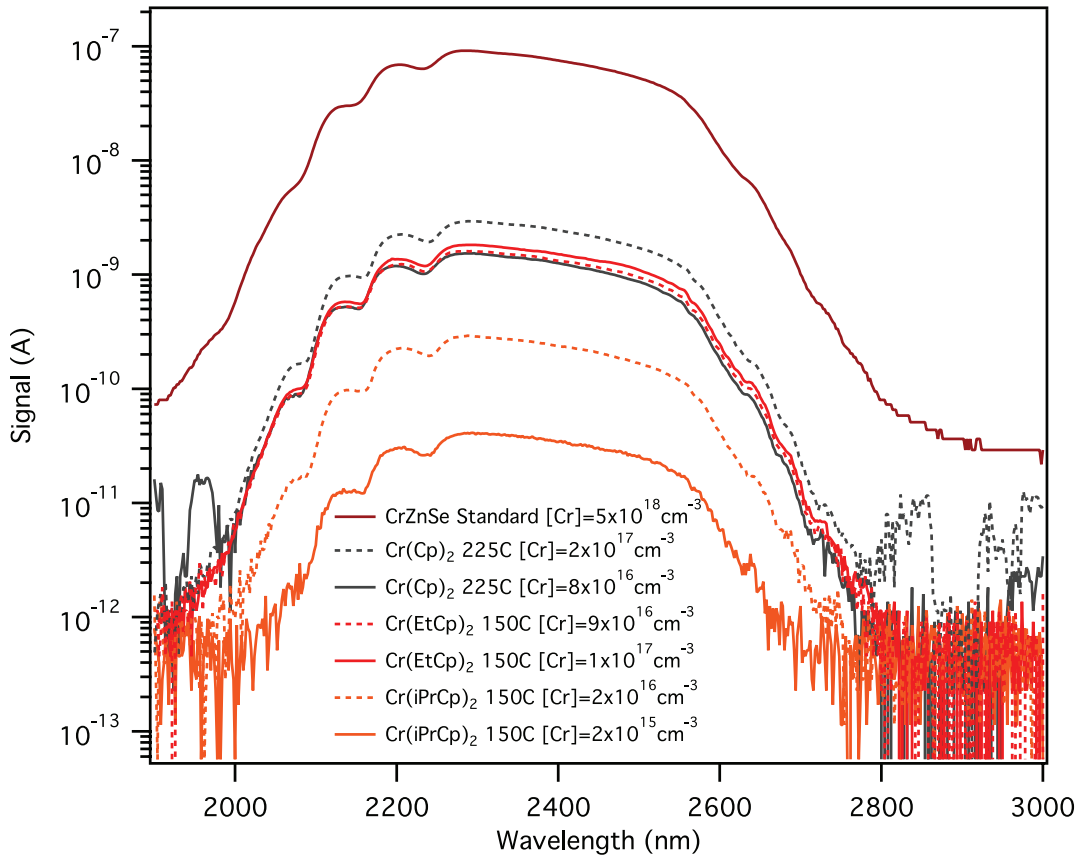

Figure 6.7: Cr^{2+}:ZnSe signal as a function of ring substitution on chromocene. The length difference from the dashed and solid lines of a given sample is ~1 cm. The concentrations of chromium are calculated by comparing to the standard of known concentration.

6.2.2.4 Future Strategies for Iron / Manganese Doping

Fe^{2+}:ZnSe gain media can function from wavelengths of 3.7 – 5.1 μm, a considerably longer wavelength that is valuable for many applications.[6] To date, Fe^{2+}:ZnSe lasers have required an impractically low temperature of operation. It may be, however, that due to the greater efficiency possible with the fiber configuration, operation at higher temperatures is possible. Iron can be doped into ZnSe via diffusion processes as well (from FeSe), but will likely

have the aforementioned issues that were observed with Cr^{2+}:ZnSe. However, the principles that were discovered for in-situ chemical deposition of Cr^{2+}:ZnSe will be applicable to Fe doping.

A key difference in the chemistry is that bis(cyclopentadienyl)iron, ferrocene [$Fe(Cp)_2$], obeys the 18 electron rule, which makes it much more stable than $Cr(Cp)_2$ which only has 16 electrons in the d orbitals. This can be seen in the orders of magnitude difference in the rate constants of pyrolysis at 500 °C for $Fe(Cp)_2$ (k = 0.01 s^{-1}) versus $Cr(Cp)_2$ (k = 1.34 s^{-1}).[21] Therefore a much less stable Fe source is needed for the deposition of Fe^{2+}:ZnSe in HPCVD conditions. Bis(t-butylcyclopentadienyl)iron [Fe(t-butylCp)$_2$] may be a good molecule to start with in the ferrocene family of precursors as it should be much less stable than $Fe(Cp)_2$ as was observed for $Cr(iPrCp)_2$. Moving towards heteroleptic compounds such as cyclopentadienyl-iron-dicarbonyl, pentamethylcyclopentadienyl-dicarbonyl-dimer, and cyclooctatetraene-iron-tricarbonyl could allow the reactivity of the molecule to be tailored with more control. As was seen with $Cr(CO)_6$, $Fe(CO)_5$ is not stable enough and will decompose at too low of a temperature for the ZnSe reaction. As discussed earlier, an alternative approach is to lower the reaction temperature of the ZnSe deposition by using (t-butyl)$_2$Se as a Se source. In this way, the carbonyl compounds may be appropriate.

As the optical power of a fiber laser is scaled, the need for an optical isolator becomes very essential. It would be ideal to fabricate a high power optical fiber isolator out of $Zn_{(1-x)}Mn_xSe$, as it is much more efficient than silica (**Section 1.2.4**) and also transparent in the mid-IR. It has been shown that tricarbonylmethylcyclopentadienyl manganese [$(CO)_3$MeCpMn], which is a liquid at room temperature, is a suitable precursor for Mn doping of II-VI semiconductors.[24] By using the splice designs presented in **Section 6.2.2.2**, introduction of precursors at the high levels needed for alloy formation (x = 0.01 – 0.15) should be straightforward, but will be limited by the Mn solubility in ZnSe.[25] An example of $Zn_{(1-x)}Mn_xSe$ deposition is as follows. The vapor pressure of $(CO)_3$MeCpMn is 1.3 kPa at 100 °C, which gives

a ratio of Zn to Mn in the precursor stream of approximately 8.5:1. This will deposit approximately $Zn_{0.9}Mn_{0.1}Se$. Higher values of *x* can be achieved by increasing the temperature of the $(CO)_3MeCpMn$, or by changing the stability of the molecule by substitution on the cyclopentadienyl ring. Also, it will be important to determine the Verdet constants of this material in the mid-IR, as they have not been reported.

6.3 Cr^{2+}:ZnSe Optical Fiber Lasers

As described earlier, the HPCVD ZnSe filled capillaries function well as low loss, step index optical fibers. With the chromium doping chemistry developed, the basic structure could be investigated for optical fiber laser demonstrations.

6.3.1 Initial CW Pumping Attempts

The first attempts at demonstrating a Cr^{2+}:ZnSe optical fiber laser were in the CW regime with a thulium doped silica fiber laser (10 W, 1908 nm, IPG Photonics) as a pump source. The sample was pumped in the end-fire geometry, with a high reflector (HR) gold mirror evaporated on one facet and an input/output coupling optic (OC) on the other polished facet. Fresnel reflection at the air/Cr^{2+}:ZnSe surface provides a 70% output coupling optic, whereas a 10% coated sapphire substrate can be butt-coupled to the facet to provide a lower output coupling cavity. The sample was fabricated using $Cr(EtCp)_2$ as the chromium source to result in a 2 cm long, 15 μm diameter core step index Cr^{2+}:ZnSe optical fiber.

A thermoelectric cooled waveguide mount stage was used to ensure that the sample was kept cool during high power pumping to alleviate any thermal effects. When the cavity is above threshold, narrowing of the fluorescence spectrum should occur as a specific range of

wavelengths begin to oscillate via stimulated emission. In a free running, waveguide laser, this wavelength will be determined by the gain spectrum of the material as well as the loss of the structure. Since the waveguide loss scales as λ^{-4}, it is expected that the lasing peak should evolve around 2600 nm, as was seen by the first planar Cr^{2+}:ZnSe waveguide laser.[9] However, as can be seen in **Figure 6.8a**, the output fluorescence spectrum from the sample does not change with pumping power with a 70% OC. In fact, the emission intensity decreases with increasing input power, which indicates that the system is undergoing a photo-quenching process. Intra-gap charge transfer processes could be occurring at such high optical power densities, which would reduce the mid-IR signal. Indeed, visible light emission is sometimes observed at such powers; this emission can be attributed to the following mechanisms. Emission at 1.4 eV results from an electronic transition from the Cr^{2+} states to the valence band (or $Cr^{1+} \rightarrow Cr^{2+}$), while emission at 2.2 eV arises from an electronic transition from the conduction band to the Cr^{2+} states (or $Cr^{2+} \rightarrow Cr^{1+}$).[17,26,27] It is likely that as the Cr^{2+} levels become saturated at high pumping power, these processes could be occurring via nonlinear multiphoton absorption.

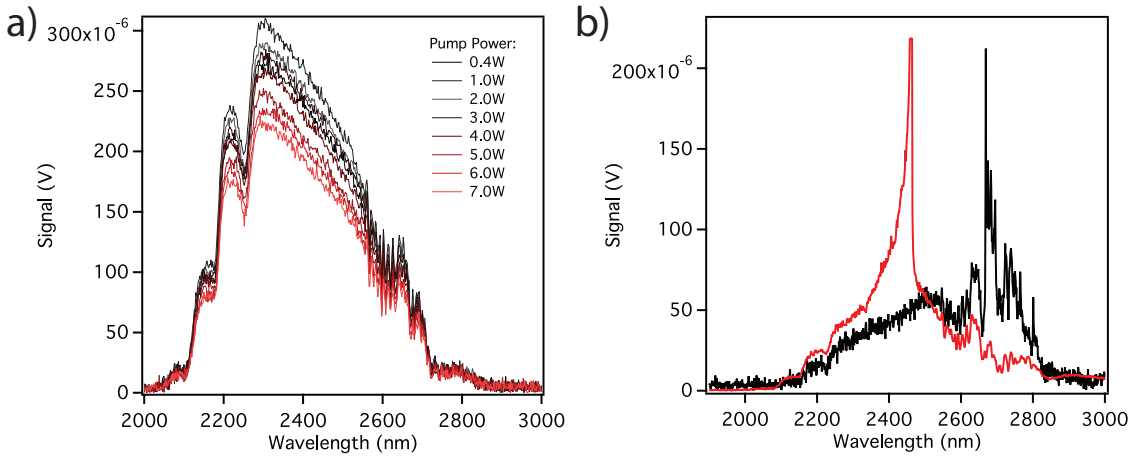

Figure 6.8: Continuous wave pumping of a 15 μm Cr^{2+}:ZnSe optical fiber. (a) Output spectra as a function of input power of a cooled sample with a gold HR and Fresnel reflection OC. (b) Preliminary evidence of lasing in the CW regime, where the spectrum sharpens, but this output is not stable enough to characterize.

Very short instances that appear to be lasing from the sample have been observed (**Figure 6.8b**) at 10W of pumping power, but the sample typically burns before the lasing can be characterized thoroughly. The round trip losses in the cavity are likely too high to achieve stable CW lasing with the given gain that tends to saturate from the relatively low concentration of chromium ions (**Figure 6.8a**). Increasing the gain of the cavity with a higher concentration of chromium ions could allow for stable CW lasing. To lower the round trip losses in the cavity, a lower throughput OC (1 – 5%) could be deposited onto the fiber facet instead of the butt-coupled OC that introduces some loss between the optic and the fiber facet. Also, a $ZnS_xSe_{(1-x)}$ cladding layer is needed, which would lower the losses at the 2600 nm wavelength (from the silica cladding) that is most favorable for lasing in the waveguide geometry. Thus, further improvements in the chemistry, such as layered structures, deposited OC optics on fiber facets, completely filling the hole to reduce the loss of the optical fiber, and higher doping levels for high gain coefficients will make stable CW lasing more achievable.

6.3.2 Proof of Concept Gain Switched Laser

Stable CW lasing proved to be a challenge and could not be thoroughly characterized with the current generation of samples, so the pulsed regime was investigated since the optical intensity and thus gain of the cavity can be increased without damaging the sample by using short pulses of light. In this case, a 10 Hz repetition rate, 10 ns pulse width optical parametric oscillator operating at 1700 nm (providing a higher gain cross-section than 1908 nm pumping) was used to pump the optical fiber in the side-pumped geometry (**Figure 6.9a** inset) The pump beam was focused onto the core of a 5 mm long sample (same sample as **Section 6.3.1**) using a cylindrical lens. The cavity was formed with an evaporated gold mirror HR on one end and Fresnel reflection as an OC from the other facet. The signal was collected with a ZnSe aspheric lens (NA=0.85) and

focused onto the Hamamatsu G5853-203 InGaAs detector with a CaF_2 lens and processed with a gated integrator/boxcar averager (SRS SR250) and pre-amplifier (SRS SR445A).

Clear evidence of a lasing threshold is seen in an output power (at 2 – 3 μm) versus input power plot (**Figure 6.9a**). In the time domain, a sharp increase in output intensity along with a decrease in the lifetime of the Cr^{2+} fluorescence from 5 μs to <500 ns indicates that the cavity is above threshold and lasing (**Figure 6.9b**). Below threshold, the fluorescence kinetics follow a single exponential decay, while above threshold a multi-exponential decay is observed, which is a result of the generation of the laser pulse.[9] In order to determine the lasing wavelength, a spectrum of the output fluorescence below and above threshold to show a sharpening of the output around the predicted wavelength of 2600 nm is needed. Due to the low repetition rate (10 Hz) of the pump laser, a larger core sample will have to be used for the frequency domain analysis to produce more signal that can be aligned through a spectrometer and dispersed with a diffraction grating. Nonetheless, this is the first demonstration of a Cr^{2+}:ZnSe optical fiber laser. Thus, all of the necessary principles for developing high power Cr^{2+}:ZnSe optical fiber lasers have been developed in this dissertation. In **Chapter 7**, the scaling and development of these principles for fabricating high power optical fiber lasers is discussed.

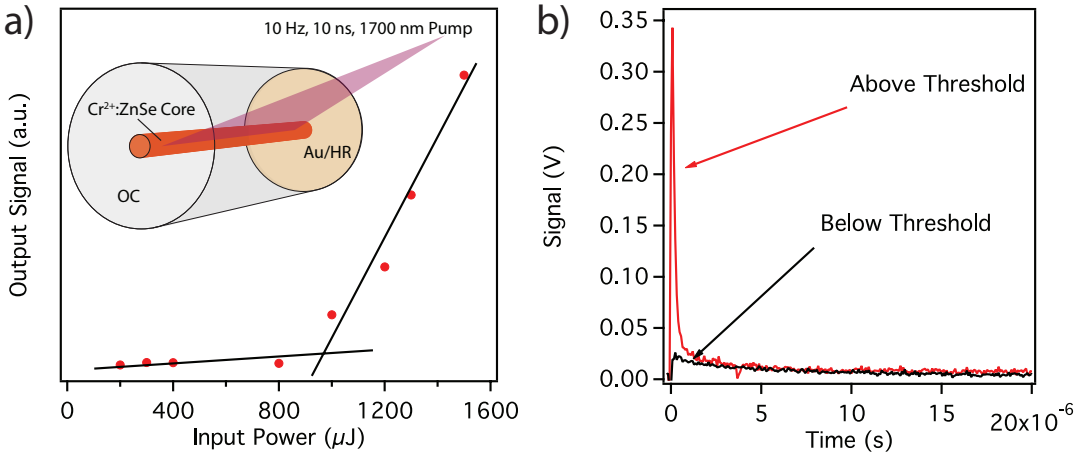

Figure 6.9: Gain switched lasing of a 15 μm Cr^{2+}:ZnSe optical fiber. Clear evidence of threshold behavior is observed (a) along with a sharpening of the fluorescence lifetime (b).

6.4 References

[1] L. D. DeLoach, R. H. Page, G. D. Wilke, S. A. Payne, and W. F. Krupke, "Transition Metal-Doped Zinc Chalcogenides: Spectroscopy and Laser Demonstration of a New Class of Gain Media" *IEEE J. Quantum. Electron.* **1996**, 32, 885.

[2] H. Jelinkova, P. Koranda, M. E. Doroshenko, T. T. Basiev, J. Sulc, M. Nemec, P. Cerny, V. K. Komar, and M. B. Kosmyna, "Cr^{2+}:ZnSe Laser Pumped by 1.66 μm or 1.97 μm Radiations" *Laser Phys. Lett.* **2007**, 4, 23.

[3] I. S. Moskalev, V. V. Fedorov, and S. B. Mirov, "Tunable, Single-Frequency, and Multi-Watt Continuous-Wave Cr^{2+}: ZnSe Lasers" *Opt. Express* **2008**, 16, 4145.

[4] I. T. Sorokina, "Cr^{2+}-Doped II-VI Materials for Lasers and Nonlinear Optics" *Opt. Mater.* **2004**, 26, 395.

[5] S. Kuck, "Cr^{2+} Lasers" *SPIE Adv. Lasers Sys.* **2003**, 5137, 48.

[6] S. Mirov, V. Fedorov, I. Moskalev, D. Martyshkin, and C. Kim, "Progress in Cr^{2+} and Fe^{2+} Doped Mid-IR Laser Materials" *Laser Photon. Rev.* **2010**, 4, 21.

[7] I. Moskalev, V. Fedorov, and S. Mirov, "10-Watt, Pure Continuous-Wave, Polycrystalline Cr^{2+}:ZnS Laser" *Opt. Express* **2009**, 17, 2048.

[8] K. L Schepler, R. D. Peterson, P. A. Berry, and J. B. McKay, "Thermal Effects in Cr^{2+}:ZnSe Thin Disk Lasers" *IEEE J. Sel. Top. Quantum Electron.* **2005**, 11, 713.

[9] J. E. Williams, V. V. Fedorov, D. V. Martyshkin, I. S. Moskalev, R. P. Camata, and S. B. Mirov, "Mid-IR Laser Oscillation in Cr^{2+}:ZnSe Planar Waveguide" *Opt. Express* **2010**, 18, 25999.

[10] J. E. Williams, D. V. Martyshkin, V. V. Fedorov, I. S. Moskalev, R. P. Camata, and S. B. Mirov, "Cr:ZnSe Planar Waveguide Mid-IR Laser" *Proc. SPIE: Solid State Lasers* **2011**, 7912, 79121H.

[11] D. J. Richardson, J. Nilsson, and W. A. Clarkson, "High Power Fiber Lasers: Current Status and Future Perspectives" *J. Opt. Soc. Am. B* **2010**, 27, B63.

[12] J. O. Ndap, K. Chattopadhyay, O. O. Adetunji, D. E. Zelmon, and A. Burger, "Thermal Diffusion of Cr^{2+} in Bulk ZnSe" *J. Cryst. Growth* **2002**, 240, 176.

[13] Y. F. Vaksman, V. V. Pavlov, Y. A. Nitsuk, Y. N. Purtov, A. S. Nasibov, and P. V. Shapkin, "Optical Absorption and Chromium Diffusion in ZnSe Single Crystals" *Semiconductors* **2005**, 39, 377.

[14] V. I. Levchenko, V. N. Yakimovich, L. I. Postnova, V. I. Konstantinov, V. P. Mikhailov, and N. V. Kuleshov, "Preparation and Properties of Bulk ZnSe:Cr Single Crystals" *J. Cryst. Growth* **1999**, 198, 980.

[15] V. A. Akimov, M. P. Frolov, Y. V. Korostelin, V. I. Kozlovsky, A. I. Landman, Y. P. Podmar'kov, and A. A. Voronov, "Vapour Growth of II-VI Single Crystals Doped by Transition Metals for Mid-Infrared Lasers" *Phy. Stat. Sol. C* **2006**, 3, 1213.

[16] A. Burger, K. Chattopadhyay, J. O. Ndap, X. Ma, S. H. Morgan, C. I. Rablau, C. H. Su, S. Feth, R. H. Page, K. I. Schaffers, and S. A. Payne, "Preparation Conditions of Chromium Doped ZnSe and their Infrared Luminescence Properties" *J. Cryst. Growth* **2001**, 225, 249.

[17] A. Gallian, V. V. Fedorov, J. Kernal, J. Allman, S. B. Mirov, E. M. Dianov, A. O. Zabezhaylov, and I. P. Kazakov, "Spectroscopic Studies of Molecular-Beam Epitaxially Grown Cr^{2+}-Doped ZnSe Thin Films" *Appl. Phys. Lett.* **2005**, 86, 091105.

[18] M. Jouanne, J. F. Morhange, E. Dynowska, E. Lusakowska, W. Szuszkiewicz, L. W. Molenkamp, and G. Karczewski, "Structure Characterization of MBE-Grown (Zn,Cr)Se Layers" *J. Alloy. Compd.* **2004**, 382, 92.

[19] F. Maury, C. Vahlas, S. Abisset, and L. Gueroudji, "Low Temperature Metallorganic Chemical Vapor Deposition Routes to Chromium Metal Thin Films Using Bis(benzene)chromium" *J. Electrochem. Soc.* **1999**, 146, 3716.

[20] J. R. Thygeson and M. C. Molstad, "High Pressure Hydrogen Attack of Steel" *J. Chem. Eng. Data* **1964**, 9, 309.

[21] L. M. Dyagileva, E. I. Tsyganova, and Y. A. Aleksandrov, "The Kinetic Stability of Biscyclopentadienyl and Diarene Compounds of Transition Metals in the Thermal Decomposition Reaction" *Russian Chem. Rev.* **1988**, 57, 316.

[22] A. Sennaroglu, U. Demirbas, A. Kurt, and M. Somer, "Direct Experimental Determination of the Optimum Chromium Concentration in Continuous-Wave Cr^{2+}: ZnSe Lasers" *IEEE J. Sel. Top. Quantum Electron.* **2007**, 13, 823.

[23] A. Sennaroglu, U. Demirbas, A. Kurt, and M. Somer, "Concentration Dependence of Fluorescence and Lasing Efficiency in Cr^{2+}:ZnSe Lasers" *Opt. Mater.* **2007**, 29, 703.

[24] P. J. Wright, B. Cockayne, A. F. Cattell, P. J. Dean, A. D. Pitt, and G. W. Blackmore, "Manganese Doping of ZnS and ZnSe Epitaxial Layers Grown by Organometallic Chemical Vapour Deposition" *J. Cryst. Growth* **1982**, 59, 155.

[25] D. Litvinov, D. Gerthsen, B. Daniel, C. Klingshirn, and M. Hetterich, "Defects and Phase Distribution in Epitaxial ZnMnSe Layers Analyzed by Transmission Electron Microscopy" *J. Appl. Phys.* **2006**, 100, 023523.

[26] M. Godlewski, M. Surma, V. Y. Ivanov, and T. P. Surkova, "Mechanisms of Radiative and Nonradiative Recombination in ZnSe:Cr and ZnSe:Fe" *Low Temp. Phys.* **2004**, 30, 897.

[27] B. K. Rai, R. S. Katiyar, K. T. Chen, and A. Burger, “Raman and Photoluminescence Studies on Intrinsic and Cr-Doped ZnSe Single Crystals” *J. Appl. Phys.* **1998**, 83, 6011.

Chapter 7

Conclusions

With many of the key principles in place, such as low loss ZnSe optical fibers, chemical deposition of Cr^{2+}:ZnSe, and proof of concept lasing in the pulsed regime, ongoing work will be to optimize the structure and materials properties to demonstrate Cr^{2+}:ZnSe optical fiber lasers in the high power CW regime. A schematic of an ideal structure for power scaling the laser into the multi-watt CW regime is shown in **Figure 7.1**. A D-shaped cladding region of $ZnS_xSe_{(1-x)}$ is used to both control the mode structure of the waveguide with a small refractive index gradient as well as to break the symmetry of the cladding to allow for efficient cladding pumping of the Cr^{2+}:ZnSe core. Also, the layer will alleviate any absorption effects in the IR from silica above 3 μm. The diameter of the waveguiding core is large so that high powers of pump radiation can be focused into the structure, while the length is on the centimeter scale to absorb all the pump light efficiently. Owing to the long interaction length, the doping levels can be kept relatively low to reduce the thermal load over the length of the fiber. The structure is completely filled using the annealing techniques presented in **Chapter 4**, with either a thermal expansion matched glass cladding, or a SiC or Si_xN_y higher thermal conductivity cladding. This dissertation has developed all of the necessary principles for fabricating this structure and the next step in this research will be to put it all together. As the power is scaled, the need for optical isolation will become more important. Materials such as the DMS $Zn_{(1-x)}Mn_xSe$ (**Section 1.2.4**) would be ideal candidates for such devices and could readily be fabricated into the optical fiber geometry using the chemical principles developed in this dissertation. To access wavelengths further into the mid-IR, iron doping could be developed along with nonlinear OPG processes based on the second order nonlinearity of ZnSe (**Chapter 5**) to create a new platform of mid-IR optical fiber laser sources.

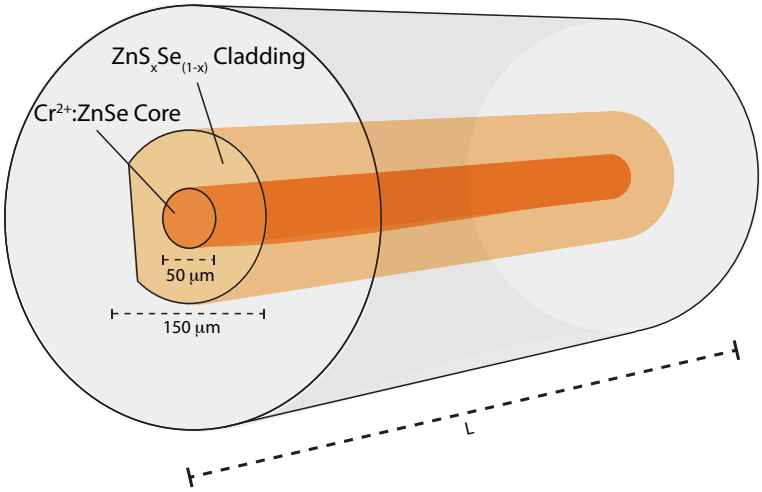

Figure 7.1: A schematic of an ideal structure for power scaling Cr^{2+}:ZnSe optical fiber lasers.

As was shown throughout this dissertation, HPCVD is a useful tool for infiltrating high aspect ratio structures, such as MOFs, with chemical precursors for the deposition of a variety of materials. HPCVD can also be extended to other confined geometries such as microfluidic chips, inverse opals, and biotemplates. Interfacing HPCVD with microfluidic architecture could lead to a variety of new function in both platforms. For example, the field of optofluidics combines optical elements with microfluidic elements; depositing high quality optical materials in the channels of microfluidic chips could be another application of HPCVD. Furthermore, the polydimethylsiloxane channels routinely used in microfluidics are readily swelled in common solvents that limit their use as for microfluidic syntheses; coating the channels with a refractory material with HPCVD could alleviate this issue, while ZnO could be deposited and used as a piezoelectric microvalve. The control of laminar flow offered by microfluidic chips could be used to generate pulses of precursors that can flow into MOFs for high pressure ALD applications. The conformal nature of HPCVD could also be advantageous for biotemplating applications as well coating planar, nanostructured opals and photonic crystals. Importantly, the HPCVD principles discussed in this dissertation are not restricted to optical fiber applications.

VITA

Justin R. Sparks

EDUCATION

Ph.D., Chemistry 2007-2013
The Pennsylvania State University, University Park, Pennsylvania

B. S., Chemistry, Summa Cum Laude 2003-2007
DeSales University, Center Valley, Pennsylvania

AWARDS

Braucher Fellowship Award, Pennsylvania State University 2012
Apple Fellowship Award, Pennsylvania State University 2011
Worldwide University Network Grant, University of Southampton 2009
Incoming Graduate Student Award, Pennsylvania State University 2008
Dan H. Waugh Memorial Teaching Award, Pennsylvania State University 2008
Roberts Graduate Fellowship, Pennsylvania State University 2008
The Chemistry Award for Academic Excellence, DeSales University 2007
The Chemistry Award for Excellence in Research, DeSales University 2007
Lehigh Valley Section of the American Chemical Society Undergraduate Award 2007
CRC Press Freshman Excellence in Chemistry Award 2004

SELECTED PUBLICATIONS

J. R. Sparks, R. He, N. Healy, S. Chaudhuri, T. C. Fitzgibbons, A. C. Peacock, P. J. A. Sazio, and J. V. Badding, "Conformal Coating by High Pressure Chemical Deposition for Patterned Microwires of II-VI Semiconductors" *Advanced Functional Materials* **2012**, DOI: 10.1002/adfm.201202224.

R. He, P. J. A. Sazio, A. C. Peacock, N. Healy, **J. R. Sparks**, V. Gopalan, and J. V. Badding, "Integration of GHz Bandwidth Semiconductor Devices inside Microstructured Optical Fibres" *Nature Photonics* **2012**, 6, 174-179.

J. R. Sparks, J. L. Esbenshade, R. He, N. Healy, T. D. Day, D. W. Keefer, P. J. A. Sazio, A. C. Peacock, and J. V. Badding, "Selective Semiconductor Filling of Microstructured Optical Fibers" *Journal of Lightwave Technology* **2011**, 29, 2005-2008.

J. R. Sparks, R. He, N. Healy, M. Krishnamurthi, A. C. Peacock, P. J. A. Sazio, V. Gopalan, and J. V. Badding, "Zinc Selenide Optical Fibers" *Advanced Materials* **2011**, 23, 1647-1651.

N. Healy, **J. R. Sparks**, R. He, P. J. A. Sazio, J. V. Badding, and A. C. Peacock, "High Index Contrast Semiconductor ARROW and Hybrid ARROW Fibers" *Optics Express* **2011**, 19, 10979-10985.

N. F. Baril, B. Keshavarzi, **J. R. Sparks**, M. Krishnamurthi, I. Temnykh, P. J. A. Sazio, A. C. Peacock, A. Borhan, V. Gopalan, and J. V. Badding, "High-Pressure Chemical Deposition for Void-Free Filling of Extreme Aspect Ratio Templates" *Advanced Materials* **2010**, 22, 4605-4611.

N. Healy, **J. R. Sparks**, M. N. Petrovich, P. J. A. Sazio, J. V. Badding, and A. C. Peacock, "Large Mode Area Silicon Microstructured Fiber with Robust Dual Mode Guidance" *Optics Express* **2009**, 17, 18076-18082.